UNIVERSITÀ
DEGLI STUDI
FIRENZE

Università degli Studi di Firenze
Dipartimento di Ingegneria dell'Informazione (DINFO)
Corso di Dottorato in Ingegneria dell'Informazione
Curriculum: Automatica, Ottimizzazione e Sistemi Complessi

Structure and Collective Behaviour: A Focus on the Inverse Problem

Candidate
Ihusan Adam

Supervisors
Prof. Duccio Fanelli

Prof. Giacomo Innocenti

PhD Coordinator
Prof. Fabio Schoen

ciclo XXXIII, 2017-2020

Università degli Studi di Firenze, Dipartimento di Ingegneria
dell'Informazione (DINFO).

Thesis submitted in partial fulfillment of the requirements for the degree of Doctor of Philosophy in Information Engineering. Copyright © 2021 by Ihusan Adam.

This thesis is dedicated to my loving wife, mom and dad.

Abstract

The aim of this thesis is to inform our understanding of the exquisite relationship between function and structure of complex systems with a particular focus on the inverse problem of inferring structure from collective expression. There exists a rich body of work explaining complex collective behaviour through its interdependence on structure and this forms the core subject matter of the field complex networks. However, in many cases of interest, the underlying structure of the observed system is often unknown and can only be studied through limited measurements. The first chapters of this thesis develop and refine a method of inferring the structure of *a priori* unknown networks by leveraging the celebrated Heterogeneous mean-field approximations. The inverse protocol is first formulated for and rigorously challenged against synthetic simulations of reactive-random-walkers to successfully recover the degree distributions from partial observations of the system. The reconstruction framework developed is powerful enough to be applicable to many real-world systems of great interest. This is demonstrated by the extension of the method to a nonlinear Leaky-Integrate and Fire (LIF) excitatory neuronal model evolving on a directed network support to recover both the in-degree distribution and the distribution of associated current in Chapter 5. In this chapter, this method is also applied to wide-field calcium imaging data from the brains of mice undergoing stroke and rehabilitation, which is presented as a spatiotemporal analysis in Chapter 4. The findings of Chapters 4 and 5 complement each other to showcase two potential non-invasive ways of tracking the post-stroke recovery of these animals. One analysis focuses on the subtle changes in propagation patterns quantified through three novel biomarkers, while the other shifts the attention to the changes in structure and inherent dynamics as seen through the inverse protocol. This reconstruction recipe has also been extended to a more general two species LIF model accounting for both inhibitory and excitatory neurons

in Chapter 6. This was applied to two-photon light-sheet microscopy data from zebrafish brains upon successful validation *in silico*. Lastly, Chapter 7 studies a particular phenomenon of interest where structure and inherent dynamics affect the function in a different but popular class of networks. A zero-mean noise-like prestrain is used to induce contractions in 1D Elastic Network Models. The analysis shows that the exact solution is difficult to probe analytically, while the mean behaviour of the networks are predictable and controllable by tuning the magnitude of the applied prestrain.

Contents

Introduction

Many phenomena found in nature is often studied through a systems of point of view, by dissecting the whole into its parts. Complex Systems are systems, where this whole consists of many, often simple interacting elements. Interlinked, these elements display vastly complex and remarkable collective behaviours that cannot be explained let alone predicted without describing the complete system. This broad definition allows one to cast a great many problems into the realm of complex systems and rightfully so. A vast amount of natural phenomena of great fascination and scientific interest arise macroscopically as a direct consequence of the microscopic interactions of the interlinked elements [1]. Approached through a multi-disciplinary lens, this observation provides the ideal framework for investigation that cuts through a multitude of diverse fields. The flocking of birds, swarming of insects and schooling of fish highlight the ability of ecological system to display complex coordinated behaviour and self organization [2; 3; 4; 5; 6; 7]. The symmetry of spin glasses [8] or the phase transitions of matter testify to the non-triviality of the influence of micro-states on emergent macroscopic properties in physical systems [9]. The limited predictability of the stock markets or the cascading effects of opinion dynamics showcase the complexity in financial and social systems [10; 11]. Brain functions, genomics, population dynamics and the folding of proteins are just some of the examples found in biology and life sciences [12; 13; 14; 15; 16].

Complex systems often have the characteristic of displaying behaviour that is a non-trivial aggregate of its parts. In many cases of interest, the facet of these systems that brings about this complexity is the nature, or rather the structure of how individual entities are coupled together. Networks are abstract mathematical structures, often invoked in modelling the dynamics of the complex interacting units [17; 18; 19; 20; 21]. The brain, internet and the cyberworld, foodwebs and social contacts are examples drawn from dis-

tinct fields of investigation, which can be ideally grouped under the unifying umbrella of network science. Nodes (vertices) can point to individual actors of the inspected dynamics (e.g. material units, bits of information or on a different scale, extended populations), while edges (links) stand for existing bilateral ties. Alternatively, nodes can tag spatial or functional niches, bounded regions of an embedding landscape, that are mutually connected by physical or virtual paths, as epitomized by the links [20; 22; 23; 24; 25; 26]. Irrespective of the specifics of the realm of investigation, the nature of the pairwise coupling amongst nodes class the links between them into two general types which are either directed or undirected depending on whether interactions are mutual or one-sided, respectively [18]. Due to the potency of these ingredients in modelling an ever-increasing plethora of natural phenomena, complex networks are finding successful application in describing problems not only in the natural sciences [27], but also in fields as diverse the climatology [28; 29] through to epidemiology [30; 31], computer sciences [32] and sociology [33]. Networks also find their way into emerging fields such as smart cities and artificial intelligence and learning algorithms [34; 35; 36].

The power of networks in describing the behaviour of real-world phenomena is attributable to being able to encode, mathematically, the intricacy of the discrete structural support for the dynamical processes that mimic their real-world counterparts [20; 27]. In this representation, the state of the system is captured by the instantaneous states of each node, which is defined as a multidimensional variable whose evolution in time is generally governed by a set of ordinary differential equations.

This allows one to use many physical concepts to describe the interaction between nodes in these abstract spaces like random walks, diffusion, percolation or other linear processes [37; 38; 39]. The modelling power and numerosity of observed behaviour possible with such networks get greatly enhanced when we endow the individual sites with its own dynamics to act on the flowing entities or species that make up the network. The nodes can have its own inherent reaction dynamics, describable by its own specific differential equations. This added ingredient creates a myriad of remarkable complex global behaviour that is otherwise impossible from purely node-to-node interactions. Patterns, both static or oscillating limit cycles that are so prominent in nature arise, as described in this seminal paper [40] or is demonstrated chemically in experiments such as the Belousov-Zhabotinsky [41] reactions, as a direct consequence of reactive and diffusive aspects of

such systems [42; 43; 44; 45; 46; 47; 48; 49].

For a lot of these real-world systems, what we invariably find is that the structure of the system plays a role of utmost importance in determining how the collective behaves. A vast body of work exists to characterize, class and describe a multiplicity of abstract networks. Ranging from networks with a few hubs linking the entire network, as is the case with internet and social networks [50; 51], to those that are completely random, to ones that are regular and lattice-like. There are those that are somewhat in between like in the case of small-world networks [21; 52; 53]. The classifications can go much deeper based on various descriptions of features that can be used to distinguish one particular class from the next. These could range from sub-features of the network, like sub-graphs or motifs [54], or the existence of relatively closed communities [55] and clustering to those that are characterized by the distance between any two nodes as in the case of small-world networks [56]. Other distinctions are based on the processes behind the formation of networks in nature or their synthetic generation as in the case of Erdös-Rényi or Preferential attachment or Watt-Strogatz networks [19; 56; 57].

These recognized classes of networks have been studied and applied successfully to a rich body of problems, whereby the knowledge of the structure allows one to describe, predict and in some cases control [58; 59] the behaviour of real-world systems. However, an area that is still not well understood is the inverse problem. This is the problem of inferring the structure of the network connections from the display of the collective expression of the system as a whole.

In many cases of interest, one often has knowledge of the rules governing the dynamics of the fundamental building blocks of incredibly complex systems and has access to how a portion or the whole network behaves when these fundamental units are coupled via an *a priori* unknown web of intricate links. One such example is the brain where simple base blocks, neurons, that operated in a non-intelligent and almost mechanistic fashion is able to create, when coupled to many billions of other such units, a collective phenomenon that is so unfathomably complex that it contain the entire field of conscious experience. The make-up, function and dynamics of single neurons and groups of neurons are rather well understood and can be modelled mathematically [60; 61; 62]. An integral part of the of modelling the dynamics of complex systems such as neuronal models is the architecture of the connections linking the units and invariably this leaves its imprint on the collective

output of the system. However, a unified theory of the penetrating interdependence of the structure of networks and the resulting dynamics is still lacking and considered to be a significant challenge in network science. Our aim is to contribute towards this broad goal by focusing on the intertwined relationship of dynamics and structure as an inverse problem of inferring information about the structure through its imprint on the collective phenomena. Inferring insights into the embedding network from observations of the global phenomena is a challenging task as we shall see later on in the thesis as we gradually build and tackle this problem first in synthetic scenarios and eventually move into real-world contexts.

In the immediate next chapter, we will introduce the theoretical background needed for the later chapters. In Chapter 2, a procedure is developed and tested to recover the distribution of connectivity of an *a priori* unknown network, by sampling the dynamics of an ensemble made of reactive walkers, a combination of self reaction and random walks. The relative weight between reaction and relocation is gauged by a scalar control parameter, which can be adjusted at will. Different equilibria are attained by the system, following the externally imposed modulation, and reflecting the interplay between reaction and diffusion terms. The information gathered on the observation node is used to predict the stationary density as displayed by the system, via a direct implementation of the celebrated Heterogeneous Mean Field (HMF) approximation. This knowledge translates into a linear problem which can be solved to return the entries of the sought distribution. A variant of the model is then considered which introduces a local class of nodes called sources where the reactive constituents are injected at a rate that can be adjusted as a stepwise function of time. The linear problem obtained when operating in this setting allows one to recover a fair estimate of the underlying system size. Numerical experiments are carried so as to challenge the predictive ability of the theory.

The next chapter introduces and analyzes a data set of *in vivo* cortical recordings of mice undergoing an induced stroke and eventual recovery that will be used for an inversion procedure in the subsequent chapters. Stroke is a debilitating condition affecting millions of people worldwide. The development of improved rehabilitation therapies rests on finding biomarkers suitable for tracking functional damage and recovery. To achieve this goal, a detailed spatiotemporal analysis of wide-field cortical calcium images from mice during longitudinal motor training is performed, before and after focal

stroke induction and two different rehabilitation paradigms: motor training alone and combined with pharmacological therapy. Three novel indicators are identified that are able to track how movement-evoked global activation patterns are impaired by stroke and evolve during rehabilitation: the duration, angle and smoothness of individual propagation events. When comparing rehabilitation paradigms clear signs of recovery for both are found, but surprisingly, cortical propagation in double treated mice is even faster and smoother than before stroke. The propagation-based biomarkers deliver novel insights into brain mechanisms underlying motor recovery that pave the way towards a more targeted post-stroke therapy.

In Chapter 4 we generalize the reconstruction framework in Chapter 2 and test an inversion framework which aims at recovering the *a priori* unknown functional and structural information from global signals of living brains activity, i.e. the wide-field calcium recording dataset in Chapter 4. The unmatched ability of the brain to cope with an extraordinarily large plethora of complex tasks, carried out in parallel, ultimately resides in the intricate web of interlinked connections which define the architecture of the embedding neurons' network. Structural and functional information, as inferred from direct measurements of neuronal activity, under different experimental conditions, are fundamental pieces of a jigsaw puzzle of how the brains works, from simple organisms to more complicated creatures, across phylogenetic scales. To this end, we consider a Leaky-Integrate and Fire (LIF) model with short term plasticity neurons, coupled via a directed network. Neurons in the model are assigned a specific current value, which is heterogeneous across the sample, and sets the firing regime in which the neuron is operating in. The aim of the method is to recover the distribution of incoming network degrees as well as the distribution of the assigned currents from global field measurements. The proposed approach to the inverse problem implements the reductionist Heterogenous Mean-Field approximation. This amounts in turn, to organizing the neurons in different classes depending on their associated degree and current. When tested against synthetic data, the method returns accurate estimates of the sought distributions, while managing to reproduce and interpolate almost exactly the time series of the supplied global field. Finally, we also applied the proposed technique to longitudinal wide-field fluorescence microscopy data of cortical functionality in groups of awake Thy1-GCaMP6f mice (transgenic mice that allow Ca^{2+} dynamics to be monitored through contain genetically encoded sensors). Mice

are induced a photothrombotic stroke in the primary motor cortex and their recovery monitored in time. An all-to-all LIF model which accommodates for currents heterogeneity allows to adequately explain the recorded patterns of activation. Altered distributions in neuron excitability are in particular detected, which are compatible with the phenomenon of hyperexcitability in the penumbra region after stroke.

In Chapter 5 we build and generalize the method in Chapter 4 for an extended LIF model allowing for two species of neurons, excitatory and inhibitory, while aiming to recover structural and functional information from brain activity. Neurons are endowed with a heterogeneous current value, which sets their associated dynamical regime. By making use of a heterogenous mean-field approximation, the method seeks to reconstruct from global activity patterns the distribution of in-coming degrees, for both excitatory and inhibitory neurons, as well as the distribution of the assigned currents. The proposed inverse scheme is first validated against synthetic data. Then, time-lapse acquisitions of a zebrafish larva recorded with a two-photon light-sheet microscope are used as an input to the reconstruction algorithm. A power law distribution of the in-coming connectivity of the excitatory neurons is found. Local degree distributions are also computed by segmenting the whole brain in sub-regions traced from annotated atlas.

Lastly, in Chapter 6 we study the effects of network structure on Elastic Network Models (ENMs) which are powerful, versatile modelling tools with a wide variety of applications in numerous fields, ranging from material sciences to biophysical systems. Recently, there has been an increased interest in crafting ENMs that can perform a prescribed function. Here, we propose and analyse a framework of inducing contractions as an intrinsic property of the underlying dynamics of 1D elastic networks. This is achieved by relying solely on a random, zero mean, noise-like prestrain imposed on the links of the network. We show the expected behaviour of such systems by numerical simulations, and formulate analytical predictions for the magnitude of the contractions as a function of the strength of the prestrain. Furthermore, we assess the robustness of the method against changes in topology, testing scale-free, Watts-Strogatz and a third type of network topology designed to maximise the length of the links, that we call End-Hubs.

Chapter 1

Complex networks: A short overview

To understand complex systems we must begin by looking at how its parts interact with each other. This means describing the connections between the various components that make up the system [17; 52]. The field of mathematics that deals with the study of systems and its components through mathematical abstraction is known as *graph theory*. The idea of representing sites of interest and the connections between them through abstract mathematical pointers was first introduced by Euler in his proof of the bridges of Könisberg problem [52]. Since its inception, the power of separating the actual problem being studied into a mathematical catalogue representation (known as a *network* or a *graph*) of *nodes* or *vertices* connected by *links* or *edges* has proved to be important in tackling many problems. This fact is made evident by the ever-present scientific interest on the topic even almost 300 years after that first paper.

When modeling real-world systems from fields such as biology, ecology, or sociology, and many others, the nodes can represent the individual entities of the investigated dynamics or embody spatial regions. The links refer to the virtual or real paths making up the node to node interactions that form the system. Networks serve as the common language to interpret many systems that may differ in appearance, nature, or scale essentially creating a versatile toolset to study complex systems.

Links of networks can be *directed* or *undirected* based on whether the pairwise interactions are asymmetric, e.g. World-Wide-Web (WWW) links

through URL, or symmetric, e.g. elastic interactions between beads connected by a springs (a model studied in Chapter 6). The links can also denote the strength of the coupling between nodes in the case of *weighted* networks, e.g. trade volumes between countries. In a network of size N elements, nodes are generally identified by an index $i = 1, \ldots, N$. The network is then captured through an *adjacency matrix*, $\mathbf{A} \in \mathbb{R}^{N \times N}$, where the A_{ij} is equal to the weight of the link connecting node j to i and is 0 if the two nodes are not connected. The adjacency matrix is symmetric for undirected networks and asymmetric for directed networks. Furthermore, if the weight of the links of the network are all equal or are unweighted then the connections and absent links are shown by ones and zeros respectively, i.e., *binary*. One important property of the nodes that can then be immediately computed is *degree* of the i^{th} node denoted as $k_i = \sum_{j=1}^{N} A_{ij}$ for undirected networks and can be represented by a N dimension vector $\mathbf{k}$ which accounts for the total number of links as $L = \frac{1}{2}\sum_{i=1}^{N} k_i$. For a directed network the node degrees are defined for *in-degree*, $K_i^{in} = \sum_{j=1}^{N} A_{ij}$, and *out-degree*, $k_i^{out} = \sum_{i=1}^{N} A_{ij}$ while for a symmetric network these two measures are equal, $k_i = k_i^{in} = k_i^{out}$.

1.1 Commonly encountered topologies

The basic measures of the properties of networks defined above are useful to make sense of networks encountered in the real world. These tools help us quantify and differentiate the numerous networks that can exist both in the real-world and synthetically. As more and more networks are explored through the increasing toolset of network science, there are patterns and similarities between networks that allow us to categorise the commonly encountered types. The various types or *topologies* of networks are categorized in a way that reflects certain defining features of the underlying connections of the network. While there are many metrics and tools for studying various network characteristics [52; 63], this chapter will present an introduction to common typologies focusing on just the metrics relevant for the subsequent chapters. We will have a closer look at *lattices*, *random networks*, *small-world networks* and *scale free* networks as these will be frequently referenced in the chapters that follow.

1.1.1 Lattice networks

Some of the simpler networks we encounter have a regular structure where every node has the same number of connections. These are useful in modelling geometries in Euclidean spaces of arbitrary dimensions $\mathbb{R}^n$ where embedding these networks in such spaces results in a mesh or grid that forms a regular tiling of the spaces. They are sometimes referred to as *spatial networks* for this reason. For instance, this regularity lends itself to the modelling of the regular arrangement of atoms or molecules in crystalline solids and more recent examples can be found in ecology, biology, chemistry and economics and financial markets amongst many others [64; 65; 66; 67].

It is useful to introduce the degree distribution at this stage as a statistic that allows us to easily identify the structural characteristics of a network and can be used to distinguish one type of network from another.

The *degree distribution*, $P(k)$ is the probability of a randomly chosen node having a degree of k. The $P(k)$ of lattice is Dirac delta peaked at the average connectivity of $\langle k \rangle$ as all nodes share this degree. Lattices can be defined in 1 dimension (1D), as *chain* or a *ring*, or more complicated shapes, like a square for instance, in higher-dimensional lattices. An example 1D ring lattice made up of $N = 10$ nodes is shown with its degree distribution in Fig. 1.1. This class of networks is also characterized by a high *clustering coefficient*, which measures the level of *connectedness* (or *embedding*) of the nodes in their respective neighbourhoods.

1.1.2 Random networks

A lot of the networks that are observed in the real-world are not regular and appear to connected randomly. The network of acquaintances at a cocktail party serves as a hypothetical example of such a network. The initially disconnected N nodes start to form random connections and after a certain number of links (of order N) the network becomes a completely connected graph, i.e., any arbitrary node is reachable from every other node in a finite number of steps.

Random networks models, also known as *Erdös-Rény* (ER) networks, aim to reproduce the features of these networks by characterizing those that are truly random [57]. One recipe, and definition, of a random network, is similar to the cocktail party example above. Starting from N isolated nodes, each one of the total, $N(N-1)/2$, pairs of nodes are with linked with a chosen

probability p. This results in a binomial distribution of degrees from which properties like the expected connectivity of $\langle k \rangle = p(N-1)$ and a variance $\sigma_k^2 = p(1-p)(N-1)$ can easily be calculated. An example ER network of $N = 100$ nodes generated with a connection probability of $p = 0.2$ is shown in Fig. 1.2. Random networks have found many applications in fields such as gene regulatory networks in genetics [68], ecology [69] and is prominent in modelling human-related networks like the human mobility networks [70].

1.1.3 Small word networks

Small world networks are between regular networks like lattices and fully random networks. The network generation recipe was proposed by Watts and Strogatz (WS) and serves to compensate for an important shortcoming of the purely random ER networks [56]. ER networks exhibit a small *average path length* (or shortest node-to-node distance), which is the average number of steps it takes to go from one node to another in the network. This small average path length given the size of networks is known as the *small world phenomenon* as was initially hypothesised and popularized in a series of empirical experiments in social networks (*six degrees of separation*) [71]. However real-world networks tend to be characterized by densely connected clusters in addition to the small average path lengths.

The WS network model for network generation creates a class of random networks that can reproduce both the small average path lengths and the high clustering of networks by interpolating between a regular and a random network. The model start by creating a ring of connected N nodes where each neighbour is connected to a specified k neighbours. Each link is then rewired randomly with a *rewiring probability* p. The presence of just a few long-range links, created in the random rewiring, introduces the small world effect to regular lattices. The gradual transition from a regular lattice, $p = 0$ to a fully random $p = 1$ is reflected in the degree distribution as a gradual flattening as shown in Fig. 1.4. This wide scope of WS networks has made it one of the most studied models in network science, finding applications in many fields, for instance, ecology [72], biology [73] and neuroscience [74] to name a few. They are particularly prominent with problems on social and human networks such as epidemiology [75] or opinion dynamics [76] and man-made networks such as power girds [77] and communication networks [78].

1.1.4 Scale-free networks

Another interesting class of networks structure that is prevalent in many real-world systems are *scale-free networks*. These are networks characterised by a power-law degree distribution, $P(k) \propto k^{-\gamma}$, where γ is known as the *degree exponent*. This class of networks capture a distinctive feature of many real-world networks that are irreproducible by random networks. One example of a scale-free network is the WWW which is one of of the largest networks ever created by humans. It was shown to have a relatively small number of highly connected nodes, *hubs* holding numerous low degree nodes together. The existence of hubs is not possible through a random generation of the network. Motivated by this, Barabási and Albert proposed *preferential attachment*, as a mechanism for the generation of scale-free networks and as an explanation for the existence of the *scale-free property* in real-world networks like the internet at the router level [53].

Preferential attachment is the idea that new nodes joining the network are far more likely to connect to the conspicuous, highly connected hubs than the low degree nodes. While preferential attachment is by far the most popular generative scheme, there have been others proposed that try to account for deviations of observed networks from the pure scale-free model [79; 80]. There are many examples of scale-free networks in the real-world ranging from transportation networks [81] and cell regulatory networks [82], to financial networks[83] and scientific collaboration networks [84]. Chapter 5 also finds evidence for the existence of a scale-free network in the brains of zebrafish. All scale-free network are found within values for γ that are between 2 and 3, as these mark two critical points in such networks. The existence of the hubs also have the effect of radically reducing the average path length compared to random networks creating an *ultra small-world effect*.

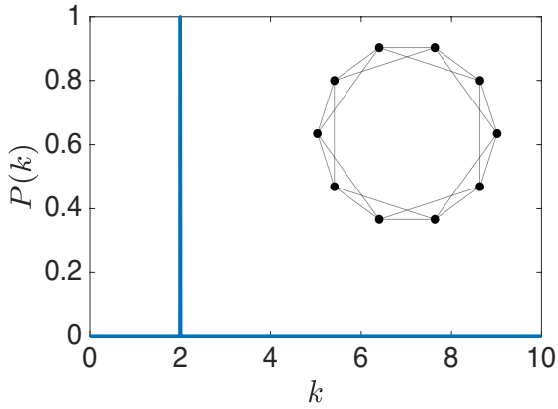

Figure 1.1: Shows the degree distribution $P(k)$ of lattice network of size $N = 10$ where every node is connected to exactly $\langle k \rangle = 2$ neighbours. The network is depicted in the inset.

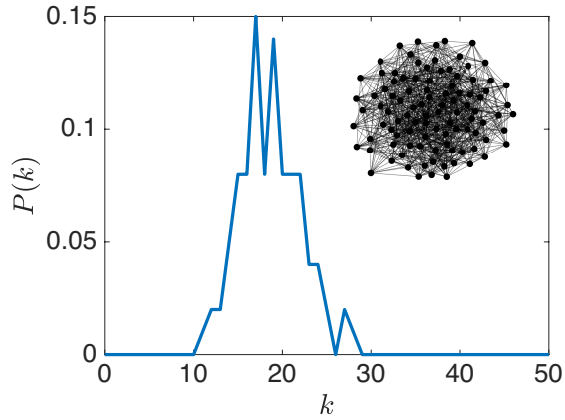

Figure 1.2: Shows the degree distribution $P(k)$ of an Erdös-Rény network of size $N = 100$ and connection probability of $p = 0.2$. The average connectivity is $\langle k \rangle = 19.8$ with a variance of $\sigma_k = 3.98$. The network is depicted in the inset.

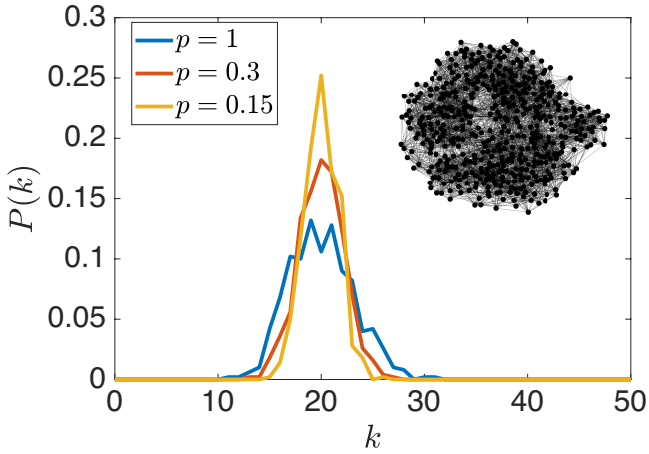

Figure 1.3: Shows the degree distribution $P(k)$ of Watts-Strogatz networks of size $N = 500$ nodes generated with 3 different rewiring probabilities p. An example network is shown in the inset.

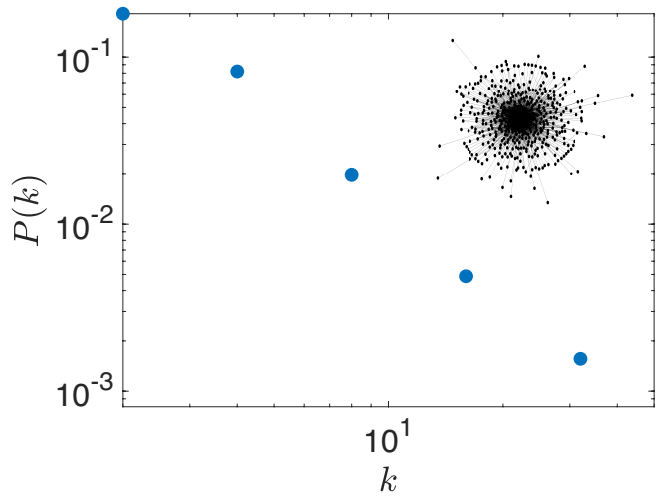

Figure 1.4: The blue dots show the degree distribution $P(k)$ of a scale-free network of size $N = 500$ nodes generated with a degree exponent of $\gamma = 2.2$. The network is shown in the inset.

Chapter 2

Reactive Explorers to Unravel Network Topology

In several cases of interest, punctual entities, also termed agents, may jump from one node to any of its adjacent neighbours, following the intricate network's architecture. Agents relocating across the network via multiple successive jumps are said to execute a random walk: their asymptotic distribution convey important information on the inherent organization of the underlying network. If walkers do not interact with each other, their steady-state distribution reflects in fact the degree of connectivity of the nodes, a direct measure of the number of links possessed by any given node of the collection. Photographing the asymptotic nodes' occupancy, enables hence to reconstruct the distribution of connectivities, a topological quantity of paramount importance when aiming at classifying the characteristics of the underlying graph. Indeed, the structure of the network is often unknown and several methods have been devised in the literature to recover it, from functions back to structure, a non-trivial task that hides formidable challenges [85; 86; 87; 88; 89; 90; 91; 92; 93]. Efficient schemes should gather the necessary information from a limited number of nodes, as monitoring the population on each vertex becomes virtually impracticable, for large network sizes.

In a recent paper [94] a variant of the random walk problem was introduced which accounts for the mutual interference between agents, as stemming from the competition for the available space in crowded operating condition [43; 44; 95; 96; 97; 98; 99; 100; 101]. Nodes are assigned a finite

carrying capacity, a sensible constraint which makes walkers dynamically intertwingled, through dedicated nonlinear terms. The asymptotic density distribution of walkers in the presence of crowding differs significantly from that obtained under diluted conditions. In crowded conditions, the equilibrium concentration saturates for large enough values of the connectivity. This observation opens up the perspective of recovering the unknown distribution of connectivities from repeated single-node measurements of the asymptotic dynamics, at increasing crowding. The nonlinearities that originate from the interference among microscopic agents competing for space is the key of success to the proposed approach.

In this chapter, we build on this achievement and generalize the method to the setting where agents perform standard, hence linear, diffusion, but the nonlinearity comes from a local reaction term. In the first part of this chapter, in Section 2.1, we introduce the mathematical framework and model in which the relative strength of the reaction and diffusion contributions is weighted by a scalar control parameter. Different equilibria are attained by the system, by modulating the latter parameter, and reflecting the interplay between reaction and diffusion terms. The equilibrium distribution is sampled by punctual measurements performed on just one node. The information gathered on the observation node is used to predict the stationary density as displayed by the system, via a direct implementation of the celebrated Heterogeneous Mean Field (HMF) approximation [20; 102; 103]. In Section 2.2 we present the inverse protocol by showing that the entries of the sought distribution link the solution, as obtained within the HMF working ansatz, to the average density sampled on the reference node. Solving the ensuing linear problem with standard optimization tools, returns a rather accurate estimate of the distribution of connectivity, as we shall prove for a selected gallery of test network models.

In Section 2.3, we consider a variant of the model by accounting for the presence of a source where the reactive constituents are injected, at a rate that we assume to be modulated as a stepwise function of time. This allows for the fixed point to be successively tweaked, as required by the reconstruction scheme here developed. In our application, the reaction model is assumed of the logistic type and it is therefore tempting to ideally interpret the reactive explorers, as living entities crawling on the unknown network support.

2.1 The mathematical framework

Label with x_i the concentration of the reactive species on node i. The dynamics of the system that we shall examine is governed by the following set of ordinary differential equations:

$$\dot{x}_i = \alpha f(x_i) + (1-\alpha)\sum_{j=1}^{N} L_{ij}x_j \tag{2.1}$$

where $L_{ij} = \frac{A_{ij}}{k_j} - \delta_{ij}$ are the entries of the random walk Laplacian operator $\mathbf{L}$; $\mathbf{A}$ is the adjacency matrix of the (undirected) network, while $k_i = \sum_j A_{ij}$ denotes the connectivity (or degree) of node i. The scalar parameter $\alpha \in [0,1]$ gauges the relative weight of the two terms, appearing on the right hand side of the above equation. In the following, we will operate under an idealized setting and assume that α can be freely tuned within the interval of pertinence. This choice has pedagogical value, and builds on the analysis in [42]: when $\alpha = 0$ the reaction term is silenced and the agents behave as standard linear walkers. By making α progressively larger, nonlinearities gain in relevance. The linear problem that is obtained when $\alpha = 0$ can be solved analytically. By direct inspection, it is immediate to conclude that, at equilibrium ($\dot{x}_i = 0$), $x_i = k_i / \sum_j (k_j)$. When nonlinearities come into play ($\alpha \neq 0$), the complexity of the problem rises considerably and no closed form solutions exist in general. Approximate techniques can be however put forward, to access information on the asymptotic fate of the system. In particular, for relatively small values of α it can be reasonably hypothesized that the displayed concentration is still arranged in classes of connectivities, as it happens in the reference setting of a pure random walk ($\alpha = 0$). This working ansatz motivates recasting the problem at hand in the form:

$$\dot{x}_k = \alpha f(x_k) + (1-\alpha)\left[k\sum_{k'} P(k' \mid k)\frac{x_{k'}}{k'} - x_k\right] \tag{2.2}$$

where x_k stands for the density displayed by the nodes that share the connectivity k. The discrete index k runs from 1 to k_{max}, where k_{max} stands for the largest connectivity, as exhibited by the network being analyzed. $P(k' \mid k)$ is the conditional probability that a link exists from a given class k to a class k'. In (2.2) we have implicitly assumed that the nonlinear contribution $f(x)$, can be also organized in classes $f(x_k)$, as reflecting the degree of connectivity associated to individual nodes. While this is not true in general,

it can be reasonably postulated as long as α is forced small, i.e. when the system under scrutiny is a perturbation to the linear random walk problem. Neglecting correlation among node degrees, one can break the probability as $P(k' \mid k) = \frac{k'P(k')}{\langle k \rangle}$, where $\langle k \rangle = \sum_k kP(k)$ and $P(k')$ is the connectivity distribution. This latter condition constitutes the core of the celebrated Heterogeneous Mean Field (HMF) approximation, to which we shall make extensive reference in the following. A straightforward manipulation yields

$$\dot{x}_k = \alpha f(x_k) + (1-\alpha)\left[\frac{k}{\langle k \rangle}\sum_{k'} P(k')x_{k'} - x_k\right] \tag{2.3}$$

Introduce now the quantity $\Theta = \frac{1}{\langle k \rangle}\sum_{k'} P(k')x_{k'}$ which enables one to recast the previous equation in the compact form:

$$\dot{x}_k = \alpha f(x_k) + (1-\alpha)[k\Theta - x_k] \tag{2.4}$$

Θ is a collective mean-field variable, which allows to formally decouple the dynamics, as seen on different nodes, grouped in classes of homologous connectivity. Stated differently, the knowledge of Θ is sufficient, under the range of validity of the HMF approximation, to solve for the densities at any time and for all degree classes k. In the following, we will focus on the equilibrium solution, which in turn amounts to setting $\dot{x}_k = 0\ \forall k$. We will then label with $\bar{x}_k$ the fixed points as displayed by the system and, consequently, $\bar{\Theta} = \frac{1}{\langle k \rangle}\sum_{k'} P(k')\bar{x}_{k'}$. Further, we will assume the nonlinear function $f(\cdot)$ to be of the logistic type, and thus set $f(\bar{x}_k) = \bar{x}_k(1-\bar{x}_k)$. This is not a mandatory step for the forthcoming analysis, as any generic nonlinear function would serve equally well the scope [1]. The advantage of using a logistic equation resides in that it allows for explicit analytical progress to be made.

From Eq. (2.4), at the fixed point, one gets:

$$\bar{x}_k = \frac{(2\alpha-1) \pm \sqrt{(2\alpha-1)^2 + 4\alpha[(1-\alpha)k\bar{\Theta}]}}{2\alpha} \tag{2.5}$$

To elaborate on the fundamental interest of Eq. (2.5), we consider a numerical implementation of system (2.1), assuming a random network made of $N = 200$ nodes (see caption of Fig. 2.1) as the backbone support. Starting out of equilibrium, the system evolves towards a fixed point, as it can be appreciated by visual inspection of Fig. 2.1. Trajectories stemming from nodes

[1] The only request is the existence of a stable fixed point and the boundedness of orbits to avoid escaping solutions.

sharing the same connectivity cluster together, thus confirming a posteriori the validity of the HMF ansatz. The asymptotic attractor as attained by the system in its late time evolution can be effectively estimated by resorting to relation (2.5). More specifically, we select a randomly chosen node of the pool, with degree k^*, and measure the density therein displayed, $\bar{x}_{k^*}$. By inversion of (2.5) one gets an estimate for the mean-field variable $\bar{\Theta}$ as:

$$\bar{\Theta} = \frac{\alpha \bar{x}_{k^*}^2 - (2\alpha - 1)\bar{x}_{k^*}}{(1-\alpha)k^*} \tag{2.6}$$

This latter is then inserted in equation (2.5) to predict the equilibrium solution $\bar{x}_k$ for all choices of the class index k. The predicted values are depicted in Fig. 2.1 with a symbol (crosses) and match the equilibrium solution as obtained by direct integration of the dynamics. This observation forms the basis of the scheme of inversion that we shall outline in the following. We remind that the inverse scheme is ultimately targeted to reconstructing the distribution of connectivity of a network, *a priori* unknown, that happens to host the inspected dynamics. Moreover, the number of necessary information is to be gathered on just one node.

2.2 The inverse protocol

The procedure that we shall illustrate builds on the following recipe. Imagine to perform a series of experiments by tuning progressively the parameter α, in discrete, ascending steps. The sequence of the experiments is indexed by r, which ranges from 1 to at least k_{max}. In each experiment, the system is let to equilibrate, and the corresponding density $\bar{x}_{k^*}^{(r)}$ is recorded on a node of class k^* where the inspection is performed. From the knowledge of $\bar{x}_{k^*}^{(r)}$ one can infer an estimate of $\bar{\Theta}_r$, which can be used to access an approximate measure of $\bar{x}_k^{(r)}$, for $k \neq k^*$, by means of Eq. (2.5). Combining this information together, and recalling the definition of Θ, results in a linear problem for the unknown entries of the q-component vector $\vec{P} = (P(1) \dots P(q))$. In formulae:

$$\langle k \rangle \begin{bmatrix} \bar{\Theta}_1 \\ \vdots \\ \bar{\Theta}_q \end{bmatrix} = \underbrace{\begin{bmatrix} \bar{x}_1^{(1)} & \cdots & \bar{x}_q^{(1)} \\ \vdots & \ddots & \vdots \\ \bar{x}_1^{(q)} & \cdots & \bar{x}_q^{(q)} \end{bmatrix}}_{\doteq \mathbf{\Gamma}} \begin{bmatrix} P(1) \\ \vdots \\ P(q) \end{bmatrix} \tag{2.7}$$

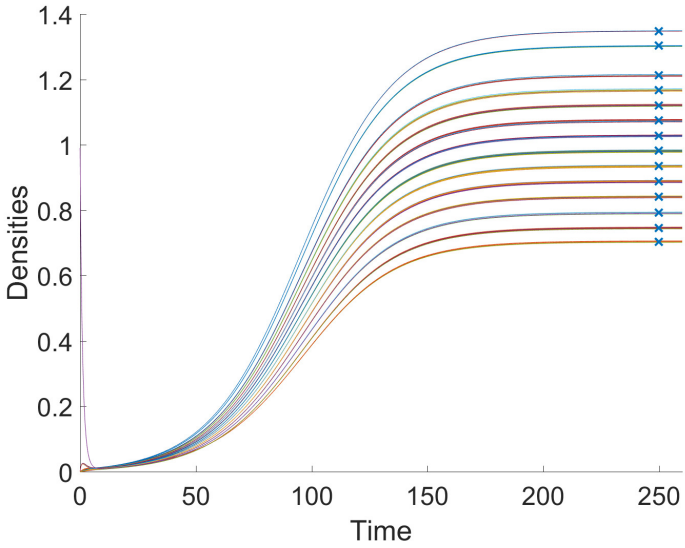

Figure 2.1: Densities x_i are plotted against time, starting out-of-equilibrium and assuming a random Watts-Strogatz network with relocation probability $\beta = 0.99$ and $N = 200$ nodes. Solid lines refer to a direct integration of the governing Eqs. (2.1), while symbols (crosses) stand for the HMF-based prediction, obtained following the procedure described in the main text. All 200 trajectories are displayed and cluster in families of homologous connectivity k, Each solid curve in the graph corresponds exactly to a given connectivity class. Here, $\alpha = 0.05$.

Solving the above problem for $(P(1) \dots P(q))$ implies inverting the matrix $\mathbf{\Gamma}$, a task that proved numerically cumbersome, being $\mathbf{\Gamma}$ poorly conditioned. To overcome this limitation we resorted to an optimization approach, which enforced the minimization of the norm $\|\vec{\Theta}\langle k\rangle - \mathbf{\Gamma}\vec{P}\|$, while imposing the entries of $\vec{P}$ to be positively defined. Here, $\vec{\Theta} = (\Theta_1 \dots \Theta_q)$. The average connectivity $\langle k\rangle$ is *a priori* unknown and it is therefore assumed, as a free control parameter in the optimization scheme. More specifically, we set $\langle k\rangle$ to a nominal value and run consequently the optimization protocol, recording as an output the quantity $\sum_{k'} P(k')$. An implicit requirement of the analysis that leads to (2.5) is the normalization of the distribution of connectivity, $\sum_{k'} P(k') = 1$. Among the solutions that are found by solving the problem in norm for different $\langle k\rangle$, we select the one that minimizes the positive residue $(1 - \sum_k P(k))^2$. By invoking this closure of the scheme, we also get an

estimate for the average connectivity $\langle k \rangle$. This latter could be challenged against the true values in synthetic network model, in the aim of testing the adequacy of the proposed procedure [2].

To this end, we begin by considering the model (2.1) defined on a random network made of $N = 200$ nodes. The network is generated with the Watts-Strogatz recipe [56], for a large relocation probability, which makes the network completely random. The average connectivity is $\langle k \rangle = 20$. We performed $q = 75$ different measurements, sampling the dynamics on the very same node and letting α to change in uniform steps in the interval $[0.005, 0.4]$. In Fig. 2.2 the normalization error $\left(1 - \sum_k P(k)\right)^2$ is depicted against the imposed average connectivity. A clear minimum is displayed, for approximately the correct value of $\langle k \rangle$.

Setting $\langle k \rangle$ to the value that minimizes the normalization error returns the distribution of connectivity depicted in Fig. 2.3. The blue line (with diamonds) stands for the true distribution, while the red curve (with dot markers) refer to the reconstructed profile. Changing the node from which the dynamics is sampled yields different estimates of the average connectivity $\langle k \rangle$ (and of the distribution that is consequently recovered). To provide a qualitative illustration of the degree of variability that stems from an arbitrary choice of the reference node, we plot in Fig. 2.4(a) the histogram of $\langle k \rangle$, as obtained for all possible selections of the observation site. The distribution of predicted average connectivity is peaked around the correct solution. To further challenge the reconstruction scheme we also monitored the root mean square deviation between the reconstructed $(P(k)^{rc})$ and the exact $(P(k)^{ex})$ profiles. This latter quantity is labelled σ and formally defined as $\sigma = \sqrt{\sum_k \left(P(k)^{ex} - P(k)^{rc}\right)^2 / q}$. The histogram of the values of σ obtained when changing the observation nodes is depicted in Fig. 2.4 (b) and points to the adequacy of the proposed scheme. To improve on the accuracy of the method one can repeat the measurements on different sites and combine together the acquired information. This significantly improves on the ability of the HMF approximation to adhere to the exact asymptotic solution, as seen in direct simulations. In Fig. 2.5 the reconstruction procedure is tested for a Watts Strogatz network with a smaller relocation probability and the quality of the reconstruction is still satisfying.

[2] In principle, one could absorb $\langle k \rangle$ in the definition of P_k, compute the rescaled entries $\tilde{P}_k = P_k / \langle k \rangle$ via the linear problem and enforce a posteriori the normalization. This scheme proved however less stable than the one that we have illustrated in the main body

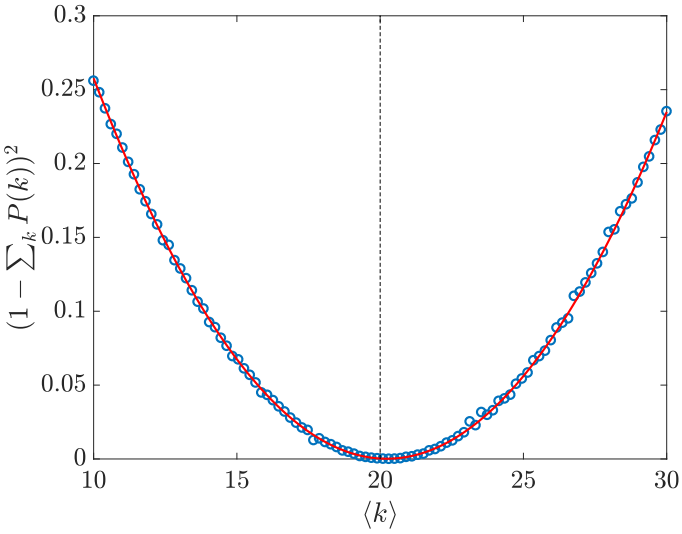

Figure 2.2: The normalization error $\left(1-\sum_k P(k)\right)^2$ is plotted against the value of $\langle k \rangle$ imposed when running the inverse scheme. A clear minimum is displayed for $\langle k \rangle \simeq 20$, which is very close to the correct value of the average connectivity ($\langle k \rangle = 20$). The reconstruction procedure is hence able to single out the correct average connectivity as possessed by the network being analyzed. The solid line is obtained by fitting a parabola to the collected data.

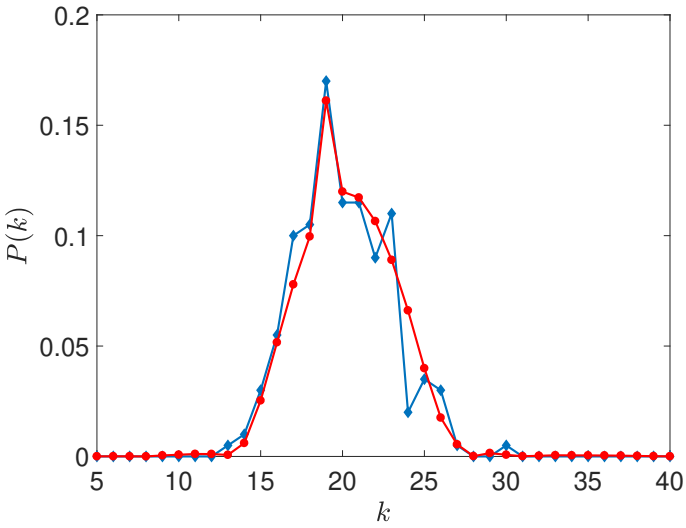

Figure 2.3: The reconstructed distribution of connectivities: the blue line (with the diamond markers) represent the true degree distribution. The red line (with dot markers) stands for the distribution reconstructed via the procedure described in the main text. Here, 75 independent experiments are employed and the dynamics is sampled from just one node of the collection. The network is generated according to the Watts-Strogatz recipe with relocation probability $\beta = 0.99$. Here, $N = 200$

To further elaborate on the potential of the described procedure we considered a scale-free network made of $N = 500$ nodes. More specifically $P(k) \propto k^{-\gamma}$ with $\gamma = 3$. The $P(k)$ is correctly recovered following the method, as displayed in Fig. 2.6. The distribution of $\langle k \rangle$ is obtained by sampling the dynamics on all possible observation sites is shown in Fig. 2.7(a). At variance to the case of the random network analyzed above, changing the reference node impacts more significantly on the recorded $P(k)$, as seen from the histogram of σ in Fig. 2.7(b) (while $\langle k \rangle$ is correctly estimated). However, we could not identify any significant correlation between the error displayed by the reconstruction and the topological characteristics of the observation node (as e.g. its degree). Averaging independent profiles obtained by sampling the dynamics from distinct nodes contributed to enhance the fidelity of the reconstruction.

---

of the paper.

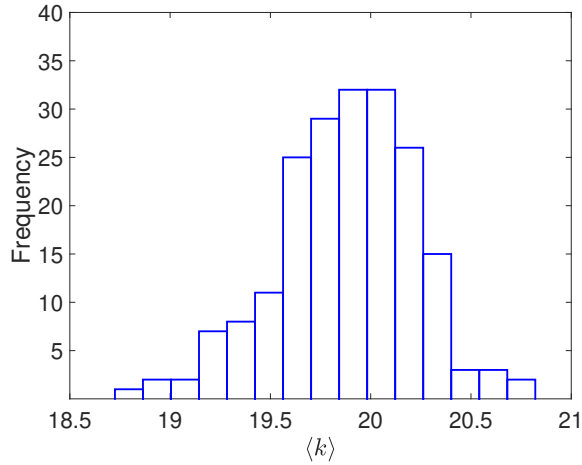

(a)

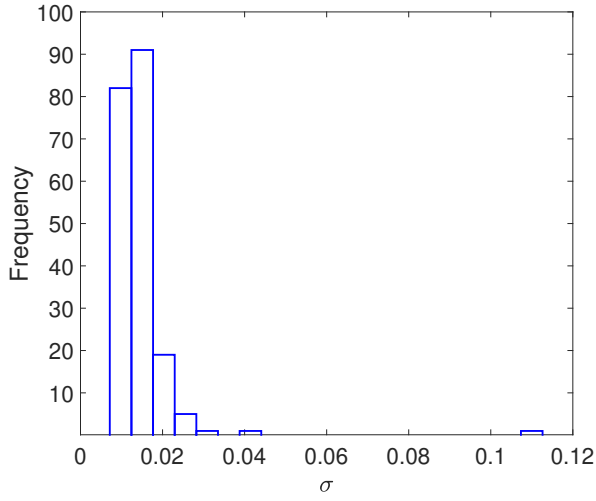

(b)

Figure 2.4: (a) The histogram of the averaged connectivity $\langle k \rangle$ is displayed. Each value of $\langle k \rangle$ refers to a different selection of the node from which the dynamics is sampled. (b) The histogram of the root mean square error in reconstruction σ is plotted. Each value of σ refers to different observation nodes.

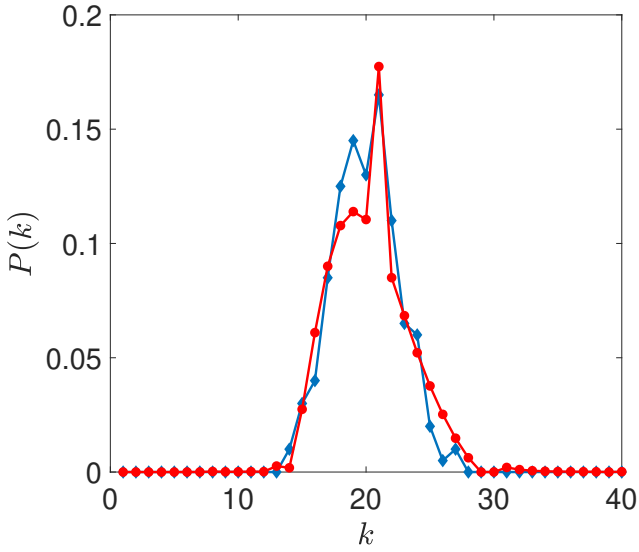

Figure 2.5: The reconstructed distribution of connectivities, for a Watts-Strogatz network with relocation probability $\beta = 0.5$ and $N = 200$. Symbols are chosen as explained in the caption of Fig. 2.3.

Summing up to this point, we have introduced and successfully applied a procedure to reconstruct the distribution of connectivity of an unknown network by performing local measurements on just one node. The inspected system combines nonlinear reactions to relocation. The method implemented requires adjusting a control parameter which sets the relative strength of the two aforementioned contributions, a condition that might prove difficult to meet in real experiments. To overcome this limitation and formulate a reconstruction scheme which could be viably implemented, we will hereafter consider a slightly modified version of the examined dynamical process. More precisely, we will accommodate for the presence of a set of sources, where the interacting elements can be injected at a given rate to be externally tuned.

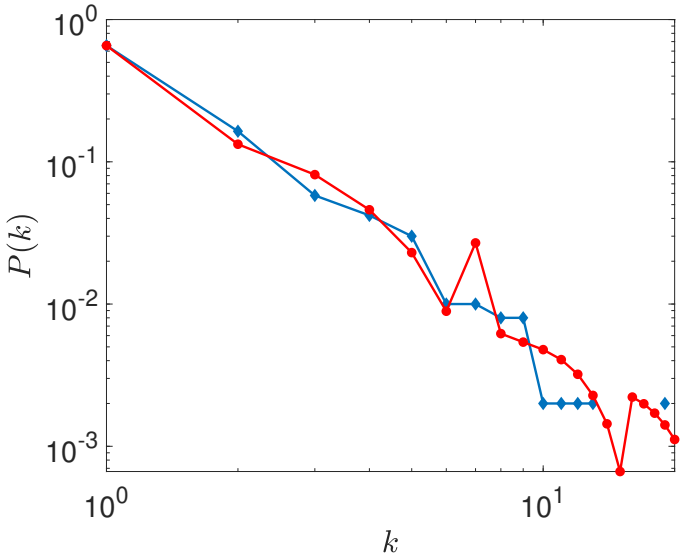

Figure 2.6: The reconstructed distribution, assuming a scale free network. The network consists of 500 nodes. Here, $P(k) \propto k^{-\gamma}$ with $\gamma = 3$. Symbols follows the convention introduced in Fig. 2.3

2.3 Introducing the sources and modulating their strengths

The updated scheme builds on the following steps. First, we freeze α to a constant amount. Then, we modify the dynamics of a given class of nodes, say those characterized by a connectivity $\hat{k}$, by introducing an ensemble made of identical sources, characterized by a constant injection strength η. Mathematically, this corresponds to inserting on the right-hand side of Eq. (2.1) a constant factor η, for the entries i which identify the selected pool of nodes. For any given choice of η, the asymptotic fate of the system can be analytically investigated by proceeding with the HMF approximation, in analogy with the results reported above. Formally, one ends up with an expression for the fixed point which trivially extends that displayed in Eq.

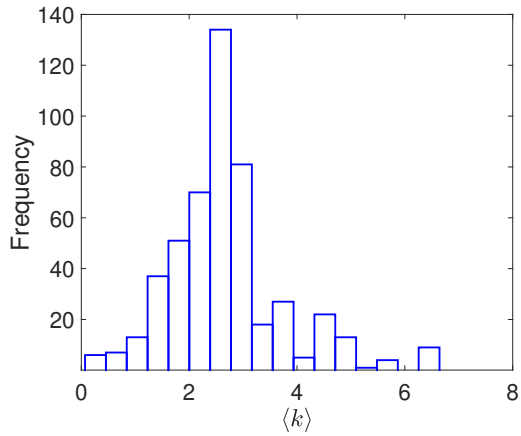

(a)

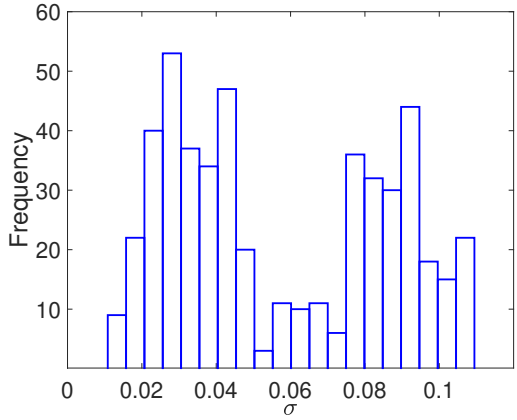

(b)

Figure 2.7: (a) The histogram of the reconstructed averaged connectivity $\langle k \rangle$ is plotted, for a scale free network. Each value of $\langle k \rangle$ refers to a different selection of the node from which the dynamics is sampled. (b) The histogram of the root mean square error in reconstruction σ is represented. Each value of σ refers to different observation nodes.

(2.5):

$$\bar{x}_k = \frac{(2\alpha - 1) \pm \sqrt{(2\alpha - 1)^2 + 4\alpha[(1-\alpha)k\bar{\Theta} + \eta\delta_{k\hat{k}}]}}{2\alpha} \tag{2.8}$$

where $\delta_{k\hat{k}}$ stands for the Kronecker delta.

The reconstruction scheme can be hence modified as follows: (i) change η within a given interval; (ii) for each choice of η, measure the asymptotic state attained by the system on a given node with degree $k = k^*$; (iii) use this knowledge to estimate the mean-field variable $\bar{\Theta}$, by inversion of Eq. (2.8) and, finally, (iv) predict the equilibrium solution $\bar{x}_k$, $\forall k \neq k^*$. Repeating this procedure for a sufficiently large set of distinct values of η, yields a linear problem of the type (2.7) which can be solved in norm to compute $\vec{P} = (P(1) \dots P(q))$. Also in this case the average connectivity is estimated by minimizing the residual error. As a demonstrative example, we compare in Fig. 2.8 the reconstructed $P(k)$ to its exact homologue. Here, the underlying network is generated according to the Watts-Strogatz recipe and the agreement between the two depicted curves is satisfying.

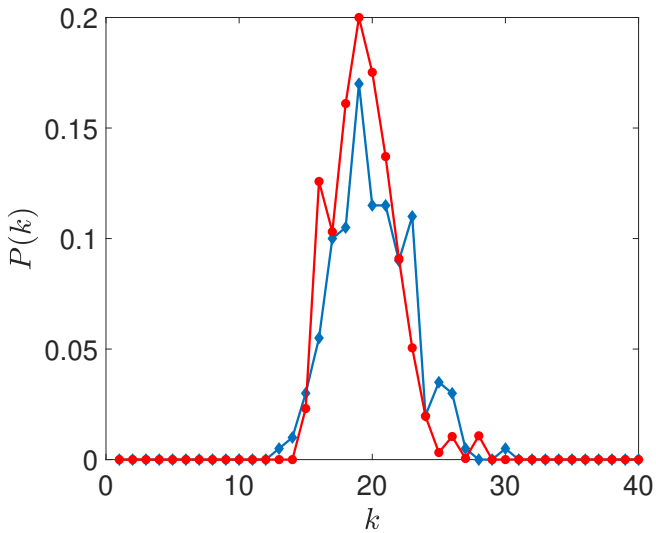

Figure 2.8: The reconstructed distribution of connectivities: the blue line (with the diamond markers) stands for the true degree distribution. The red line (with dot markers) identifies the distribution reconstructed via the procedure described in the main text. Here, $\alpha = 0.005$ and η is changed in the interval $[0.005, 5.5]$ with uniform increments of 0.2. The sources are placed on the nodes sharing degree $\hat{k} = 15$ (the results do not depend on this specific choice). This class contains 7 different nodes, for the network realization here considered. The network employed is that of Fig. 2.3.

In Fig. 2.9 we report the histogram of σ, the root mean square error of the reconstructed profile against the exact one. Each curve refers to a different choice of the nodes that act as sources. The corresponding ensemble of σ is obtained by changing the observation node, for each source selection. The results are quite consistent and point to the overall validity of the proposed method. The connectivity of the selected sources is, respectively, $\hat{k} = 15, 20, 25$, and it does not influence significantly the performance of the reconstruction algorithm.

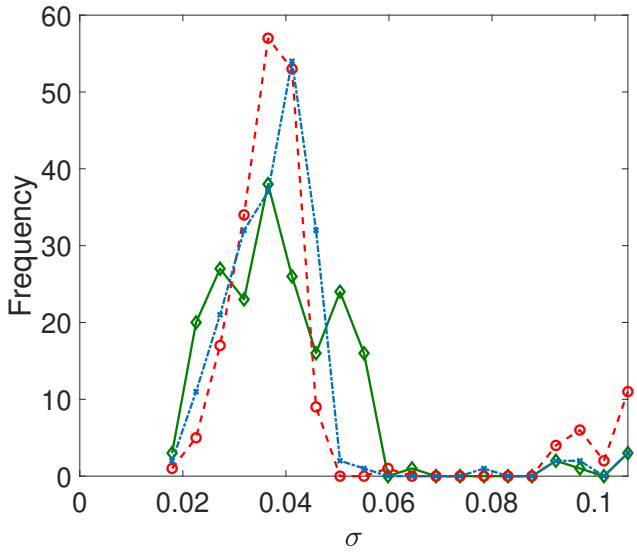

Figure 2.9: The histogram of σ is plotted. Each curve refers to a specific choice of the source nodes. More specifically, the green line with diamond markers is obtained by setting the sources on the nodes that share connectivity $\hat{k} = 15$. The red dashed line with circle markers refers to $\hat{k} = 20$ and the dash-dotted blue line with crosses stands for $\hat{k} = 25$. For each sourcesâ selection, we perform the reconstruction by sampling the dynamics on different observation nodes and quantify the associated error σ.

As a final point, we will relax the assumption of dealing with a full class of nodes which behave as identical sources. More precisely, we will break the symmetry and assume that just one node of a given class $\hat{k}$ acts as a source. To handle this generalized setting, we revisit the definition of the mean field variable. Recall that $P(\hat{k})$ measures the number of nodes sharing connectivity $\hat{k}$ normalized to the system size N. Then one can define the

following collective variable:

$$\Pi = \frac{1}{\langle k \rangle} \left[\sum_{k'} P(k') x_{k'} + \frac{y - x_{\hat{k}}}{N} \right] \tag{2.9}$$

where y denotes the value of the density at the source location. One can apply the HMF machinery[3] to yield:

$$\bar{x}_k = \frac{(2\alpha - 1) \pm \sqrt{(2\alpha - 1)^2 + 4\alpha(1 - \alpha)k\Pi}}{2\alpha} \tag{2.10}$$

for the fixed point concentration as predicted on all nodes, but the source. This latter is characterized by an asymptotic density given by:

$$\bar{y} = \frac{(2\alpha - 1) \pm \sqrt{(2\alpha - 1)^2 + 4\alpha[(1 - \alpha)k\Pi + \eta]}}{2\alpha} \tag{2.11}$$

Building on the above, one can put forward a straightforward generalization of the reconstruction algorithm. For any given choice of the source injection rate η, one can measure the equilibrium density as displayed on one individual node, belonging to class k^*. By manipulating Eq. (2.10), one can then estimate Π and use this latter to predict the expected density on each of the classes ($\bar{x}_k$, $k \neq k^*$) and on the source ($\bar{y}$). To this end one makes explicit use of, respectively, Eqs. (2.10) and (2.11). Repeating the analysis for a sufficiently large set of η returns a linear problem of the type discussed above, with the sole difference that now the size of the network N qualifies as one of the unknowns to be eventually recovered. In formulae, Eq. (2.9) can be cast in the form:

$$\langle k \rangle \Pi = \sum_{k'} P(k') x_{k'} + \frac{z}{N}$$

where $z = y - x_{\hat{k}}$. We hence get:

$$\langle k \rangle \begin{bmatrix} \bar{\Pi}_1 \\ \vdots \\ \bar{\Pi}_q \end{bmatrix} = \begin{bmatrix} \bar{x}_{k_1}^{(1)} & \cdots & \bar{x}_q^{(1)} & \bar{z}_1 \\ \vdots & \ddots & \vdots & \vdots \\ \bar{x}_1^{(q)} & \cdots & \bar{x}_q^{(q)} & \bar{z}_q \end{bmatrix} \begin{bmatrix} P(1) \\ \vdots \\ P(q) \\ \frac{1}{N} \end{bmatrix} \tag{2.12}$$

[3] In doing so we postulate that the inserted source does not disrupt the organization in classes. The validity of this working ansatz is confirmed a posteriori by the quality of the obtained reconstruction.

where q ($> k_{max}$) stands for the number of repeated measurements performed at different choices of η. The reconstruction obtained following this updated strategy is displayed in Fig. 2.10, for the same realization of the Watts-Strogatz network as considered above. The quality of the reconstruction is still adequate and the estimated value of N is in agreement with the true one. The performance of the algorithm may change depending on the node of observation but the distribution of N obtained when covering the full set of possible choices is peaked in correspondence of the correct value as shown in Fig. 2.11(a). Similarly, in Fig. 2.11(b) the distribution of $\langle k \rangle$, the average value of the reconstructed connectivity, extends over a finite domain which contains the correct value.

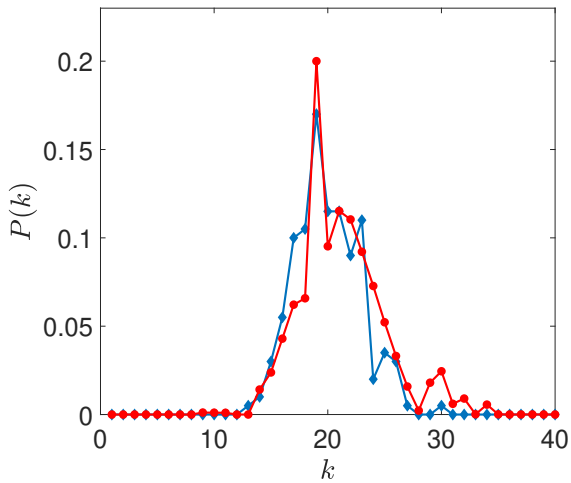

Figure 2.10: The reconstructed distribution of connectivities: the blue line (with the diamond markers) stands for the true degree distribution. The red line (with dot markers) identifies the distribution reconstructed via the procedure described in the main text. Here, $\alpha = 0.005$ and η is changed in the interval $[0.005, 0.35]$, with 80 successive uniform increments. The source is placed on one of the nodes sharing degree $\hat{k} = 15$. The network employed is that of Fig. 2.3.

To sum up, we have in this chapter introduced and tested a procedure to access structural information on network topology. The method samples the dynamics of reactive walkers, microscopic entities which are made to explore the embedding network, while subject to nonlinear (and local) reaction terms. The imposed non-linearity makes it possible to recover the network's

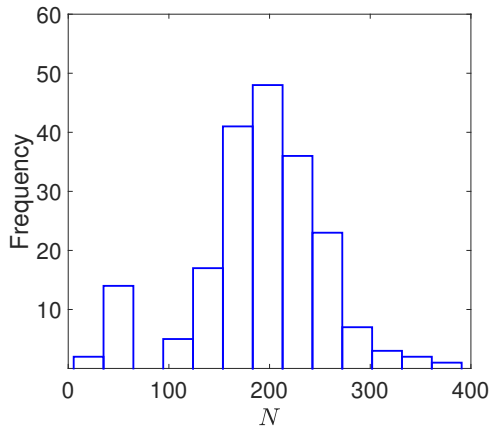

(a)

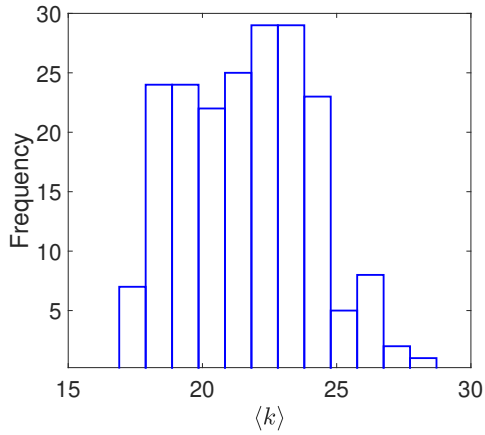

(b)

Figure 2.11: (a) The histogram of N, the reconstructed network size. Each value of N refers to distinct observation node. (b) The histogram of the reconstructed averaged connectivity $\langle k \rangle$ is plotted. Each value of $\langle k \rangle$ refers to a different selection of the node from which the dynamics is sampled.

distribution of connectivity, from sequences of measurements performed on just one node of the collection. To reach this goal, we exploit the organization in classes of the ensuing dynamical equilibrium and make explicit

use of the celebrated Heterogeneous Mean Field approximation. A variant of the method which consists in introducing localized sources of modulable strength, enables in turn to estimate the size of the scrutinized network.

Chapter 3

Cortical propagation as a biomarker for recovery after stroke

We have introduced a method for network reconstruction in the previous chapter that we rigorously challenged and validated against synthetically generated data. The inversion framework, however, is general enough to be extended to many dynamical models including ones that more readily resemble real-world phenomena in order to gain insights into the underlying connections of such systems. We use this chapter to introduce one such dataset from the field of neuroscience and present an overview of a spatiotemporal analysis[1] of this data before extending the reconstruction framework to neuronal models in Chapter 4. The data concerns the living brain activity of mice captured through a series of wide-field cortical calcium images tracking the recovery of the animals after the induction of a stroke. The images were recorded during longitudinal motor training, before and after a focal stroke induction. In addition the mice follow two different rehabilitation paradigms, motor training alone and combined with pharmacological therapy and are grouped accordingly. In the analysis that follows, we identify three novel indicators that are able to track how movement-evoked global

[1]This work was done as a collaborative effort involving many parties who have contributed far greater towards the work than the authour and does not represent his primary research activity. The names and relevant contributions can be found on the manuscript referred to in the publications section in Appendices

activation patterns are impaired by stroke and evolve during rehabilitation: the duration, angle and smoothness of individual propagation events. In the following chapter we will build upon the techniques presented here and in the previous chapter to show a different analysis of the same data which employs a refined inverse protocol strategy to similarly track the progression of the effects of the stroke immediately after induction and during recovery.

Stroke is a severe disease that alters cortical processing producing long-lasting motor or cognitive deficits. Treatments generally include motor rehabilitation, pharmacological therapies, brain stimulation, or combinations of them [104]. However, the functional outcome, measured as behavioural recovery, depends on multiple factors such as age, lesion size and type, edema formation or inflammation and is hardly predictable [105; 106]. One way to track recovery after stroke is by monitoring cortical activity, which is known to undergo drastic changes that have been tightly linked to structural alterations [107; 108; 109]. Previous studies have reported that stroke produces global widespread alterations in cortical activity as measured by changes in resting-state functional connectivity or cortical excitability. On the one hand, electrophysiological studies have shown that stroke and recovery modulate both resting state and stimulus-evoked cortical oscillations in motor areas [110; 111]. On the other hand, neuroimaging studies have shown that stroke alters the resting-state functional connectivity, for example, it reduces the interhemispheric correlations between motor networks, and these changes correlate with behavioural deficits [112; 113]. Furthermore, these changes in resting-state functional connectivity can be used to discriminate subjects with behavioural deficits [114]. This supports the idea that monitoring how cortical activity evolves over time could be used to track recovery after stroke and it could represent a powerful tool to evaluate the efficacy of stroke treatments or better yet could lead to biomarkers of functional recovery.

Advancements in neural imaging combined with genetically encoded calcium indicators allow to monitor neural activity over almost the entire cortical mantle with high spatial resolution on a sub-second temporal scale [115; 116; 117; 118]. Using these tools it has been shown that the cortical activity of animals engaged in a behavioural task is characterised by cortex-wide global activation patterns [119] and these patterns are shaped by learning across sessions [120]. In the context of stroke calcium imaging has been used to demonstrate that stroke profoundly affects resting-state

functional connectivity [121] and leads to sensorimotor remapping of the peri-infarct area [116]. Furthermore, in a recent study, we have shown that movement-related activation maps are different for stroke therapy associated with functional recovery [109]. Therefore neural activity as measured by calcium imaging could be used as an indicator of cortical remapping, of redistribution of functional connectivity among spared regions and could be directly associated with behavioural recovery.

Here, we propose that damage and functional recovery can be tracked by monitoring the spatiotemporal properties of movement-evoked widespread activation patterns or global events. In particular, we use the recently proposed SPIKE-order analysis [122] to identify global events and to sort the participating regions from first to last (or leader to follower). In addition, to characterise the spatiotemporal properties of each individual global event, we extend this method and define three propagation indicators: duration, angle and smoothness, i.e., how ordered and consistent is the direction of the propagation.

First, in Section 3.1 we present an overview of the methods and the recorded data following which we define the three key indicators that will be used to characterise global events. We show that these events are mostly associated with the exertion of force and their duration and direction are modulated by different behavioural events. Then, to understand the impact of stroke on the global events we quantify the three propagation indicators in a group of acute stroke subjects. We provide evidences that acute stroke alters the propagation patterns by increasing the duration while decreasing the smoothness of the global events. Finally to test if global events propagation patterns can be used to track recovery and furthermore differentiate between treatments that lead to generalized recovery, we quantify the propagation indicators in two experimental groups with different therapies in Section 3.2. The first consisted of motor training alone and leads to task-specific improvement of the motor functions, while the second therapy combined motor training with pharmacological treatment and results in generalised recovery of the forelimb dexterity [123]. While both treatments reverse the effect of stroke on the global events propagation patterns indicators, the combined rehabilitative therapy leads to a new propagation pattern defined by the shortest duration and the highest smoothness among all experimental groups.

3.1 Methods

3.1.1 Experimental set-up and data collection

In this section, we provide a short overview of the data and the methods we used to analyse them. For more technical details please refer to the section "Materials and Methods" in Appendix A.1.

To investigate the changing propagation patterns during motor recovery from functional deficits caused by the induction of a focal stroke via a photothrombotic lesion, calcium imaging signals recorded from 17 mice were analyzed. The data was recorded during two long-term robot-assisted rehabilitation programs, one based on motor training alone (robot group) and one combined with transient pharmacological inactivation of controlesional activity (rehab group) previously validated by Spalletti and collaborators [109; 123]. A schematic representation of the robotic system, the M-Platform [124; 125], is shown in Fig. 3.1a. This system uses passively actuated contralesional forelimb extension on a slide to trigger active retraction movements that were subsequently rewarded (up to 15 cycles per recording session). The effect of the motor activity was monitored via the discrete status of the slide and by recording the force the mice applied to the slide. As a measure of the neural activity itself wide-field calcium imaging was performed over the affected hemisphere, from the somatosensory to the visual areas. Selecting a region of interest of 2.16 x 3.78 mm and spatially downsampling by a factor 3 resulted in calcium images of 12 x 21 pixels of size 180 μm. These are the signals that we analyzed.

The 17 mice were divided into three groups: control (3 mice), robot (8 mice) and rehab (6 mice). The healthy controls had no stroke-induced but still received the same type of motor training as the other mice (4 weeks on the M-Platform). Both robot and rehab mice underwent physical rehabilitation on the M-platform for 4 weeks starting 5 days after the injury.

For rehab mice, in addition a pharmacological inactivation of the primary motor cortex in the contralesional hemisphere was carried out in order to counterbalance the hyperexcitability of the healthy hemisphere. The recording schedule for all three groups is shown in Fig. 3.1b. Apart from the data acquisition during the shared training regime, 5 out of 8 robot mice were also recorded for one week before the stroke (pre-stroke condition).

Two weeks before the stroke, five mice belonging to the robot group have been trained for 5 days (pre-stroke condition), Fig. 3.1b. It was tested

whether the pre-stroke condition shows any statistical difference with the first week of recordings of the control group. As could be expected, the pre-stroke condition presents the same behaviour as the control group, both qualitatively and quantitatively.

Fig. 3.1c displays a sequence of snapshots of the calcium activity over time. The three images illustrate one pull of the slide by the contralateral forelimb of a control mouse, from the activation of the average calcium activity (left) via its maximum (middle) to its tail end (right).

The central method of this chapter was a mapping of this sequence of snapshots into the propagation pattern shown in Fig. 3.1d. In this matrix, the order of activation of the individual pixels was colour-coded from red (earliest) to blue (latest). We superimposed this order matrix on the standard atlas of brain regions [126] which illustrates that the recording area covers the primary motor area M1 (the location of the lesion), the primary somatosensory area, and the primary visual cortex, as well as the retrosplenial cortex.

3.1.2 Event identification and propagation analysis

In this section the use of SPIKE-order framework [122] to identify global events and to assess the propagation of activation within these events (refer to Fig. 3.1d) is explained. In particular, the focus again is on one individual global event to illustrate how the detailed activation patterns have been characterised with the three propagation indicators: **duration**, **angle**, and **smoothness**.

In Figure 3.2 the activity during a complete recording session of one mouse is shown. Fig. 3.2a depicts the status, a discrete codification of the current phase of the passive extension and active retraction cycle, e.g. position of the slide and acoustic go and reward cues. Most relevant here are the marked times of the pull completions which typically correspond to peaks in the force applied to the slide (Fig. 3.2b, force events are marked at threshold crossings). Notice that there are typically more force events than rewarded pull completions. The peaks in the calcium signal computed by averaging the fluorescence signal over all pixels (Fig. 3.2c,) outnumber the former.

In the next step all individual pixels are analysed but here small time markers denoting the time of the threshold crossings are shown (Fig. 3.2d). This is very similar to a raster plot showing in each row the spike train of one individual neuron and accordingly we here follow this terminology and

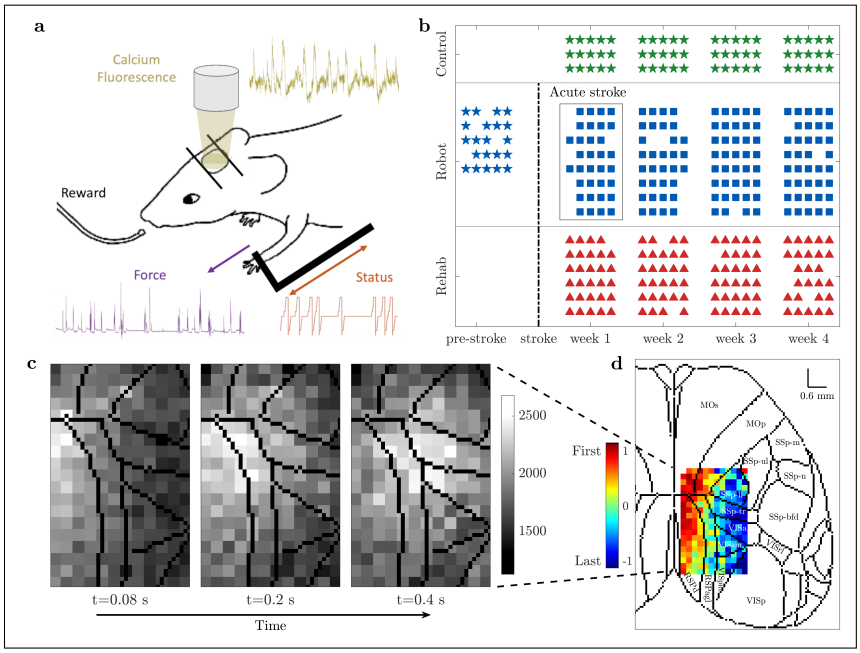

Figure 3.1: Experimental set-up and data collection. **(a)** Motor-training of mice was performed on the M-Platform, which uses a movable robotic slide for a retraction movement of the left forelimb. Motor activity was monitored via the discrete status of the slide (orange) and the force applied by the mouse to the slide (purple). Meanwhile, the cortical activity (yellow) was recorded using wide-field calcium imaging. **(b)** The control (green) and rehab (red) group performed 4 weeks of daily training; for the robot (blue) group we additionally recorded 1 week before stroke induction (typically 5 sessions per week). Star symbols refer to the healthy condition, while the two different types of rehabilitation, robot and rehab, are represented by squares and triangles, respectively. **(c)** Calcium imaging sequence of cortical activation, superimposed on contours of brain regions according to the standard atlas. **(d)** Propagation pattern, from leader (red) to follower (blue), of the event depicted in (c). Colour coding is based on the SPIKE-order (see Section SPIKE-order in Materials and Methods for details).

call the threshold crossings of individual pixels, 'spikes'. While there are a few spikes in the background (in black), most of the spikes are part of global events (in color) matching the peaks in the average calcium activity shown right above. To automatically identify these global events and sort the spikes within these events from leader to follower, we used the SPIKE-order framework proposed in [122].

After some initial denoising an adaptive coincidence detector [127] was used to pair spikes such that each spike is matched with at most one spike in each of the other pixels. By means of the symmetric and multivariate measure SPIKE-Synchronization [128], all spikes which were not coincident with spikes in at least three-quarters of the other spike trains were filtered out. To the global events that remained, the asymmetric SPIKE-order indicator [122] which quantifies the leader-follower relationship between pairs of spikes was applied. For each event the SPIKE-order is then colour-coded from leader (red) to follower (blue). Finally, the scalar Synfire Indicator [122] was used to also sort the spike trains in the raster plot from overall leader to overall follower. Since the sorting takes into account all global events, the first spike trains contain more leading spikes (red) and the last spike trains more trailing spikes (blue).

In Fig. 3.2e a zoom in on the fourth global event of the raster plot is shown. The first propagation indicator, the event **duration**, is defined as the time from the first to the last spike of this event. The propagation matrix of this specific event, obtained by projecting the colour-coded relative order of the spikes onto the pixels of the 2D-recording plane, is shown in Fig. 3.2f. Following this, a singular value decomposition (SVD) to calculate the two remaining propagation indicators was used.

SVD [129] searches for spatial patterns by decomposing the propagation matrix into three simple transformations: a rotation, a scaling along the rotated coordinate axes and a second rotation. The scaling is a diagonal matrix which contains along its diagonal the singular values of the propagation matrix. Backprojecting the (sorted) singular values, one at a time resulted in various orders of approximations for the original propagation matrix. The first two such projections are displayed in Fig. 3.2g and the second-order approximation, their weighted sum, is shown in Fig. 3.2h. From the weighted average of the mean gradients of these first two projections the second propagation indicator, the **angle** of the main propagation direction was calculated.

In Fig. 3.2i the (sorted) singular values (rescaled to the highest value) versus the order of the projection is depicted. Also shown is the value of the third propagation indicator, the **smoothness** S, which quantifies how well the approximation with only the first two singular values captures the full spatiotemporal pattern obtained by considering all singular values σ_i. Smoothness is defined as the relative weight of the first two projections, their sum divided by the sum of all singular values. This can be verified

visually by comparing the second approximation (Fig. 3.2h) with the original propagation matrix (Fig. 3.2f).

A comparison of Fig. 3.2d and Fig. 3.2c clearly shows that all global events in the raster plot can easily be matched with a peak in the average calcium trace, however, while the vast majority of global events are in close proximity of a peak in the force, not all of them are. This can be used to categorise the global events into two groups: Force (**F**) and non-Force (**nF**). Among the Force events two kinds of events are distinguishable; a few of them occur during the passive extension of the arm by the slide (Passive, **Pass**) but most of them do not, i.e., they occur during the active retraction phase (Active, **Act**). Finally, among those active events, the movements which lead to a completion of the forelimb retraction can be differentiated and therefore are rewarded (Reward Pulling, **RP**) and movements which are not completed and thus not rewarded (non-Reward Pulling, **nRP**). The Reward Pulling events are the ones that correspond to the vertical markers in the status trace of Fig. 3.2a.

The overall categorisation can be visualised by means of this branching structure:

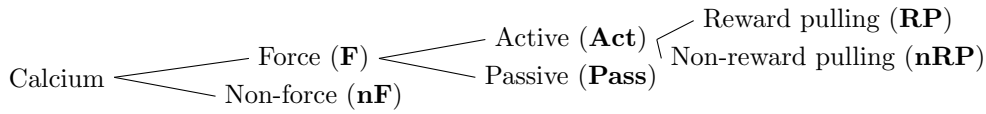

3.2 Results

In this chapter, a biomarker for functional recovery after stroke in the neural activity propagation was investigated. To this aim, a global event propagation analysis was used to investigate the spatiotemporal features of neuronal activation over the dorsal cortex. The propagation patterns in healthy versus acute stroke and after treatment mice (control, robot, and rehab groups, Fig. 3.1) was compared. It was also decided to investigate three main indicators (angle, duration, and smoothness of the propagation) to account for both spatial and temporal propagation characteristics. To identify common brain dynamics associated with similar behaviours, each event type was dealt with separately.

3.2.1 Healthy mice

The dependency of the three indicators was evaluated both over time and with respect to different event types (Fig. 3.3). For the four weeks of recordings in healthy mice, the variation of the number of events divided by type is depicted in Fig. 3.3a. Most of these events occurred when the mouse applied a force to the handle (87% of events). Furthermore, 73% of force events (64% of total) occurred when the mouse was actively pulling the handle, and 68% of active events (43% of the total) of those corresponded to reward pulling events.

Global events propagate along angles -0.3 ± 0.4 with a smoothness of 0.63 ± 0.03, and they last 0.59 ± 0.04 s (see subplot "All" of Fig. 3.3b,d,f). The little variation in the angle, smoothness and duration implies high coherence of the parameters of spatiotemporal propagation over weeks. This suggests that motor training alone does not change events number, duration, smoothness or angle along weeks.

Results for angle, smoothness and duration were then analysed looking at specific event types. Fig. 3.3g shows the distributions of the angle for the three consecutive subdivisions of the event types. The propagation becomes more directed when narrowing down the type of events. The difference between event types in the angle distribution reduces as well. Interestingly, also the bimodal nature of the distribution is attenuated. Specifically, the peak at $-\pi/2$ (see first plot in Fig. 3.3g) is initially caused by non-force events, then within force events it stands out in the passive cases, finally it is predominant in the non-reward pulling events. This suggests that task-specific events, such as reward pulling, are characterised by consistent propagation patterns. The same argument can be made for the smoothness of the propagation; further specifying the type of event leads to smoother and smoother propagation patterns (Fig. 3.3e) with the highest average smoothness being obtained for reward pulling events. They display also the shortest duration, on average, among all the other events (Fig. 3.3c).

The patterns observed in healthy mice are characterised by different spatiotemporal features when comparing force and non-force events in terms of angle ($p=10^{-10}$) and smoothness ($p=0.001$) of propagation, and when comparing active and passive events in terms of angle ($p=10^{-9}$) and duration ($p=0.002$). Also between rewarded and non-rewarded pulls events, the observed patterns display different characteristics when comparing angle ($p=10^{-8}$) and smoothness ($p=0.001$) (see Fig. 3.3c,e,g).

In summary, in healthy mice, there is a high coherence of the parameters of spatiotemporal propagation over weeks, suggesting that on a simple motor task alone does not change the angle, smoothness, and duration of events. Moreover, the investigated spatiotemporal propagation indicators discriminate between different event types when a specific characteristic is taken into account, i.e., force versus non-force, active versus passive, reward versus non-reward pulling.

3.2.2 Acute phase after stroke

The cortical activation events as associated with classes of behavioural events in the first week right after the stroke (called acute stroke) is discussed here. Moreover, these results are compared with the first week of recordings on healthy mice (Fig. 3.4) which consists of the first week of recordings of the control group and the pre-stroke week in the robot group.

When looking at all events together, the distribution of the angles for the acute stroke group exhibits a flatter distribution and two secondary peaks in $-\pi/2$ and $\pi/2$, indicating the presence of a more heterogeneous pool of events (Fig. 3.4e). Differences can be appreciated for the smoothness (p=0.007) and duration (p=0.003) even without further splitting the events into specific types. In particular, the smoothness decreases (Fig. 3.4c) and the duration increases (Fig. 3.4a) during the acute phase.

When splitting the results into event types (Fig. 3.4b,d,f), a common tendency for angle, smoothness and duration is that the stroke condition attenuates differences of the indicators between event types. For the angle (Fig. 3.4f), the dissimilarities in the control group between event types are preserved in the acute stroke condition (F-nF and Act-Pass, control p¡0.001 and robot p¡0.05). For both smoothness and duration (Fig. 3.4b,d), while the control group presents significant variations when changing the type of event (F-nF p=10^{-10} and RP-nRP p=0.008 for smoothness, and Act-Pass p=0.04 for duration), the acute stroke group is characterised by smaller fluctuations in the mean value (F-nF p=0.082 and RP-nRP p=0.51 for smoothness, and Act-Pass p=0.059 for duration). Regarding the smoothness (Fig. 3.4d), a significant difference in mean between healthy and stroke mice can be appreciated for force (F, p=0.004), active (Act, p=0.01), passive (Pass, p=0.002), and reward pulling (RP, p=0.005) events. For the duration (Fig. 3.4b), significant differences can be found in the same events types as for smoothness (p=0.026, 0.034, 0.035, 0.014) with the addition to the not reward pull (nRP,

p=0.028) events.

Altogether, the three spatiotemporal propagation indicators are able to distinguish between healthy and stroke mice. The acute phase after stroke leads to more heterogeneous events characterised by flattened distributions of the angle, lower smoothness, and longer duration. Moreover, in contrast to the healthy condition, cortical propagation features do not discriminate event types in the acute stroke condition.

3.2.3 Rehabilitation treatment

It was hypothesised that rehabilitative treatments may alter the spatiotemporal propagation patterns, and in particular reverse the trend observed in the acute stroke phase. Therefore, the spatiotemporal propagation indicators in animals treated with motor training alone (robot group) or in combination with pharmacological inactivation of the homotopic cortex (rehab group) was compared. Finally, by comparing treated (robot and rehab) with healthy mice (control group), it was evaluated whether the propagation features were restored to pre-stroke levels or if the treated condition ended in a new state (Fig. 3.5).

In this section, the data belonging to control, robot, and rehab groups starting from the second week of recording up to one month after stroke is analysed.

The most striking result emerging from this analysis is that the rehab group is significantly distinguishable from both the control and the robot group. To find differences between groups in the angle distribution, it is not sufficient to look at all events together (Fig. 3.5a), but instead it is necessary to split the results into event types (Fig. 3.5b).

The events of the rehab group display a greater smoothness compared to the control (p=0.025) and robot ($p=10^{-4}$) groups. The biggest difference can be observed for rehab versus robot group; it is significant not only for all events together ($p=10^{-4}$, Fig. 3.5c) but also for each event type separately (all $p< 0.01$, Fig. 3.5d). Note that, as for the angle, the smoothness of the rehab group appears to be consistent when distinguishing different event types, meaning force, non-force, active, passive, reward and non-reward pulling events display the same average smoothness value.

Among all the characteristics investigated, the marker that distinguishes most clearly between the rehab group, control ($p=10^{-4}$) and robot ($p=10^{-6}$) groups is duration. The events of the rehab group are shorter than for the

control (all $p< 0.01$) and robot (all $p< 0.001$) groups (Fig. 3.5e-f). Again, this statement applies to all events together (Fig. 3.5e) as well as to each event type individually (Fig. 3.5f). Also in this case, the duration of the rehab group appears to be consistent when looking at different event types.

In summary, the rehab group is significantly different from both control and robot groups. In particular, it is characterised by higher smoothness and shorter duration. Differences between the rehab and the other two groups can be observed not only for all events together, but also for specific event types. Especially, when looking at specific event types (force, non-force, active, passive, reward pull, non-reward pull) the three spatiotemporal propagation indicators are able to distinguish the rehab group from the control and robot groups.

3.3 Discussion

In this chapter an improved version of the recently proposed SPIKE-order analysis was used [122] to sequences of wide-field fluorescent calcium images from the dorsal cortex of awake and active mice. Three propagation indicators that characterise the duration, the angle of propagation and the smoothness of movement-evoked global events was defined. This new way of quantifying variations in the spatiotemporal propagation patterns during longitudinal motor training allowed the tracking of damage and functional recovery following stroke.

It was found that in healthy mice all three indicators of spatiotemporal propagation display a very high degree of consistency over time. For animals with acute stroke, the propagation patterns of the global events are altered. The most prominent consequence is a large increase in global event duration and a decrease in smoothness over the ipsilesional hemisphere. Two different rehabilitation therapies were also compared, motor training alone and motor training combined with pharmacological therapy. While both reverse the effects observed during the acute phase, the combined treatment, promoting a generalised recovery of the forelimb dexterity, leads to a new functional efficacy, different from pre-stroke conditions, with very fast and smooth propagation patterns.

In summary, the detailed spatiotemporal analysis of global activation patterns during longitudinal motor training provides a powerful non-invasive tool to quantify the success of different state-of-the-art rehabilitation paradigms.

The propagation-based biomarkers deliver new and unforeseen information about the brain mechanisms underlying motor recovery and this could pave the way towards a more targeted post-stroke therapy.

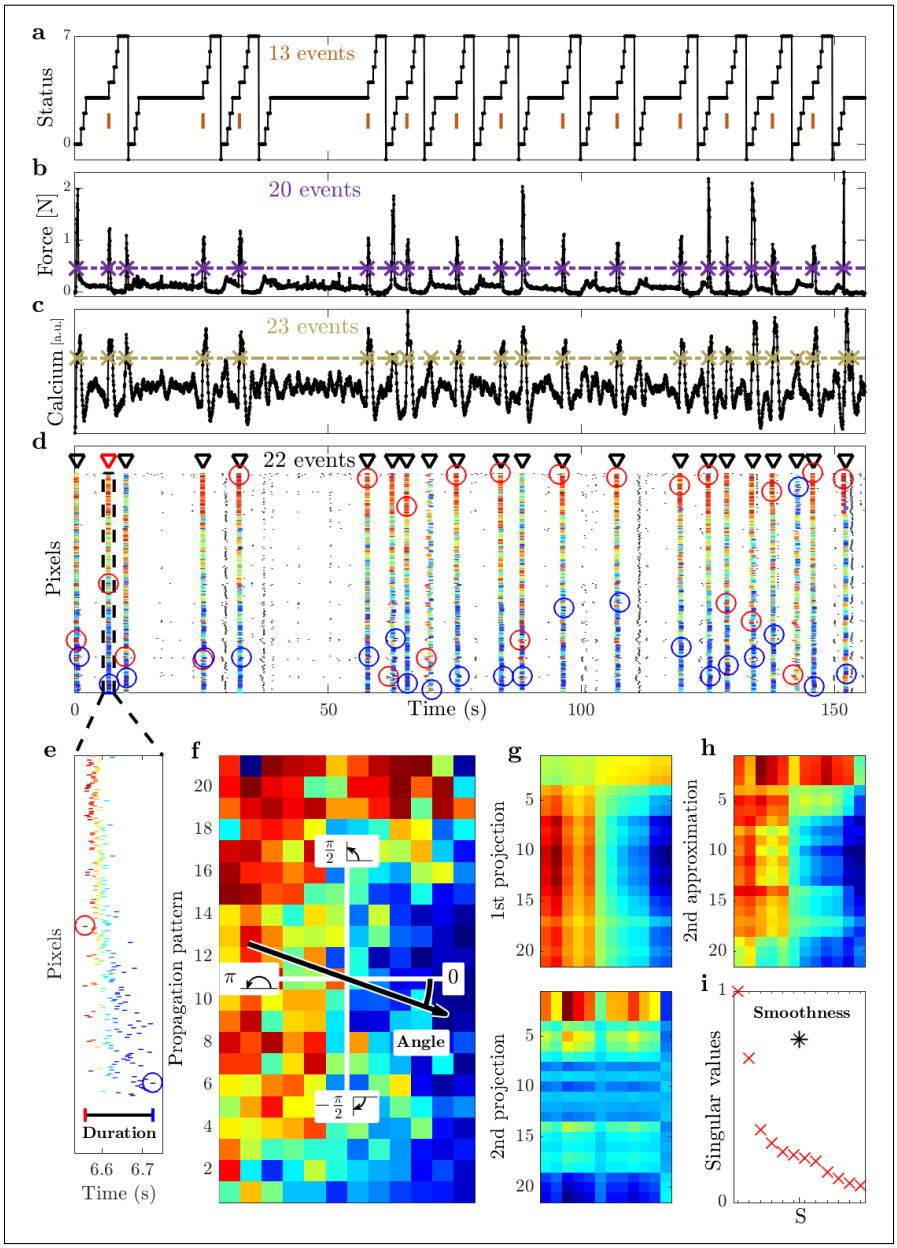

Figure 3.2: Event identification, propagation analysis, and definition of three propagation indicators: duration, angle, and smoothness.

Fig. 3.2 continued on next page

Fig. 3.2 continued
(a) Status of the robotic slide. The longer horizontal plateaus at status 3 correspond to the time interval during which the mouse is allowed to retract the slide. The orange bars refer to the time when the pull is completed and the mouse receives its reward. **(b)** Force applied by the mouse during the retraction movement. **(c)** Average calcium signal over all pixels. The purple and yellow dashed lines below refer to the threshold used to identify the force and global calcium events, respectively. **(d)** Raster plot obtained from the threshold crossings of individual pixels versus time. Triangle indicators show the global events identified during this session, and the red triangle with dashed box marks the event analyzed in the remaining panels below. The first (last) spike of each global event is marked by a red (blue) circle. Within each subplot (a)-(d) we state the number of the respective events/threshold crossings. **(e)** Zoom of this selected event. The **duration** is defined as the interval from the first to the last spike within the event. **(f)** The propagation matrix is obtained by projecting the relative order of these threshold crossings onto the 2D-recording plane. By means of singular value decomposition (SVD) we obtain the **angle** of the propagation, defined relative to the horizontal axis. **(g)** First and second approximations of the propagation matrix and **(h)** second-order approximation as their weighted sum (cumulative). **(i)** Singular values (red) vs. order of approximation. The **smoothness** (black asterisk) measures the quality of the approximation.

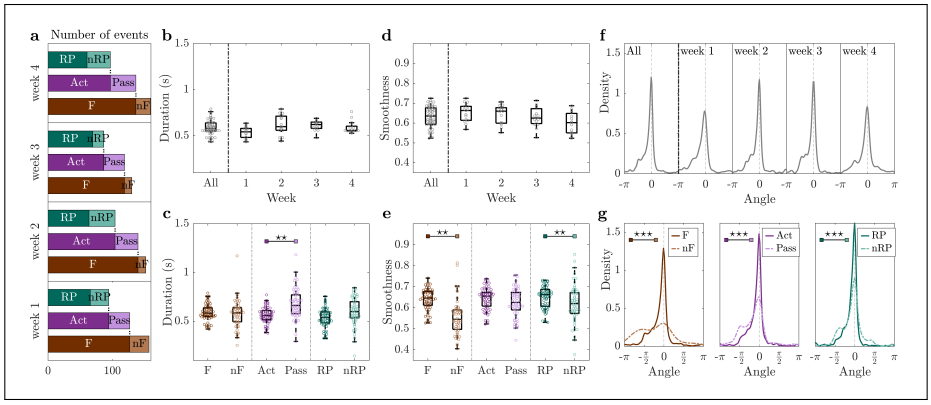

Figure 3.3: Cortical propagation features discriminate event types in healthy mice. **(a)** Mean number of events for all three mice per week, partitioned by type of event. **(f-g)** Narrowing down the type of event leads to more directed propagation patterns, while remaining unchanged over weeks. **(d-e)** Smoothness discriminates force (F) and non-force (nF) events, and is preserved over weeks. **(b-c)** Event duration is a marker for discriminating active (Act) and passive (Pass) events, as well as reward pulling (RP) and non-reward pulling (nRP) events. Angle and duration are weighted by smoothness. Markers in (b-e) refer to the average value per day. Within each box in (b-e), the central mark indicates the median, and the bottom and top edges of the box indicate the 25^{th} and 75^{th} percentiles, respectively. Control group n=3 mice.

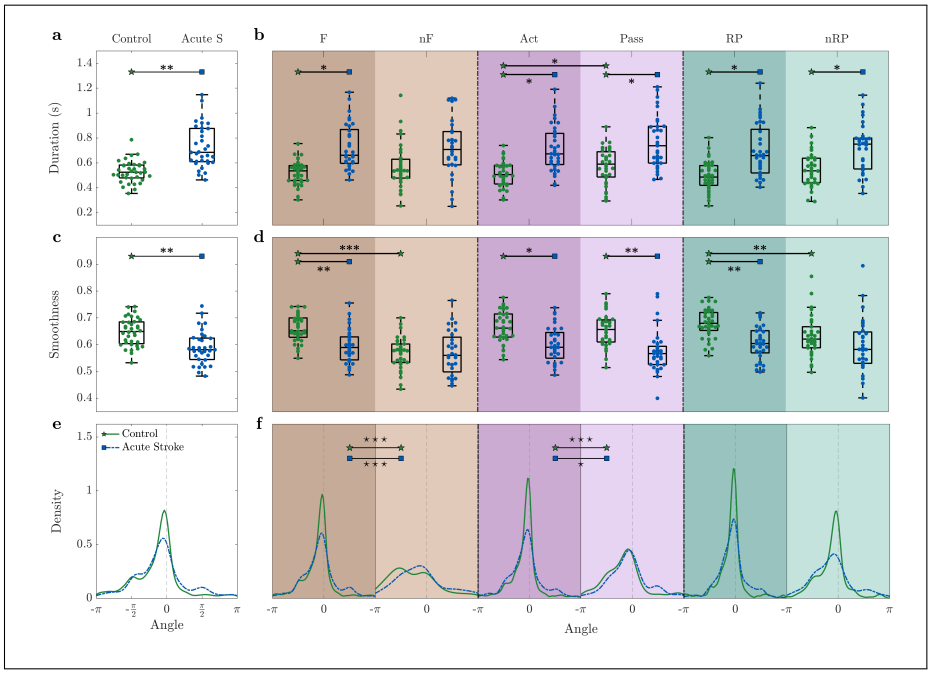

Figure 3.4: The acute phase (1 week after stroke) is characterised by an increase of the event duration. During the acute phase, **(a-b)** the event duration is increased, **(c-d)** smoothness is decreased, and **(e-f)** the direction of propagation is more spread. Markers in (a-d) refer to the average value per day. Within each box in (a-d), the central mark indicates the median, and the bottom and top edges of the box indicate the 25^{th} and 75^{th} percentiles, respectively.

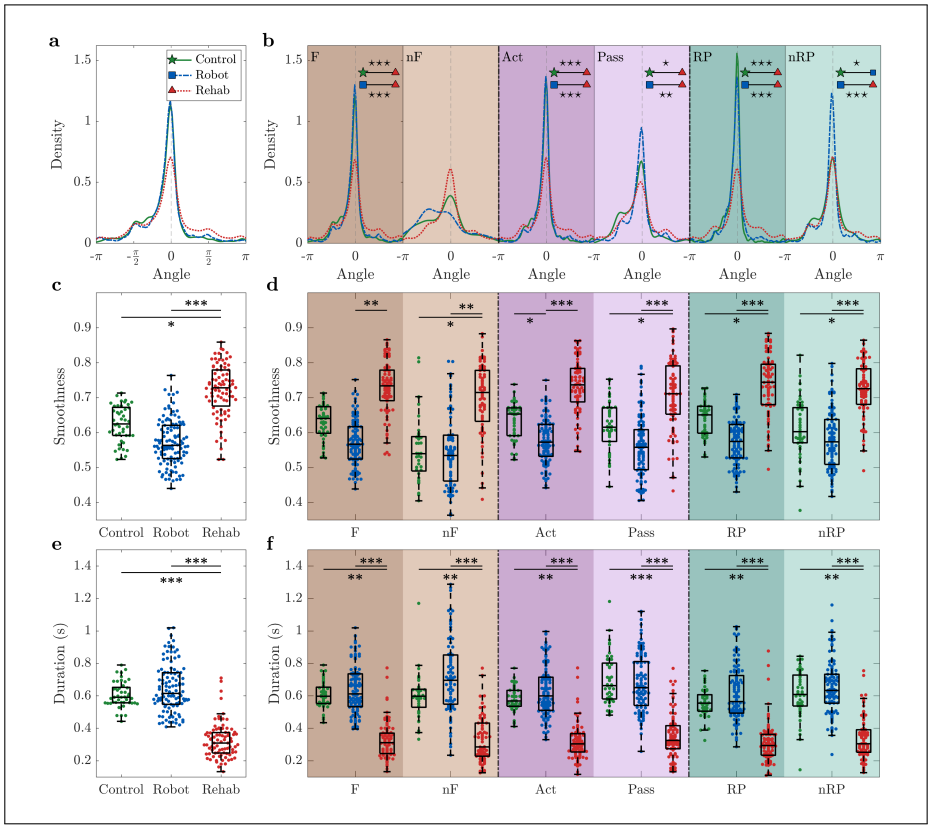

Figure 3.5: Rehab group is characterised by higher smoothness and shorter duration. **(a-b)** For the rehab group the distribution of the angles does not vary depending on the type of event. **(c-d)** For all types of event, the smoothness of the rehab group is higher than for the robot group. **(e-f)** For all types of event, rehab group events are the shortest. Angle and duration are weighted by smoothness. Markers in (c-f) refer to the average value per day. Within each box in (c-f), the central mark indicates the median, and the bottom and top edges of the box indicate the 25^{th} and 75^{th} percentiles, respectively. Control group n=3 mice, robot group n=8 mice, rehab group n=6 mice. "$\star$" refers to difference in variance and "*" refers to difference in mean.

Chapter 4

Inferring network structure and local dynamics from neuronal patterns with quenched disorder

In Chapter 2 we have developed an inverse framework for reconstructing *a priori* unknown statistical features about the network topology in a synthetic context from limited observations of the collective dynamics. This analysis was performed on reaction-random walk models evolving on an undirected network support. Furthermore, it was the nonlinearity introduced by the local reactions and the tuning of the equilibrium solutions of the system that allowed enough data points to be sampled for the successful application of the inversion procedure. Here we will generalize the framework to a nonlinear Leaky Integrate and Fire (LIF) neuronal model evolving on a directed network support in order to apply the inversion procedure to the neuroscience dataset showcased in the last chapter while making use of a more dynamic sampling of the mean-field variable. In the previous chapter, we introduced a neural activity dataset, wide-field calcium fluorescence recordings of the mice undergoing training and rehabilitation after an induced stroke, and presented an overview of a spatiotemporal analysis of the global spiking event propagation patterns that track the recovery of an induced stroke through biomarkers. In this chapter we build upon the network reconstruction technique introduced in Chapter 2 and present a different analysis of the previously studied dataset that puts the emphasis on the structure of the intricate network that connects the fundamental units, the neurons, and

their inherent dynamics. To this end, we use an extended version of the LIF model with synaptic plasticity and added heterogeneity in associated currents to reconstruct both the in-degree distribution and the distribution of currents. This is first validated *in silico* following which we adapt the framework for the wide-field calcium imaging data set. We use the reconstructed information as a means to track the changes as the animals progress along their paths of recovery after stroke.

Inferring network characteristics from direct measurements of neuronal activity (spiking events), constitutes a challenging task. This yielded a large plethora of different methodological approaches [130; 131; 132; 133; 134; 135]. Popular techniques, aimed at recovering quantitative information on existing inter-nodes connections, rely for instance on statistical mechanics concepts, as e.g. maximum entropy principles [85; 86]. Network topology is one out of many possible sources of heterogeneity in the brain. Neurons may in fact also exhibit different intrinsic dynamics, an additional ingredient which can significantly impact the functioning of the brain [136]. Neuronal excitability (i.e. neurons' ability to respond to external inputs) is finely orchestrated in the brain through inhibitory/excitatory balance [137; 138; 139; 140]. Moreover, dysregulation of neurons' effective excitability (e.g. through excitation/inhibition unbalance) is often cause of pathologies, for example epilepsy [123; 141; 142]. Stroke is instead strongly associated with alteration in excitatory/inhibitory balance whose recovery can be boosted by rehabilitation [109; 143]. These factors are therefore crucial to understand the onset and the evolution of pathological states. Motivated by this, we here propose and successfully test against both synthetic and real data, an inverse protocol scheme: this is targeted to quantifying from global activity measurements [1] the neurons' inherent excitability, while inferring the, *a priori* unknown, distribution of network connectivities. The individual degree of excitability is here associated with a random variable, which does not evolve with time. It is hence frozen to a constant value, or quenched, in the jargon of statistical physics.

To this end we consider an extended model of Leaky-Integrate and Fire (LIF) neurons, with short-term plasticity. The neurons are coupled to a directed network and display a degree of heterogeneity in the associated current, which sets the effective excitability, and thus the firing regime, of

[1] The term global is used here to refer to the collective activity as obtained by averaging the recorded signals over a region of interest (as opposed to the signal associated to individual neurons).

the neuron. The aim of the method is to recover the distribution of the (in-degree) connectivity, in the following labelled k, which characterizes the embedding network, as well as the distribution of the assigned currents, denoted by a.

Our approach to the inverse problem presented in this chapter too builds on the Heterogenous Mean-Field (HMF) approximation [20; 102; 144; 145]. The key idea is to rewrite the dynamics of the system by organizing the neurons in different classes, each associated with distinct values of the current a and of the connectivity k. The HMF reduction scheme allows us to create a mesh in the space of the variables a and k, in such a way that the contribution of all possible neurons can be adequately represented. The inverse scheme aims at determining the sought density distributions $P(a)$ and $P(k)$. These latter are the solutions of a self-consistent iterative equation which identifies the classes of neurons needed to confidently reproduce the global activity field, supplied as an input to the algorithm. The HMF approximation has been previously employed in [87; 88; 89; 146] to recover the information on the hidden network topology, from global and local, synthetically generated, data. Starting from these premises, we here take a decisive leap forward by proving that a non-trivial generalization of the method can be effectively invoked to quantify, in addition, the amount of dynamical heterogeneity that characterizes the examined process. As we shall argue in the following, this latter component exerts a role of paramount importance in driving non-periodic, seemingly irregular patterns of activity, like those displayed in real measurements.

The first part of this chapter, Sections 4.1 to 4.3, introduce the model and the inverse framework. This is followed by the results of the analysis, in Section 4.4, which are manyfold:

- First, we will introduce the inverse method and test its efficacy against synthetic data. These are generated by assuming a random network to provide the structural skeleton of the model, while at the same time imposing a single- or multi-peaked profile for the distribution of currents. The method allows to accurately estimate the two distributions, while managing to interpolate almost exactly the time series of the collected global field.

- Then, we build a bridge from measurements to theory, by arguing that the raster plots for the spiking activity of neurons over time can provide the ideal input for the reconstruction method to work.

- Finally, we apply the proposed technique to experimental data, in this case, longitudinal wide-field fluorescence microscopy data of cortical functionality in groups of awake mice. To mimic an ischemic condition, a photothrombotic stroke is induced in the primary motor cortex. Functional recovery is promoted, via motor training on a robotic platform. The global activity fields as obtained from the experiments can be nicely interpolated by a LIF model which accommodates for quenched heterogeneity in the currents. Altered distributions in neuron excitability are detected during the acute phase, i.e. immediately after stroke. In particular, the neurons in the region adjacent to the stroke manifest a degree of enhanced excitability, in agreement with earlier experimental observation [147; 148; 149]. Conversely, rehabilitation recovered a distribution more similar to pre-stroke conditions.

Taken all together, the results presented in this chapter suggest that the proposed method could serve as a useful tool to follow the recovery process from a stroke.

4.1 The model

We consider a network of N nodes, labelled with the progressive discrete index i. Each node identifies a LIF neuron. Neurons have equal synapses and interact via the synaptic currents that are regulated by short-term plasticity. This model was proved capable of reproducing a large variety of dynamical regimes, from a-synchronous to quasi-synchronous regimes, encompassing bursting and chaotic behaviors [87; 103; 150]. Each neuron is associated a dynamical state vector $\mathbf{w}_i(t) = (v_i(t), x_i(t), y_i(t), z_i(t))$, where v_i stands for the rescaled membrane potential and x_i, y_i and z_i denote the fractions of neurotransmitters in the available, active and inactive states, respectively. This implies that, at any time t

$$x_i(t) + y_i(t) + z_i(t) = 1. \tag{4.1}$$

According to [61; 150; 151], when a fraction u of neurotransmitters in the available state is activated, the dynamics of the neural network can be described by the following equations

$$\dot{v}_i(t) = a_i - v_i(t) + \frac{g}{N} \sum_{j \neq i} A_{ij}\, y_j(t) \tag{4.2a}$$

$$\dot{y}_i(t) = -\frac{y_i(t)}{\tau_{in}} + ux_i(t)S_i(t) \tag{4.2b}$$

$$\dot{z}_i(t) = \frac{y_i(t)}{\tau_{in}} - \frac{z_i(t)}{\tau_r} \tag{4.2c}$$

where a_i represents the external input current of the i-th neuron, S_i stands for the spike train produced by neuron i, g is the coupling strength; A_{ij} are the entries of the adjacency matrix $\mathbf{A}$ that specifies the structure of the underlying network; τ_{in} and τ_r are suitable time constants. In the following, we will provide a detail explanation of the quantities involved in the formulation of the dynamical model.

As mentioned above, the parameter a_i is an important ingredient of the model, as it regulates the endogenous functioning of the corresponding neurons, in the uncoupled limit. With reference to the adopted rescaled variables setting, the critical value $a_i = 1$ identifies a bifurcation point, which separates between quiescent and active (spiking) dynamical regimes. Notwithstanding the focus of the model that is here solely placed on excitatory neurons (i.e. $g > 0$), a can be conceptualized as an effective parameter which controls the net current received by the neuron, forcing it to input ($a > 1$) or fluctuation ($a < 1$) dominated regimes. This forthcoming analysis will also be generalized later in Chapter 5 to the interesting setting where populations of excitatory and inhibitory neurons are simultaneously present, at the price of a non-trivial complexification of the procedures involved.

In Eq. (4.2b), $S_i(t)$ represents the spike train produced by neuron i, in formulae

$$S_i(t) = \sum_n \delta(t - t_i(n)) \tag{4.3}$$

where $t_i(n)$ is the time when neuron i fires its n-th spike. Notice that, in this simplified model of neural activity, a spike is assimilated to a Dirac δ-distribution. Such a spike is generated by neuron i whenever its membrane potential $v_i(t)$ crosses the threshold value $v_{th} = 1$. Immediately afterwards v_i is reset to zero and the spike is transmitted to its efferent neurons. The synaptic dynamics regulated by the short-term plasticity which mediates the transmission of the spike-train function, follows the scheme implemented in Eqs. (4.2b) and (4.2c). When neuron i emits a spike, it releases a fraction of neurotransmitters $ux_i(t)$ and the fraction of active resources $y_i(t)$ gets consequently increased. In between consecutive spikes of neuron i, the use

of active resources yields an exponential decrease, on a time scale τ_{in}, of $y_i(t)$, while the fraction of inactive resources $z_i(t)$ gets increased by the same amount. At the same time, while $z_i(t)$ decreases, over a time scale τ_r, the fraction of available resources is eventually reintegrated. In fact, by combining Eqs. (4.2b), (4.2c) and (4.1) one readily obtains

$$\dot{x}_i(t) = \frac{z_i(t)}{\tau_r} - u x_i(t) S_i(t). \tag{4.4}$$

Spikes from the afferent neurons j are received by neuron i through the sudden increase of their active resources $y_j(t)$ and affect the dynamics of its membrane potential via the coupling term (tuned by the parameter g) which sits on the right hand side of Eq. (4.2a). The existing connections between pairs of neurons are specified by the binary adjacency matrix $\mathbf{A}$. The entries A_{ij} are set to one if neuron j fires to neuron i and zero, otherwise. In this simplified model, all the parameters appearing in the above equations (except for the intensity parameter a_i) are independent of the neuron indices and each neuron is connected to a macroscopic number of pre-synaptic neurons: this is the reason why the interaction coupling g is normalized by the factor N. We further consider *dense networks*, where each neuron is connected to $\mathcal{O}(N)$ pre-synaptic neurons [2]. As it is common practice, the timescales in the above equations are attributed by the phenomenological values in adimensional units, $\tau_{in} = 0.2$, $\tau_r = 133\tau_{in}$, $g = 30$ and $u = 0.5$, see [150; 152].

4.2 The heterogeneous mean field ansatz.

A simple analogue of the model described in the previous Section, with homogeneous currents, $a_i = a > 1$, was studied in [87], and successfully employed to reconstruct in silico the network structure (more precisely, the distribution function from which the random connectivity network was sampled) from global signal of, synthetically generated, synaptic activity. To accomplish this step, the original model is reformulated in terms of a Heterogeneous Mean Field (HMF) approximation: the original single-neuron variables are hence replaced by families of neurons with equal average input

[2] This choice is inspired to the the mean-field derivation of the HMF technique, the standard mean-field limit being recovered in a fully connected network, where $A_{ij} = 1$ for any pair i, j, i.e. where the number of pre-synaptic neurons is $N - 1$ for all neurons. We stress however to that the HMF works out also for non-dense networks.

connectivity. In practice, when dealing with an extended population of neurons, connected via a large number of synapses, one can safely enough omit unimportant *microscopic* details of the network structure and just focus on average, i.e. mean-field-like, observables. The goal of our analysis is to take the method to a different conceptual level, by allowing for a quenched disorder in the current input. Quenched disorder turns out to be a crucial factor for capturing the variability of the amplitude of the global signal of synaptic activity, which appears to be unnaturally regular in the homogeneous case, i.e. when all $a_i = a$, as in [87]. *A posteriori* we can argue that quenched disorder amounts to a heuristic recipe for surrogating the effects of inhibitory neurons, in a simplified framework where neurons are assumed of the excitatory type. To work out the HMF approximation for the considered model we define the the input field Y_i to each neuron as $Y_i = \frac{1}{N}\sum_j A_{ij} y_j$. This latter quantity can be written in terms of the average input field per neuron as $Y_i = \frac{k_i}{N}\left[\frac{1}{k_i}\sum_{j\in I(i)} y_j\right]$ where $I(i)$ represents the set of k_i pre-synaptic neurons of neuron i. For large enough networks [3], the average input field for neuron i can thus be approximated as $\frac{1}{k_i}\sum_{j\in I(i)} y_j \approx \frac{1}{N}\sum_j y_j$. Since $Y(t) = \frac{1}{N}\sum_j y_j$ and that $\tilde{k} = \frac{k_i}{N}$, we can write $Y_i = \tilde{k} Y(t)$ where $\tilde{k} \in (0, 1]$. The key idea is to assume that all neurons with the identical rescaled degree $\tilde{k}$ and current a share the same dynamical equations, a condition which readily translates into the self-consistent dynamical relation

$$Y(t) = \int_0^1 \int_{a_{min}}^{a_{max}} P(\tilde{k}) P(a) y_{\tilde{k},a} da dk \tag{4.5}$$

where $a \in (a_{min}, a_{max})$ and

$$\dot{v}_{\tilde{k},a} = a - v_{\tilde{k},a}(t) + g\tilde{k} Y(t) \tag{4.6}$$

$$\dot{y}_{\tilde{k},a} = -\frac{y_{\tilde{k},a}(t)}{\tau_{in}} + u\left(1 - y_{\tilde{k},a}(t) - z_{\tilde{k},a}(t)\right) S_{\tilde{k},a}(t) \tag{4.7}$$

$$\dot{z}_{\tilde{k},a} = \frac{y_{\tilde{k},a}(t)}{\tau_{in}} - \frac{z_{\tilde{k},a}}{\tau_r} \tag{4.8}$$

[3] For the mean-field approximation to be valid, the average in-degree of the neurons should be large. This condition is guaranteed in the limit of $N \to \infty$ in massive networks where the average connectivity scales with the size N. In [89] it was shown that the HMF approximation works also for sparse networks, as far as the average connectivity is sufficiently large.

The above set of equations provides a great numerical advantage over their original analogues, especially when large systems are to be considered. Each class of neurons, as identified by the combined topological/dynamical pair $(\tilde{k}, a)$, is in fact solely driven by the mean-field $Y(t)$. It is hence possible to update in time the state of the system in the reduced space of the reference classes without keeping explicit track of all binary interactions, as encoded in the network adjacency matrix. Further, the basic features of the dynamics of the examined system can be effectively reproduced (modulo finite–size corrections) by exploiting a suitable discrete sampling of both $P(\tilde{k})$ and $P(a)$ (see below). The validity of the HMF ansatz is challenged via direct simulations of the original model. Results reported in annexed Supplementary Information (SI) testify on the adequacy of the proposed approximation.

4.3 The inversion method

The input to the inverse problem is represented by the global field $Y(t)$, which is therefore assumed known. We shall return to the actual generation of the time series $Y(t)$, when discussing the application of the proposed method to both synthetic and real data. In the following, we will set up the general scheme for recovering the unknown distributions $P(a)$ and $P(\tilde{k})$, by interpolating the available field $Y(t)$, under the simplified HMF descriptive framework.

First of all, and without any loss of generality, we select a suitable interval $[a_{min}, a_{max}]$, which contains the bifurcation threshold $a = 1$ and provides the support for the function $P(a)$ that we aim at recovering. The choice of the interval width is completely arbitrary, provided the interval is large enough to capture the true underlying distribution. This does however impact the ensuing analysis in term of associated computational cost: the larger the interval, the more demanding the numerical charge. We then proceed by discretizing the interval in q equally spaced bins, each of extension $\Delta a = (a_{max} - a_{min})/q$. The discrete counterpart of the continuous distribution $P(a)$ is therefore traced back to a vector made of q scalar unknown components, namely $\mathbf{P_a} = (P(a_1) \cdots P(a_q))$.

We proceed similarly to discretize the continuous function $P(\tilde{k})$. The unitary segment is binned in r equally spaced intervals, each of size $\Delta\tilde{k} = 1/r$, to eventually obtain the r-dimensional vector $\mathbf{P_{\tilde{k}}} = (P(\tilde{k}_1) \cdots P(\tilde{k}_r))$, which constitutes the discrete version of the degree distribution that we seek

at reconstructing.

The inversion procedure runs as follows. The HMF model made of Eqs. (4.6),(4.7) and (4.8) is initialized, with the variables $(v_{\tilde{k},a}, y_{\tilde{k},a}, z_{\tilde{k},a})$ being randomly drawn from a uniform distribution, which is constructed so as to respect the obvious constraints $v_{\tilde{k},a} < 1$ and $y_{\tilde{k},a} + z_{\tilde{k},a} < 1$. The governing equations, forced by the external field $Y(t)$, are integrated forward and the variables $y_{\tilde{k},a}$ stored, for each choice of the pair $(\tilde{k}, a)$ and for any sampling time. The process is repeated for M independent realizations of the initial conditions and the average fraction of neurotransmitters in the active state, for classes $(\tilde{k}, a)$ computed at any time of observation t_j, $j = 1, ..., n$, namely $\langle y_{\tilde{k},a}(t_j)\rangle = 1/M \sum_{i=1}^{M} \left(y_{\tilde{k},a}(t_j)\right)_i$, where the index i identifies distinct trajectories. Neurons are split into two classes, respectively locked (to the driving signal) and unlocked ones. The averaging helps to approximate the contribution from the many individual neurons, all behaving slightly differently, while belonging to the same unlocked class. This issue is further discussed in [87].

Our aim is to determine the (normalized) vectors $\mathbf{P_a}$ and $\mathbf{P_{\tilde{k}}}$ which match the self-consistent condition $Y(t_j) = \sum_{l=1}^{q} \sum_{m=1}^{r} P_{a_l} P_{\tilde{k}_m} \langle y_{\tilde{k},a}(t_j)\rangle$, for any time t_j. To this end, we start with an initial guess for the distribution to be eventually recovered (typically a uniform distribution over the respective interval of pertinence) and iterate a recursive scheme which is organized into two nested cycles.

First, the assigned components of $\mathbf{P_a}$ are used to compute the reduced $y_{\tilde{k}}(t_j) = \sum_{l=1}^{q} P_{a_l} \langle y_{\tilde{k},a}(t_j)\rangle$ entries (notice that the angle brackets are deliberately dropped on the left hand side to lighten the notation). These entries can be organized into a linear problem which implements the above constrain, for a quenched distribution of currents:

$$\begin{bmatrix} 1/\triangle\tilde{k} \\ Y_1 \\ \vdots \\ Y_n \end{bmatrix} = \begin{bmatrix} 1 & \cdots & 1 \\ y_{\tilde{k}_1}(t_1) & \cdots & y_{\tilde{k}_r}(t_1) \\ \vdots & \ddots & \vdots \\ y_{\tilde{k}_1}(t_n) & \cdots & y_{\tilde{k}_r}(t_n) \end{bmatrix} \begin{bmatrix} P_{\tilde{k}_1} \\ \vdots \\ P_{\tilde{k}_r} \end{bmatrix} \tag{4.9}$$

where $(Y_1 \cdots Y_n)$ are the n values of the continuous field $Y(t)$ sampled at the observation times $(t_1, t_2....t_n)$. The first equation of the above linear system is added to enforce the normalization of the sought solution. By matrix inversion one can in principle obtain an estimate of $\mathbf{P_{\tilde{k}}}$, at fixed $\mathbf{P_a}$. In real applications, system (4.9) is solved in norm using dedicated optimization

tools, as the transfer $n \times r$ matrix is in general ill-conditioned. As a second step in the reconstruction process, we freeze $\mathbf{P}_{\tilde{\mathbf{k}}}$ to the solution obtained above and compute $y_a(t_j) = \sum_{m=1}^{r} P_{\tilde{k}_m} \langle y_{\tilde{k},a}(t_j) \rangle$ (again we dropped, for the ease of notation, the angle bracket). Then the following linear problem is found:

$$\begin{bmatrix} 1/\triangle a \\ Y_1 \\ \vdots \\ Y_n \end{bmatrix} = \begin{bmatrix} 1 & \cdots & 1 \\ y_{a_1}(t_1) & \cdots & y_{a_q}(t_1) \\ \vdots & \ddots & \vdots \\ y_{a_1}(t_n) & \cdots & y_{a_q}(t_n) \end{bmatrix} \begin{bmatrix} P(a_1) \\ \vdots \\ P(a_q) \end{bmatrix} \tag{4.10}$$

which can be readily solved via apt numerical methods so as to obtain an estimate of $\mathbf{P}_{\mathbf{a}}$, at fixed $\mathbf{P}_{\tilde{\mathbf{k}}}$. The above procedure is iterated recursively until a maximum number of allowed cycles is reached, or, alternatively, the stopping criterion is eventually met. More precisely, we monitor the error function (the root mean square difference of the input and reconstructed fields) against different iterations of the aforementioned procedure. For all examined settings, we observed a smooth convergence of the error function. The sought distributions are indeed found to attain their asymptotic solutions after a few (complete) iterations. Here, we assume the rather conservative value of 100 maximum iterations. At the end of the iterations, and for all inspected cases, the modulation in the error function between successive iterations is smaller than 0.01%. The proposed reconstruction algorithm is graphically illustrated in panel B of Fig. 4.1. In the following section, we will test the predictive adequacy of the method, challenging it against synthetically generated data. Then, we will turn to the analysis of longitudinal wide-field fluorescence microscopy data cortical functionality in mice.

4.4 Results

4.4.1 Testing against synthetic data

We shall hereafter proceed by testing the proposed reconstruction protocol against synthetic data. To this end, we begin by generating a random graph made of N nodes [4]. This in turn amounts to constructing the binary $N \times N$

[4]Here, we chose $N = 500$. On the one hand, this allows for the computation to be carried out on standard computer resources. On the other hand, networks of this size

adjacency matrix $\mathbf{A}$, which sets the links among pairs of adjacent nodes. The procedure is engineered so as to return a bell-shaped distribution of connectivities $P(\tilde{k})$. The standard deviation of the distribution is sufficiently small so that the tails of the distribution at the boundaries are by all practical purposes irrelevant. We then add quenched disorder in the input currents a_i. The assigned currents display a mono-modal probability distribution $P(a)$, but more complex scenarios can be considered (see SI, where a bimodal $P(a)$ is assumed to hold). In panels C and D of Fig. 4.1, the distributions $P(\tilde{k})$ and $P(a)$, as obtained via the recipe outlined above, are depicted in red (crosses). These are the exact distributions that we aim at eventually recovering by means of the proposed reconstruction algorithm. Note that the chosen $P(a)$ extends over a finite domain which includes the bifurcation value $a = 1$.

As a first step in the analysis we proceed by integrating forward equations (4.2a), (4.2c) and (4.2c), for our specific realization of the network architecture and accounting for the heterogeneous collection of current entries a_i. From the numerics, one can readily obtain the ensuing raster plot, displayed in panel A of Fig. 4.1: each black dot identifies a spiking event. Neurons are ranked with a progressive discrete index which runs from low to highly connected units. The smooth curve superposed in red stands for the recorded global field $Y(t)$. As an important remark, we notice that the field $Y(t)$ shows irregular oscillations, characterized by a significant modulation in their relative height, as well as a non-uniform distribution of the time interval between successive peaks. This is at variance with the case where the currents are set to an identical value (when i.e. the distribution $P(a)$ converges to a Dirac delta). In this latter case, in fact, the oscillations are periodic and the LIF model cannot be straightforwardly invoked to reproduce the complex heterogeneity of patterns, as displayed in the by brain of living entities. The time series $Y(t)$ is provided as an input to the reconstruction algorithm described above and schematically illustrated in panel B of Fig. 4.1. The reconstructed distributions $P(\tilde{k})$ and $P(a)$ are depicted in blue (circles) in panels C and D of Fig. 4.1 and adhere to their corresponding exact profiles. $P(\tilde{k})$ and $P(a)$ are initially assumed to be uniform in their domain of pertinence. In order to recover the sought distributions,

yield a statistically sound representation of the sought distribution. Remark also that the experimental data analyzed in the following extend over a region of 20×20 pixels. This in turn amounts to dealing with networks of $N = 400$ nodes, a size comparable to that assumed in the synthetic setting.

the algorithm seeks to iteratively interpolate the global field $Y(t)$. The reconstructed field obtained at the end of the procedure is represented in blue (circles) in panel E of Fig. 4.1: it is almost indistinguishable from the curve depicted in red, which refers to the recorded input function $Y(t)$. The quality of the fitting can be better appreciated by performing a zoom on just one peak of the collection (see inset of panel E). As a side remark, we recall that the reaction parameter of the LIF model are here set to the nominal values, as assumed in the forward simulations. Panel F of Fig. 4.1 shows the reconstructed $P(a)$, in blue (circles), as obtained from a numerical test which assumes an all–to–all network of inter-neurons corrections. As we shall elaborate in the following, this will prove a setting of interest for properly addressing the analysis of the experimental time series. The exact $P(a)$ is depicted in red and the quality of the reconstruction is remarkably good. In panel G of Fig. 4.1 the interpolated $Y(t)$ (blue, circles) is confronted with the original signal (red), as stored in direct simulations and the agreement is again excellent (see also the annexed zoom in panel H). In this case, the iterative scheme was set to minimize the distance between the original and the reconstructed $Y(t)$, just for values of the field above a given threshold (notice that the fitted entries, the blue circles, are depicted only for a sufficiently large activity amount). This operative choice is motivated by the need of challenging a protocol that would be suited when dealing with experimental data. The low signal component is in fact in general corrupted by shot noise and should be filtered out in the reconstruction scheme. Remark also that the reconstructed profiles are robust against modulating the initial guess for the distributions to be eventually recovered. Stated differently, the system converges (for the explored settings) to a unique global attractor.

Summing up, we have here successfully tested the method against synthetic data. We have in particular demonstrated that the proposed scheme is capable to self-consistently recover the distributions of degrees and currents (assumed independent and not mutually entangled), from a heterogeneous, seemingly irregular, field of neuronal activity. In the next section, we will apply the method to longitudinal wide-field fluorescence data of cortical functionality in mice.

4.4.2 Analysis of fluorescence data

The reconstruction technique developed above will be here employed to quantitatively analyze the wide-field fluorescence microscopy data of cortical func-

tionality collected from transgenic mice expressing a functional indicator in excitatory neurons. The resting state and motor-evoked cortical activation was recorded before, acutely after stroke and following rehabilitative training. For a technical account of the experimental setup, we refer to the annexed Method. Starting from the detrended calcium fluorescence images (see panel C of Fig. 4.2), for each pixel of the ensemble which defines the region of interest, we construct a raster plot as depicted in panel C of Fig. 4.2. To this end, we set a proper threshold and register, for each pixel, the time of exact crossing. The selected events are represented as black dots in panel C of Fig. 4.2 and provide direct evidence for the level of neuronal activity within the associated pixel. It is worth emphasizing that each pixel returns a signal which is the convoluted sum of the fluorescence signal emitted by lots of neurons laying both on the superficial and deep layers of the corresponding brain region. For what concerns the analysis that follows, we shall consider each pixel as representing one individual macroscopic neuron and assume that the interplay between coarse-grained units is ruled by a LIF model of the type analyzed above. The distribution of degrees and currents that we shall hereafter recover should be hence conceptualized with reference to the imposed level of spatial abstraction. The raster plot, as obtained from the experimental data, can be straightforwardly employed to compute the global field $Y(t)$, the input of the reconstruction algorithm discussed above. More specifically, the spike train information is a proxy for the function $S_i(t)$, which in spirit of the self-consistent formulation of the LIF model, comes from the dynamics of the membrane potential v_i. In this case, we take advantage of the experimentally computed $S_i(t)$ (i running on the pixels that define the region of interest) to evolve the paired Eqs. (4.2b) and (4.2c). We hence obtain the explicit evolution for the variables y_i, which can be combined so as to obtain the collective field $Y(t)$ (see schematic picture of panel C in Fig. 4.2). Notice that the reaction parameters which enter the definition of the above equations can be set to the nominal (although experimentally motivated) values mentioned above. These latter parameters will be also assumed when running the reconstruction scheme. In practical terms, Eqs. (4.2b) and (4.2c), complemented with the experimental input which materializes in the raster plot and, hence, in the associated function $S_i(t)$, act as a veritable filter which transforms fluorescence data into an ideal input for the inverse procedure to run.

The analysis of the experimental data can be broken up into two distinct

parts. First, we shall turn to analyzing the data collected under resting state. Then we will consider the fluorescent signal recorded when the mice are motor training. In both cases, the raster plots are computed for each mouse and for different days of measurements. The reconstruction algorithm is then run according to the prescription detailed above so as to simultaneously recover the density distributions $P(\tilde{k})$ and $P(a)$ [5]. The results of this analysis are annexed as Supplementary Information: the $P(\tilde{k})$ profiles are consistently biased towards the rightmost edge $\tilde{k} = k/N \to 1$, implying that the underlying network is densely connected. This observation is indeed in line with the computed raster plots: the firings of the fictitious neurons associated to each lattice point of the selected domain are highly synchronized, possibly implying a packed web of paired connections. From a more fundamental point of view, and as recalled above, each pixel integrates the signal from an extended pool of actual neurons. This translates into a spatial resolution constraint which seems compatible with a local mean-field ansatz, for an accurate interpretation of the data which transcends the detailed knowledge of connections between pairs of neurons. Motivated by the results reported in the SI, we freeze therefore the network architecture to an all-to-all topology and set to reconstruct the *a priori* unknown $P(a)$, as the only source of heterogeneity under the HMF reductionist approach (see the setting analyzed in panels F,G,H of Fig. 4.1 for the benchmark application). The results of the analysis are displayed in Fig. 4.3 for both the resting and training settings. In both cases, and before the stroke, a peaked $P(a)$ profile is found with a modest fraction of (coarse-grained) neurons above the threshold of excitability. This is a reference working condition which appears quite reasonable under non-pathological operating conditions. The distribution of the intensities gets distorted immediately after the stroke, with the degree of excitability being significantly enhanced. The effect is reproducible across the population of mice, as it can be appreciated by looking at the region coloured in grey, which reflects the fluctuations due to individual variability. As time progresses during the rehabilitation training, the $P(a)$ converges back to its initial shape, an observation that can be made quantitative by monitoring

[5] Notice that the coupling strength g, is set to the nominal value adopted in the forward simulations of the model, see Fig. 4.1. This latter value is experimentally justified and at present cannot be self-consistently generated as a byproduct of the inverse scheme. Remark however that the parameter g, could be in principle absorbed in the definition of the rescaled degree $\tilde{k}$, a choice which materializes in a rigid shift in the recovered distribution of connectivities.

the skewness of the reconstructed distributions (red circles in panels A and C of Fig. 4.3). Hyperexcitability is indeed one of the physiological mechanisms which are known to be triggered by the sudden death of a population of neurons, as e.g. following a stroke [147; 148; 149] .

Accordingly, hyperexcitable tissue (from the high baseline fluorescence) have been observed in the penumbra in the acute phase on the same mouse model, which progressively returned to lower levels in spontaneously recovering stroke mice [109]. Further studies show in fact that neurons in the penumbra region, the area adjacent to that where the stroke takes place, exhibit an increased firing rate, as the consequence of a reduced efficacity of $GABA_A$ synapses. This observation is consistent with the results that we have here reported, and which follows a direct implementation of the proposed inverse scheme.

4.5 Discussion

Recovering functional and structural information from in vivo measurements of brain activity is a challenge of broad applied and fundamental relevance. Working in this framework we have here proposed, and successfully tested, a novel reconstruction method which aims at inferring information on the distributions of both firing rates and networks connectivity, from global activity measurements. The technique builds on a variant of the celebrated Leaky-Integrate and Fire (LIF) model, with short-term plasticity. The heterogeneity in the assigned currents results in a non-trivial, aperiodic, global field, which shares a striking similarity with the homologous quantity, accessed indirect experiments. The proposed inverse protocol deals with an effective reductionist approach, which implements an apt version of the Heterogeneous Mean Field (HMF) ansatz: the dynamics of the system is organized in different classes, each associated with distinct currents a and (rescaled) in-degree $\tilde{k}$. The reduced model is driven by the global field and the ensuing output used to fuel a self-consistent iterative scheme, which seeks at interpolating the field itself. When challenged against synthetic data, the inversion scheme is capable of returning an accurate description of the two distributions. Fluorescent microscopy data can be used to obtain experimentally tailored raster plots, which represent the ideal input for running the devised reconstruction machinery. The recovered distributions of intensities capture the phenomenon of neuronal hyperexcitability, which has been experimen-

tally found to interest the penumbra region, following a stroke event. This observation suggests that the proposed method could serve as a viable non-invasive strategy to track the recovery of pre-stroke brain functions. Notice that the observed modulation of in the distribution of a (before, during and after the stroke) can be eventually traced back to a change in the firing rates. The larger a (> 1), as it happens immediately after the stroke, the shortest the period of firing (or, equivalently, the faster the associated firing rate). As a general remark, it is worth stressing that, in many cases of interest, as in the present setting, data from neural experiments integrate global synaptic signals, which extend typically over relatively wide areas of the brain. The inverse procedure, based on the HMF recipe, moves from a coarse-grained representation of neuronal activity, from the scale of single neurons up to the pixels, which sets the image resolution of the recorded calcium waves. The analysis that we have carried out indicates that one can successfully frame the scrutinized dynamics in the context of simple microscopic models, so as to interpret, and eventually reproduce, relevant macroscopic patterns at the brain scale. This implies in turn that a *reductionist*, i.e. microscopically minimal, approach proves often adequate when aiming at describing the collective behaviour of a complex neural system. By decorating the microscopic level with additional modelling ingredients certainly allows one to grasp a full load of specific features, which prove undoubtedly relevant to characterize punctual aspects of the individual neuronal activity. On the other hand, key collective effects, emerging from the sea of interacting units, seems to be modestly affected by such fine details, which hence result in higher-order corrections to basic interpretative frameworks. For the case at hand, the imposed variability in the current a_i enforces an effective modulation of the neural activity, while avoiding exact synchrony of neurons in bursting events. *A posteriori* we can argue that quenched disorder in the firing rates amounts to a simple heuristic recipe for taking into account the effects of inhibitory neurons, which are responsible for tuning the excitatory neurons response. Stated differently, quenched disorder surrogates the effect of the inhibitory components in the brain.

4.6 Material and Methods

4.6.1 Experimental setup

The data used for the analysis presented in this chapter is a subset of that used in Chapter 3. For a detailed explanation of the experimental methods used for data collection, the preprocessing of the signals and the spike detection algorithm employed here, refer to Appendix A.1

4.6.2 MATLAB Implementation

We have made a simple implementation of the above-described reconstruction scheme available publicly for demonstrative purposes. It can be accessed through ($https://drive.google.com/drive/folders/1Em0CZRbDtkGm9Lg1d3sQEAVCQWnxm3h_?usp = sharing$)

4.7 Further tests

4.7.1 Testing the validity of the HMF approximations

The aim of this Section is to elaborate on the validity of the Hamiltonian Mean Field (HMF) approximation for the examined Leaky Integrate and Fire (LIF) model of interacting neurons. To this end, we start by computing the global field $Y(t)$, from direct integration of the LIF equations for a given realization of the embedding network and assigned values of the currents. The distributions $P(\tilde{k})$ and $P(a)$ are hence known a priori and can be used to generate $\bar{Y}(t)$, an approximate representation of the global field, as follows Eq. (5) in the main body of the paper, and upon integration of the HMF dynamics, see Eqs. (6-7). As it can be appreciated by visual inspection of panel A in Fig. 4.4 the field $\bar{Y}(t)$ obtained within the HMF scheme aligns almost perfectly with the signal which to be approximated. This in turn provides an a posteriori validation for the HMF working ansatz.

As a further check, we computed the individual Firing Rate (FR), i.e. the number of spikes per unit time, as a function of the $\tilde{k}$ and a. The (red) stars plotted in panels B and C of Fig. 4.4 refer to the FR as obtained by analyzing the time series obtained by integrating of the LIF model in the space of the nodes. The stars lay almost exactly on the manifold which is computed based on the HMF approximation. More precisely, for any given

pair $(\tilde{k}, a)$ we calculate the corresponding FR, under the HMF assumption, yielding the surface depicted with an appropriate colour code, this latter reflecting the estimated value of the FR indicator. Panels B and C offer different views of the same plot. The agreement between predicted and measured quantities points again to the validity of the HMF interpretative framework.

4.7.2 Reconstructing of a bi-modal $P(a)$

To further test the robustness of the proposed reconstruction protocol, we challenge the method against simulated data obtained for a bimodal $P(a)$ distribution. The results of the tests, which follow the conceptual scheme outlined in the main body of the paper, are displayed in Fig. 4.5 and confirm the predictive ability of the proposed method. The distributions, $P(\tilde{k})$ and $P(a)$, and the global field $Y(t)$ are nicely interpolated by their homologues reconstructed quantities.

4.7.3 Reconstructing $P(\tilde{k})$ and $P(a)$ from experimental data

Presented here are the results obtained when reconstructing simultaneously the distribution $P(\tilde{k})$ and $P(a)$ from experimental data, in this case, longitudinal wide-field fluorescence microscopy data of cortical functionality in groups of awake Thy1-GCaMP6f mice. For details that relate to the experiments and to the implemented reconstruction procedure, we refer to the main body of the paper. The results of the analysis are displayed in Fig. 4.6 and organized for different mice (rows, from A to E) and physiological conditions (before/stroke/after, grouped in different macro-columns). Blue traces (crosses) refer to individual days of experiments, within the explored window. The red lines (circles) stand for the average of the reconstructed distributions. Only signals obtained during the training sessions are sufficiently long to allow for the simultaneous reconstruction of $P(\tilde{k})$ and $P(a)$. In all cases, the recovered $P(\tilde{k})$ attain their global maximum at $\tilde{k} = 1$. This justifies our assumption of an all-to-all arrangement of the underlying network which in turn allows us to focus on the recovery of $P(a)$ (see main paper). However, the widening of the $P(a)$ immediately after the stroke, as discussed in the main paper, is also visible in the general setting when $P(\tilde{k})$ and $P(a)$ are recovered at the same time.

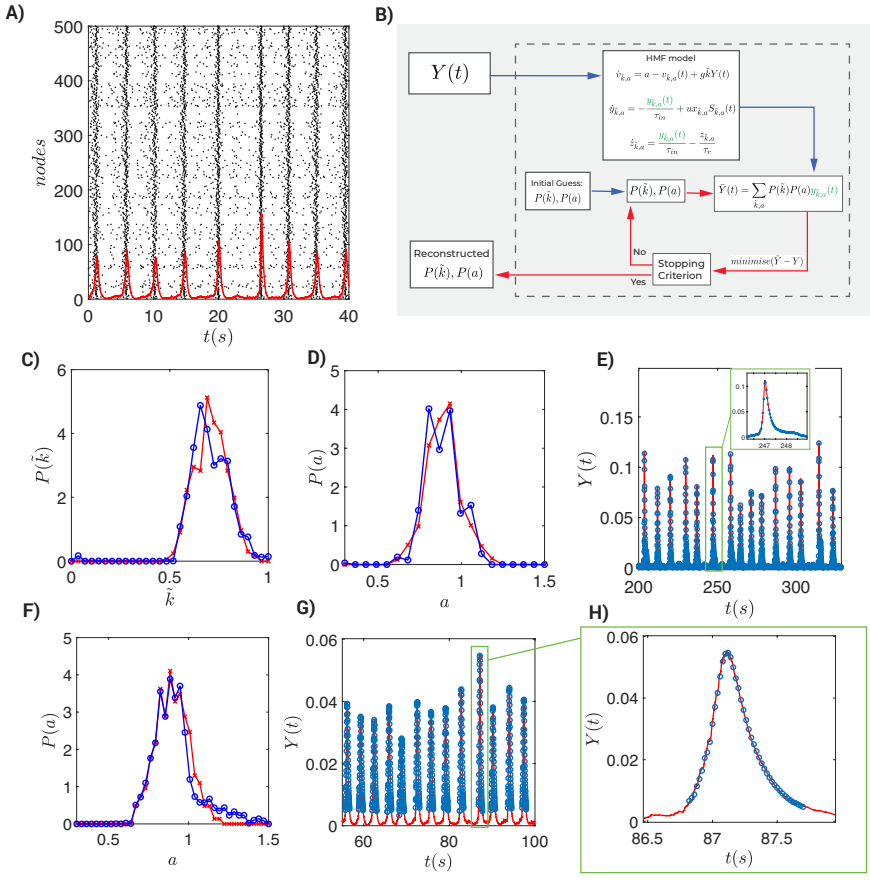

Figure 4.1: Panel A) shows the raster plot as obtained by simulating a network of $N = 500$ nodes. The distributions of in-degree and currents are drawn from Gaussian distributions with, respectively, $\langle k \rangle = 0.7$, $\sigma_{\tilde{k}} = 0.082$ and $\langle a \rangle = 0.9$, $\sigma_a = 0.1$). The global field $Y(t)$ is overlaid in red and multiplied by a scaling factor equal 2500 to help visualization. Panel B) shows a schematic outline of the reconstruction procedure. The blue arrows stand for the flow of inputs while red arrows refer to the iterative minimization procedure. Panels C), D) and E) display the outcome of the procedure, for the setting referenced to in the description of panel A). The true in-degree distribution is plotted in red while the recovered distribution is depicted in blue. In panel D) the true distribution of the external currents is displayed in red and the recovered distribution plotted in blue. E) The true global field ($Y(t)$) is shown with the solid red line and the reconstructed homologue represented with blue circles. The plot in the inset is a zoom-in of the peak in the green box. Panels F), G) and H) reports results of a similar test where now the network is fully connected and only $P(a)$ is reconstructed.

Fig. 4.1 continued on next page

Fig. 4.1 continued
— Here the algorithm seek at interpolating the driving field for value of $Y(t)$, above a minimal threshold. In panel F) the true distribution of the external currents ($\langle a \rangle = 0.9$, $\sigma_a = 0.1$) is displayed in red and the recovered distribution in blue. In panel G) the true global field is plotted with a solid red line and the blue circles refer to the reconstructed $Y(t)$. Finally, panel H) shows a zoomed-in plot of the peak in the green box in panel G). The plots of the distributions in panels C,D,E and F have been binned to have fewer points than the sampling of $\tilde{k}$ and a (r and q, respectively) that was used in the reconstruction.

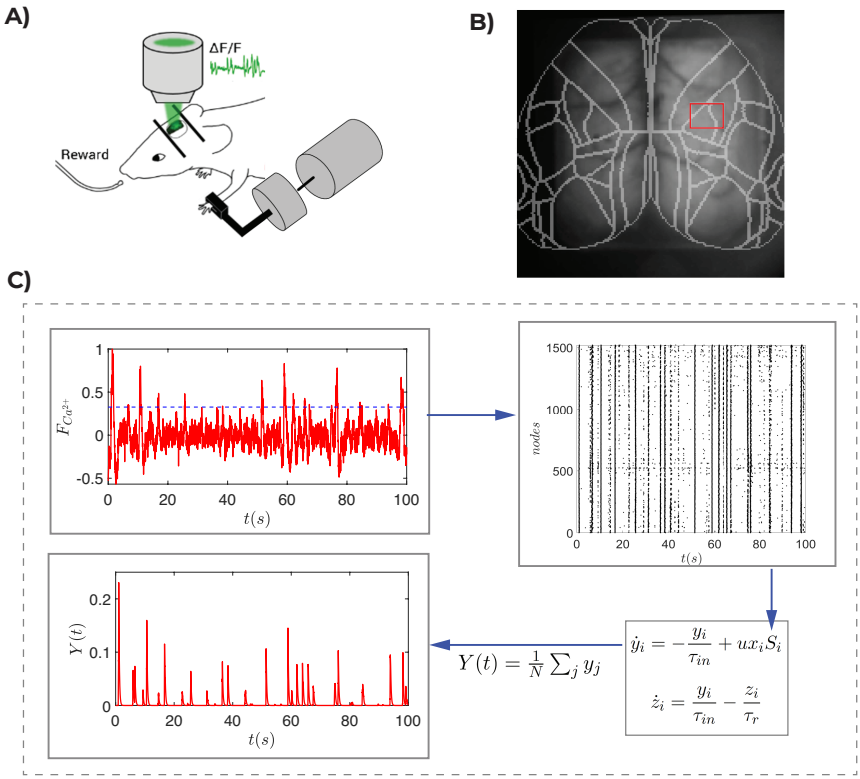

Figure 4.2: In panel A) a schematic layout of the experimental setup is shown. This includes the imaging equipment and the M-Platform used for rehabilitative training. Panel B) depicts (in red) the region of the brain from which the data for the analysis are eventually extracted. The region of interest is made of 20×20 pixels and encloses the portion of the brain affected by the stroke. The patterns in colour of grey displayed in the background refers to one typical snapshot of the calcium dynamics. The different domain in which the brain is segmented follow the Allen brain atlas. The first plot in panel C) shows the calcium fluorescence signal from one isolated pixel among those which fall in the region of interest, after detrending performed with a moving running average over a sliding window of three seconds. The to-right plot in panel C) is the raster plot of detected spikes using a threshold on each pixel. The threshold is here set to 1.8σ from the mean, where σ stands for the standard deviation of the recorded signal. Next, the spike train information is used to integrate the dynamics on each node, by means of Eqs. (4.2b) and (4.2c). The experimentally determined raster provides the needed function $S_i(t)$. Form the knowledge of y_i (on all pixels) one can compute the global field $Y(t)$ which is needed as an external driving input of the reconstruction scheme.

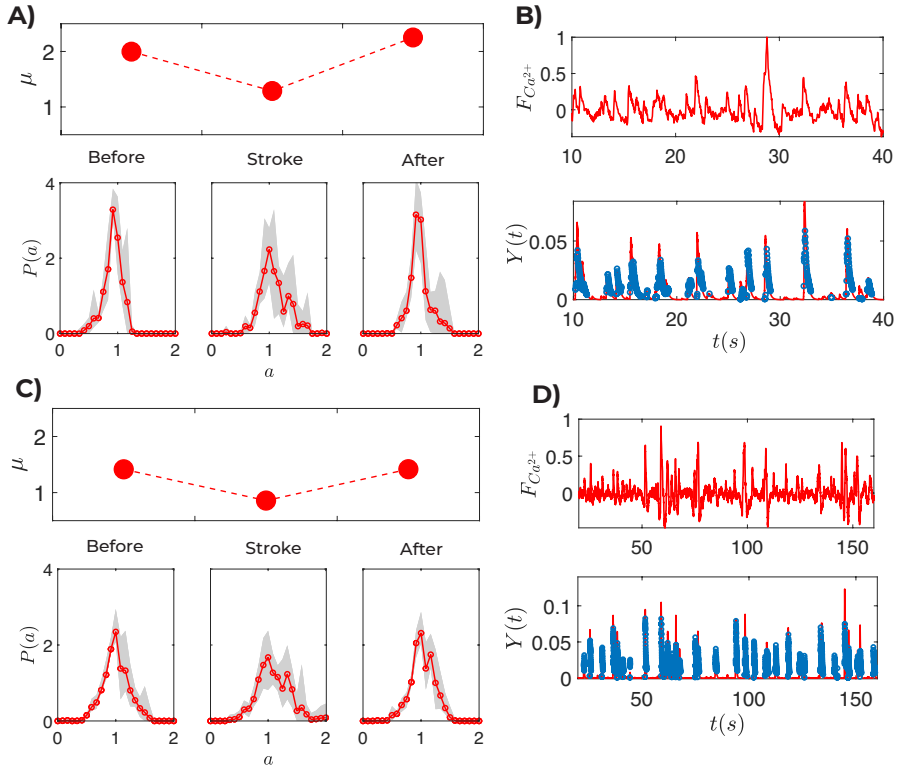

Figure 4.3: Panels A) and B) show results obtained from the resting data. In panel A) the distribution $P(a)$, averaged over 5 mice, is plotted for three successive windows of activity: before the stroke, immediately after stroke and three weeks after the stroke. In the reconstruction scheme a network with all–to–all connections in assumed (see SI for the combined reconstruction of $P(\tilde{k})$ and $P(a)$). Before the stroke, the distribution is narrow and peaked around one, the threshold of instability. The fraction of effective neurons which fall in the rightmost tail is relatively modest. Immediately after the stroke, the degree of excitability is generally enhanced. Then, as time passes, the distribution $P(a)$ regains the original shape, by lowering the population of excited units. The grey shadow sets the level of individual variability, as quantified by the maximum and minimum excursions of the average curves collected for each mouse. The skewness μ of $P(a)$, for each of the explored windows, is plotted with filled red circle in the top inset of panel A). The tendency to recovery the initial configuration is quantitatively substantiated. In panel B) the raw fluorescence data, the global field $Y(t)$ (in red) and the fitted solution (blue circles) are respectively displayed. Panel C) and D) report the analogous quantities obtained by analyzing the data recorded during the trial sessions (see Methods). Again the tendency of the system to enhance and then lower the level of excitability is clearly demonstrated.

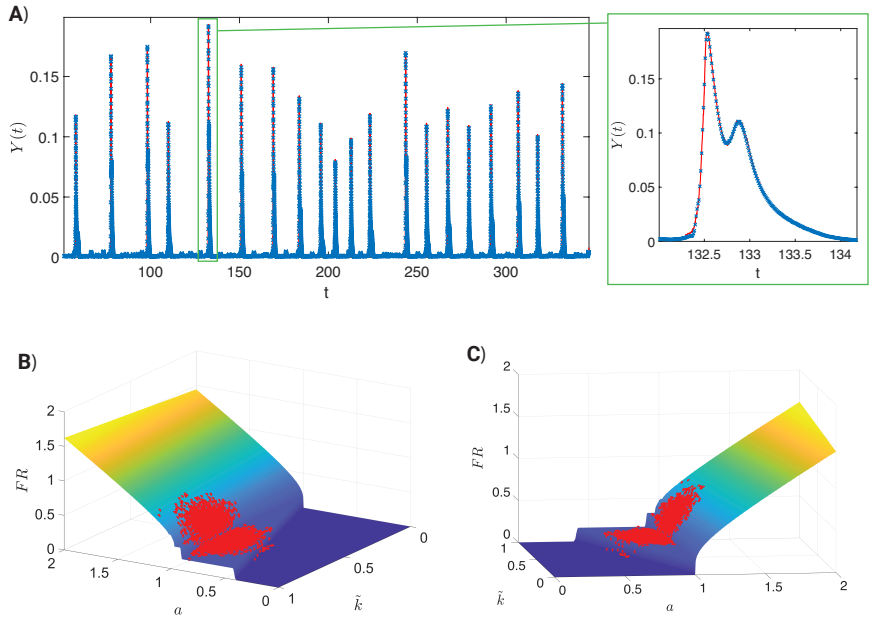

Figure 4.4: Panel A: the global field ($Y(t)$) as obtained from a direct integration of the LIF dynamics is shown with a solid red line. The reconstructed $\bar{Y}(t)$ signal, displayed with blue circles, is obtained from the true distributions $P(\tilde{k})$ and $P(a)$, by implementing the HMF reduction scheme. Here, $P(\tilde{k})$ is a unimodal bell shaped distribution with $\langle \tilde{k} \rangle = 0.7$, $\sigma_{\tilde{k}} = 0.082$. Similarly, $P(a)$ is characterized by $\langle a \rangle = 0.9$ and $\sigma_a = 0.1$. Panel B: the Firing Rate (FR) is plotted as a function of $\tilde{k}$ and a. The colored surface follows the HMF ansatz, while red crosses stem from direct integration of the original LIF model formulated in the space of the nodes. Panel C is a different view of the results displayed in panel B.

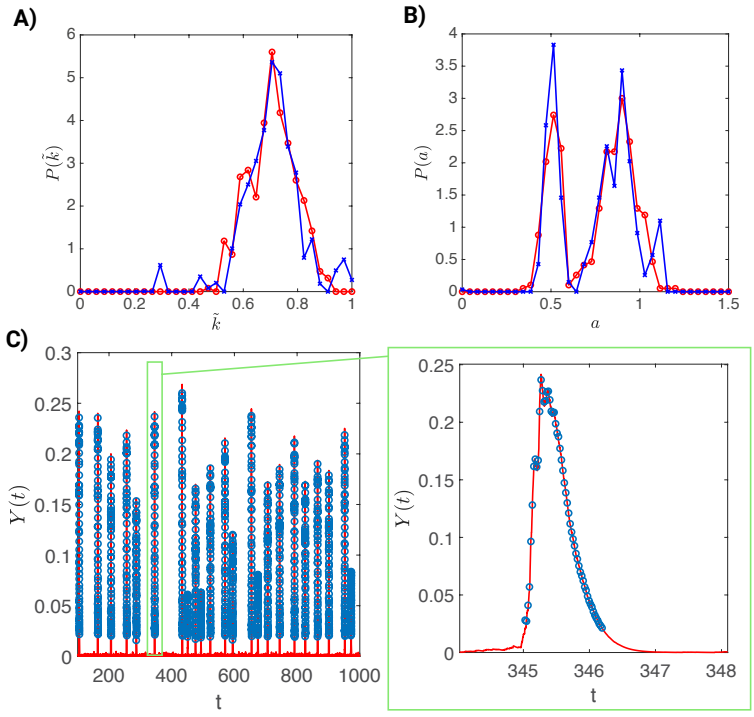

Figure 4.5: Panel A: the true in-degree distribution $P(\tilde{k})$ (here $\langle k \rangle = 0.7$, $\sigma_{\tilde{k}} = 0.082$) is shown in red (circles), while the recovered distribution is depicted in blue (crosses). Panel B: the true bi-modal distribution of the external currents $P(a)$ is shown in red (circle) and the recovered distribution in blue (crosses). Panel C: the true global field ($Y(t)$) is represented with a solid red line. Blue circles refer instead to the reconstructed signal $\bar{Y}(t)$.

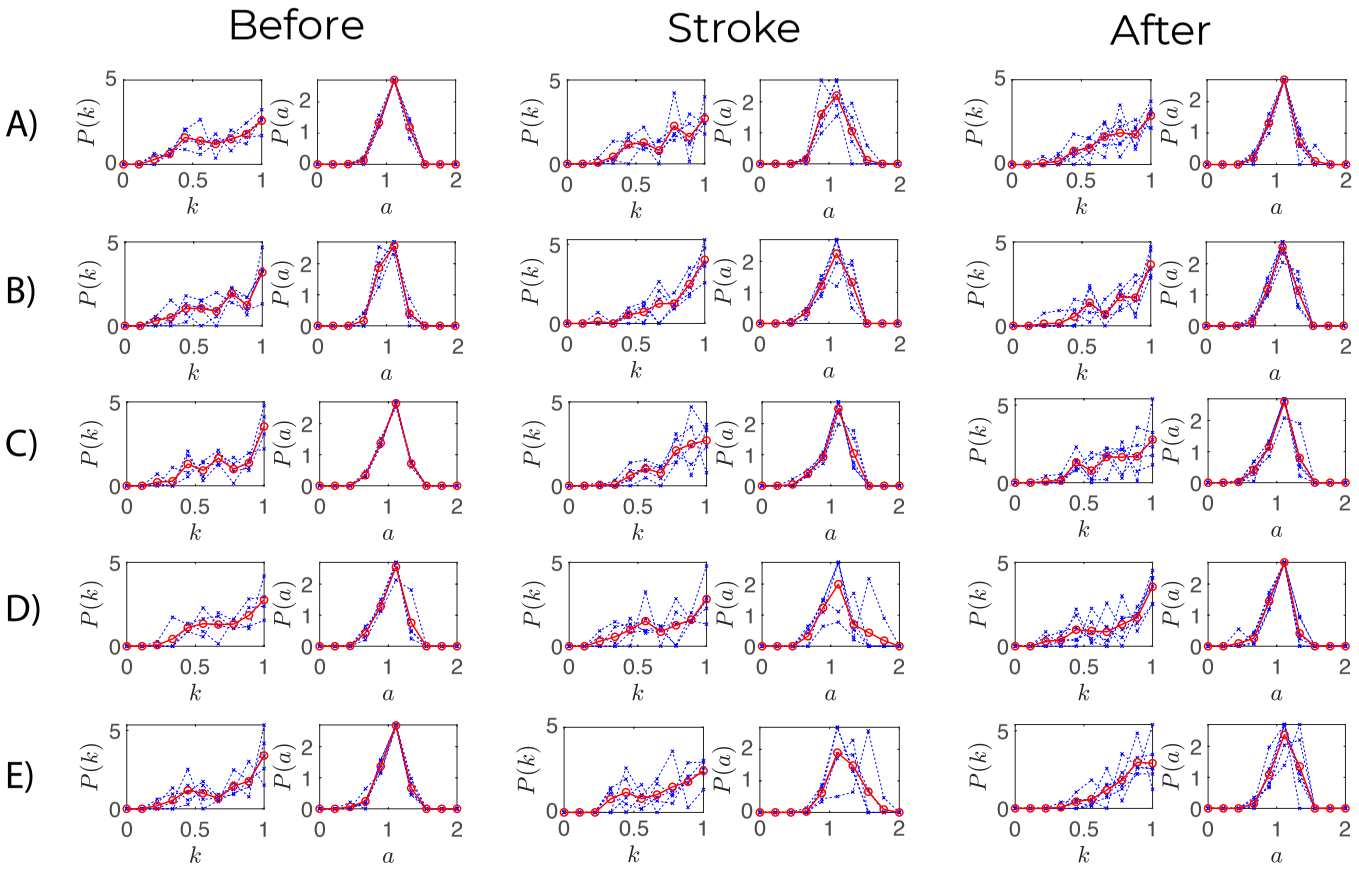

Figure 4.6: Recovered $P(\tilde{k})$ and $P(a)$ for 5 mice (identified by the letters running from A to E). Under the heading *Before*, we report the results obtained by analyzing data collected before the stroke over 4 different days of observation. Blue light traces (crosses) refer to reconstructions obtained from data collected over one single day, among those belonging to the group of pertinence. Red curves (circles) stand for the distribution averaged over individual traces. Under the heading *Stroke*, we report results which refer to 5 days immediately after the stroke with an analogous organization of the displayed plots and employed symbols. Under the heading *After*, we have organized the results which follow the analysis of the physiological signals, as acquired three weeks after the stroke.

Chapter 5

Reconstruction scheme for excitatory and inhibitory dynamics with quenched disorder: application to zebrafish imaging

The previous chapter proposed and tested against both synthetic and real data, an inverse scheme to quantify the statistics of neurons' excitability, while inferring, from global activity measurements, the, *a priori* unknown, distribution of network connectivities. The method employs an extended model of Leaky-Integrate and Fire (LIF) neurons, with short-term plasticity. Only excitatory neurons are accounted for in Chapter 4 and the approach was generalized so as to account for the dynamical heterogeneity, as stemming from the intrinsic degree of individual neurons' excitability. As mentioned above, individual excitability acts as a key component of the dynamics and yields irregular patterns of activity like those displayed in real measurements. The reconstruction scheme was applied in Chapter 4 to longitudinal wide-field fluorescence microscopy data of cortical functionality in groups of awake mice and enabled us to identify altered distributions in neuron excitability immediately after the stroke, and in agreement with earlier observation [147; 148; 149]. Conversely, rehabilitation allowed to recover a distribution similar to pre-stroke conditions.

The goal of this chapter is to push forward the reconstruction algorithm by accounting for the simultaneous presence of both excitatory and inhibitory neurons, in a refined variant of the inversion scheme proposed in Chapter 4[1]. Notice that already in [89] intertangled families of excitatory and inhibitory neurons have been considered, but only in a simplified setting where currents were assumed to be homogeneous. Relaxing this ansatz proves however mandatory when aiming at bridging the gap between theory and experiments, a challenge that we shall hereafter tackle. In particular, we will recast the dynamics of the examined LIF model in a reduced setting by grouping in different classes (excitatory and inhibitory) neurons which bear distinct values of the current a and of the connectivity k.

Our extended inverse method aims at computing the distribution of the currents, as well as the distributions of the connectivities, for respectively excitatory and inhibitory neurons, via an iterative scheme which self-consistently identifies the classes of neurons needed to interpolate the global activity field, supplied as an input to the algorithm. First, the performance of the method is evaluated in silico, against synthetically generated data. We then move forward to considering a direct application of the developed technique to custom-made two-photon Light Sheet (2PLS) microscope, optimized for high-speed (1 Hz) volumetric imaging of zebrafish larva (ZL, *Danio rerio*). Near-infrared (NIR) light is used for excitation, covering a wavelength range that is not visible to the larva in order not to induce unwanted visual responses. Hence 2PLS microscopy allows to record whole-brain activity with high temporal and spatial resolution, by preventing undesired external bias [153; 154; 155]. The experimental input is processed with a properly devised methodology to return a spatially resolved raster plot for the spiking activity of neurons over time, which provides the ideal input for the reconstruction method to work. A power law distribution of the in-coming connectivity of excitatory neurons is found, which is robust over a significant range of the imposed fraction of inhibitory neurons. Local degree distributions are also recovered by partitioning the whole brain in bound sub-domains, traced from annotated atlas [156; 157]. When manipulating experimental data one cannot distinguish among the contributions resulting from different neurons

[1]This work was done as a collaborative effort involving many parties who have contributed far greater towards the completion of the work than the authour and does not represent his primary research activity. The names and relevant contributions can be found on the published paper (or prepared manuscript) referred to the publications section in Appendices

(excitatory vs. inhibitory). A procedure is however developed which allows for the degree distribution of the excitatory neurons to be determined, while accounting for the role exerted by the population of inhibitory ones.

This chapter is organized as follows. Section 5.1 is devoted to introducing the model and the refined reconstruction scheme, followed by the results of challenging its performance against synthetically produced data in Section 5.2.1. We will then turn to present the experimental platform and discuss the details that relate to data processing. Processed data are supplied as an input to the mathematical reconstruction scheme to yield the results which are presented in Section 5.2.2. Finally, we will sum up and discuss our results.

5.1 General mathematical framework

5.1.1 The model

We use a Leaky Integrate and Fire (LIF) model to mimic the dynamics of individual neurons. Consider a pool of N LIF neurons and denote by $v_i(t)$ the membrane potential of neuron i. Further, label with $I_i^{syn}(t)$ the synaptic current due to the incoming connections with other neurons of the collection.

The dynamics of the membrane potential is hence ruled by the following equation

$$\frac{dv_i(t)}{dt} = a_i - v_i(t) + I_i^{syn}(t) \tag{5.1}$$

where a_i stands for the external input current of neuron i. This is a crucial quantity, as it sets the dynamics of the corresponding neuron, in the uncoupled regime. The critical value $a_i = 1$ separates between quiescent and active (spiking) regimes. When v_i reaches the threshold value v_{th}, neuron i emits a spike and the membrane potential v_i is reset to the base value v_r. Following [89], the membrane potential is rescaled by a suitable amount to have the spike threshold set at $v_{th} = 1$ and the rest potential at $v_r = 0$.

The Tsodyks, Uziel, and Markram model [150; 158] is assumed to describe the interactions among neurons, i.e. their coupling dynamics. More specifically, the dynamics of a synapse is expressed in terms of fractions of three different neurotransmitter states: active ($y_{ij}(t)$), available ($x_{ij}(t)$) and inactive ($z_{ij}(t)$), where i and j stand respectively for post-synaptic and pre-synaptic neurons. The obvious constraint $x_{ij}(t) + y_{ij}(t) + z_{ij}(t) = 1$ applies, for any time t.

During a spike of the pre-synaptic neuron, a fraction u_{ij} of neurotransmitters in the available state is activated. The time evolution of the three states

$$\dot{y}_{ij}(t) = -\frac{y_{ij}(t)}{\tau_{in}} + u_{ij}x_{ij}S_j(t) \tag{5.2a}$$

$$\dot{z}_{ij}(t) = -\frac{z_{ij}(t)}{\tau_r^i} + \frac{y_{ij}(t)}{\tau_{in}} \tag{5.2b}$$

$$x_{ij}(t) + y_{ij}(t) + z_{ij}(t) = 1 \tag{5.2c}$$

takes as input the spike train $S_j(t) = \sum_m \delta(t - t_j^*(m))$ of pre-synaptic neuron j emitting its n-th spike at time $t_j(n)$ [151]. The time is rescaled to the membrane time constant $\tau_m = 30ms$. The time constants are set to $\tau_{in} = 0.2$, $\tau_r^i = 3.4$ if the post-synaptic neuron i is inhibitory, or $\tau_r^i = 26.6$ if it is excitatory [89].

If the post-synaptic neuron i is excitatory, the fraction $u_{ij}(t)$ of neurotransmitters is set to the constant value of $U = 0.5$. Otherwise, $u_{ij}(t)$ evolves in time

$$\dot{u}_{ij}(t) = -\frac{u_{ij}(t)}{\tau_f} + U_f(1 - u_{ij}(t))S_j(t) \tag{5.3}$$

where $\tau_f = 33.25$ and $U_f = 0.08$ [89; 151].

Equations (5.2) are coupled to Eq. (5.1) via the synaptic current

$$I_i^{syn}(t) = \frac{g}{N} \sum_{j \neq i} A_{ij} y_{ij}(t) \tag{5.4}$$

where g is the coupling parameter and A_{ij} stands for the elements of the network adjacency matrix A. The matrix entry is $A_{ij} = 1$, if a link exists which goes from j to i, and provided j is an excitatory neuron. Conversely, $A_{ij} = -1$ if the starting node j identifies inhibitory neuron. On the other hand, if $A_{ij} = 0$ a direct connection from j and i does not exist.

Equations (5.2) can be cast in a more compact form so as to favour insight into the inspected processes and reduce the associated computational costs. To achieve this, we first notice that Eqs. (5.2) only depend on the pre-synaptic neuron j and the characteristics of the post-synaptic neuron i.

Equation (5.2a) can hence be split into two distinct equations:

$$\begin{aligned} \dot{y}_j^E(t) &= -\frac{y_j^E(t)}{\tau_{in}} + u_j^E x_j^E S_j(t) \\ \dot{y}_j^I(t) &= -\frac{y_j^I(t)}{\tau_{in}} + u_j^I x_j^I S_j(t), \end{aligned} \tag{5.5}$$

where the apexes E (Excitatory) and I (Inhibitory) reflect the specificity of the target neuron. Similar arguments apply to Eqs. (5.2b), (5.2c), and (5.3).

For each type of synapse, the average field, i.e. the fraction of neurotransmitters in the active state, is calculated as

$$\begin{aligned} Y_{EI}(t) &= \frac{1}{f_I N} \sum_{i \in \mathcal{I}} y_i^E(t) \\ Y_{EE}(t) &= \frac{1}{(1-f_I)N} \sum_{i \in \mathcal{E}} y_i^E(t) \\ Y_{II}(t) &= \frac{1}{f_I N} \sum_{i \in \mathcal{I}} y_i^I(t) \\ Y_{IE}(t) &= \frac{1}{(1-f_I)N} \sum_{i \in \mathcal{E}} y_i^I(t) \end{aligned} \tag{5.6}$$

where $\mathcal{E}$ and $\mathcal{I}$ are the ensemble of excitatory and inhibitory neurons, respectively; f_I stands for the fraction of inhibitory neurons in the network. The global fields are defined as

$$\begin{aligned} Y_E(t) &= -f_I Y_{EI}(t) + (1-f_I) Y_{EE}(t) \\ Y_I(t) &= -f_I Y_{II}(t) + (1-f_I) Y_{IE}(t). \end{aligned} \tag{5.7}$$

5.1.2 The heterogeneous mean-field ansatz.

The model described in the previous section is reformulated here in terms of a Heterogeneous Mean Field (HMF) approximation. The original neurons are classified according to their characteristics. More specifically, neurons of the same type (excitatory or inhibitory) and with the same incoming connectivity k and external current a are considered identical. Therefore, $L \times M$ equivalence classes are defined, where L (M) is the number of subintervals in which the value range of k (a) has been divided. Moreover,

we assume that neurons in the class k are subjected to a synaptic current proportional to their in-degree, i.e.,

$$\begin{aligned} \frac{g}{N}\sum_j A_{ij} y_j^E(t) &\longrightarrow \frac{g}{N} k Y_E(t) \\ \frac{g}{N}\sum_j A_{ij} y_j^I(t) &\longrightarrow \frac{g}{N} k Y_I(t) \end{aligned} \tag{5.8}$$

for the excitatory and inhibitory neurons, respectively. Following this assumption, the model can be rewritten as

$$\begin{aligned} \dot{v}_{k,a}^E(t) &= a - v_{k,a}^E(t) + \frac{g}{N} k Y_E(t) \\ \dot{v}_{k,a}^I(t) &= a - v_{k,a}^I(t) + \frac{g}{N} k Y_I(t) \\ \dot{y}_{k,a}^{(\dagger,*)}(t) &= -\frac{y_{k,a}^{(\dagger,*)}(t)}{\tau_{in}} + u_{k,a}^{(\dagger,*)}(t) x_{k,a}^{(\dagger,*)}(t) S_{k,a}^*(t) \\ \dot{z}_{k,a}^{(\dagger,*)}(t) &= \frac{y_{k,a}^{(\dagger,*)}(t)}{\tau_{in}} - \frac{z_{k,a}^{(\dagger,*)}(t)}{\tau_r^\dagger} \\ x_{k,a}^{(\dagger,*)}(t) + y_{k,a}^{(\dagger,*)}(t) + z_{k,a}^{(\dagger,*)}(t) &= 1 \end{aligned} \tag{5.9}$$

where $(\dagger, *)$ identify all possible pairs of post-synaptic and pre-synaptic neurons. Denote by $P_E(k)$ and $P_I(k)$ the in-degree distributions for the excitatory and inhibitory neurons, respectively, and $P(a)$ the external current distribution. Equations (5.9) can be closed by the consistency relations

$$\tilde{Y}_{\dagger *}(t) = \int_{k,a} P_*(k) P(a) y_{k,a}^{\dagger *}(t). \tag{5.10}$$

Taking in account the discretization of the defined classes of equivalence, Eq. (5.10) turns into

$$\tilde{Y}_{\dagger *}(t) = \sum_{l=1}^{L}\sum_{m=1}^{M} P_*(k_l) P(a_m) y_{k_l,a_m}^{\dagger *}(t), \tag{5.11}$$

where we have implicitly introduced the discrete counterpart of the continuous probability distributions

$$\mathbf{P}_*(\mathbf{k}) = (P_*(k_1), P_*(k_2), ..., P_*(k_L)) \text{ and}$$

$$\mathbf{P}(\mathbf{a}) = (P(a_1), P(a_2), .., P(a_M)).$$

5.1.3 Reconstruction scheme

In this section, we set up a general reconstruction scheme for recovering the a priori unknown distributions for the in-degree $P_E(k)$ and $P_I(k)$, as well as the external current $P(a)$. This is achieved by interpolating the available global fields $Y_E(t)$ and $Y_I(t)$, under the simplified HMF descriptive framework. The main steps of the reconstruction algorithm are schematically depicted in Fig. 5.1A.

As already mentioned, we assume the global fields $Y_E(t)$ and $Y_I(t)$ to be given. Then we integrate Eqs. (5.9), by using these global fields $Y_E(t)$ and $Y_I(t)$ as inputs to the model. The equations are initialized with variables $(v_{k,a}(t_0), y_{k,a}^{(\dagger,*)}(t_0), z_{k,a}^{(\dagger,*)}(t_0))$ randomly drawn from a uniform distribution, and generated so as to respect the constraints $v_{k,a}^{\dagger}(t_0) < 1$ and $y_{k,a}^{(\dagger,*)}(t_0) + z_{k,a}^{(\dagger,*)}(t_0) < 1$. Forced by the external fields $Y_E(t)$ and $Y_I(t)$, the governing equations are integrated forward and the variables $y_{k,a}^{\dagger *}(t)$ are stored for each class (k,a), type of synapse $(\dagger,*)$, and time t. This process is repeated for H independent realizations of the initial conditions. The average fraction of neurotransmitters in the active state, for each class (k,a) and synapse type, is computed at any time of observation t, i.e., $\left\langle y_{k,a}^{(\dagger,*)}(t) \right\rangle = 1/H \sum_{h=1}^{H} \left(y_{k,a}^{(\dagger,*)}(t) \right)_h$.

Then, the approximated global fields $\tilde{Y}_{\dagger *}$ are calculated, via Eq. (5.11), for an initial guess of the distributions $\mathbf{P_E}(\mathbf{k})$, $\mathbf{P_I}(\mathbf{k})$, and $\mathbf{P}(\mathbf{a})$. These latter are then recursively modified so as to improve the correspondence between the approximated fields and their true homologues $Y_{\dagger *}$.

Formally, for each $(\dagger,*) \in \{EE, EI, IE, II\}$, we aim at minimizing the function

$$F^{\dagger *}(\mathbf{P}_*(\mathbf{k}), \mathbf{P}(\mathbf{a})) = \sum_t |Y_{\dagger *}(t) - \sum_{k,a} \mathbf{P}_*(\mathbf{k}) \mathbf{P}(\mathbf{a}) \left\langle y_{k,a}^{\dagger *}(t) \right\rangle|^2. \qquad (5.12)$$

Note that the arguments of the above function are the target probability distributions $\mathbf{P}_*(\mathbf{k})$ and $\mathbf{P}(\mathbf{a})$ that one aims at inferring.

The iterative algorithm operates as follows. The distribution $\mathbf{P}(\mathbf{a})$ is initially frozen to a given profile and the quantities $y_{k_l}^{\dagger *}(t) = \sum_{m=1}^{M} P(a_m) \left\langle y_{k_l,a_m}^{\dagger *}(t) \right\rangle$

are hence evaluated. The inverse problem yields therefore

$$\begin{pmatrix} 1/\Delta k \\ Y_{\dagger *}(t_1) \\ Y_{\dagger *}(t_2) \\ Y_{\dagger *}(t_3) \\ \vdots \end{pmatrix} \approx \begin{pmatrix} 1 & 1 & 1 & \dots \\ y^{\dagger *}_{k_1}(t_1) & y^{\dagger *}_{k_2}(t_1) & y^{\dagger *}_{k_3}(t_1) & \dots \\ y^{\dagger *}_{k_1}(t_2) & y^{\dagger *}_{k_2}(t_2) & y^{\dagger *}_{k_3}(t_2) & \dots \\ y^{\dagger *}_{k_1}(t_3) & y^{\dagger *}_{k_2}(t_3) & y^{\dagger *}_{k_3}(t_3) & \dots \\ \vdots & \vdots & \vdots & \ddots \end{pmatrix} \begin{pmatrix} P_*(k_1) \\ P_*(k_2) \\ P_*(k_3) \\ \vdots \end{pmatrix}, \tag{5.13}$$

where the first row reflects the normalization condition. The problem is hence reduced to a linear system that can be readily solved to obtain a first estimate of the distributions $\mathbf{P_E}(\mathbf{k})$ and $\mathbf{P_I}(\mathbf{k})$.

As the second step, the in-degree distributions $\mathbf{P_E}(\mathbf{k})$ and $\mathbf{P_I}(\mathbf{k})$ are fixed to the solutions found at the previous iteration. Similar to step one, we evaluate the quantities $y^{\dagger *}_{a_m}(t) = \sum_{l=1}^{L} P_*(k_l) \left\langle y^{\dagger *}_{k_l,a_m}(t) \right\rangle$ and formulate the linear problem

$$\begin{pmatrix} 1/\Delta a \\ Y_{\dagger *}(t_1) \\ Y_{\dagger *}(t_2) \\ Y_{\dagger *}(t_3) \\ \vdots \end{pmatrix} \approx \begin{pmatrix} 1 & 1 & 1 & \dots \\ y^{\dagger *}_{a_1}(t_1) & y^{\dagger *}_{a_2}(t_1) & y^{\dagger *}_{a_3}(t_1) & \dots \\ y^{\dagger *}_{a_1}(t_2) & y^{\dagger *}_{a_2}(t_2) & y^{\dagger *}_{a_3}(t_2) & \dots \\ y^{\dagger *}_{a_1}(t_3) & y^{\dagger *}_{a_2}(t_3) & y^{\dagger *}_{a_3}(t_3) & \dots \\ \vdots & \vdots & \vdots & \ddots \end{pmatrix} \begin{pmatrix} P(a_1) \\ P(a_2) \\ P(a_3) \\ \vdots \end{pmatrix} \tag{5.14}$$

The above problem can be solved to obtained an updated estimate for the $\mathbf{P}(\mathbf{a})$. The overall procedure, consisting of two nested steps, is iterated until a maximum number of allowed cycles is reached, or, alternatively, the stopping criterion is eventually met.

Before proceeding in the analysis, we introduce a slightly modified notation. The in-degree k is normalized to the size of the network N. In formulae we will set $\tilde{k} = k/N$, with $\tilde{k} \in [0, 1]$. From hereon the distributions that constitute the target of the reconstruction scheme will be hence expressed as a function of $\tilde{k}$, instead of k.

5.2 Application to data

5.2.1 Synthetic data

In this section, we test the proposed reconstruction protocol against synthetic data. The reconstruction scheme was successfully validated on synthetic data for the case of homogeneous external current in [89; 159]. Here,

we test the reconstruction method on synthetic networks of excitatory and inhibitory neurons, assuming a quenched distribution of heterogeneous external currents. To this end, we generate a random graph with N nodes whose structural characteristic is contained in the signed $N \times N$ adjacency matrix A, which specifies the existence of (directed) links among pairs of adjacent nodes. Following the convention introduced above, negative entries ($A_{ij} = -1$) indicate that the starting node (j) is of the inhibitory type, whereas for positive elements ($A_{ij} = 1$) j belongs to the family of excitatory neurons. The network generation procedure is conceived so as to return a bell-shaped distribution for both $P_E(\tilde{k})$ and $P_I(\tilde{k})$ (see Fig. 5.1B). Quenched disorder in the input currents is introduced, the assigned currents being distributed according to a uni-modal profile $P(a)$ (see Fig. 5.1B). These are the exact distributions that we eventually seek to recover via the aforementioned reconstruction algorithm. Note that the domain of definition of $P(a)$ includes the bifurcation value $a = 1$.

With this setting, Eqs. (5.1) and (5.2) are integrated and the fields Y_E and Y_I are calculated by using Eqs. (5.6) and (5.7). This is possible because we have access to all information which pertain to the network architecture and to the heterogenous collection of randomly generated currents.

The recorded global fields Y_E and Y_I are used as inputs to the reconstruction scheme presented in the previous section. Figure 5.1B shows the comparison between true and estimated distributions, at the end of the reconstruction procedure and for one generation of the synthetic network. By inserting the estimated distributions into Eq. (5.11), we obtain the global fields $\tilde{Y}_E$ and $\tilde{Y}_I$. The comparison between estimated $(\tilde{Y}_E, \tilde{Y}_I)$ and true (Y_E, Y_I) global fields, as obtained by working on the index space, is presented in Fig. 5.1C. The agreement is excellent for both the inhibitory and the excitatory components.

When working with experimental data, however, one cannot isolate the contributions stemming from different neurons, grouped according to their specific traits (excitatory vs. inhibitory). This implies that the sums in Eq. (5.6), i.e. the input to the envisaged reconstruction scheme, cannot be in general accessed, as it was instead the case when working in the framework of the synthetic model considered above. To overcome this intrinsic limitation, we propose and test an alternative route, which performs adequately well when challenged against synthetic data. The idea is to propose an approximated version of the input Eqs. (5.6). To this end, we extend the sums

which run on the excitatory neurons to all neurons and compute, under this approximation, the fields Y_{EE} and Y_{IE}. To validate this hypothesis we operate with synthetic networks with unclassified neurons. It can be shown that the approximation for the fields Y_{EE}, Y_{IE} correctly describes Y_{EE}, but not Y_{IE}. This conclusion is supported by systematic numerical investigations (data not shown), that we carried out by varying the relative proportion of excitatory and inhibitory neurons. Building on the above, we therefore write:

$$Y_{EE}(t) \approx \frac{1}{N} \sum_{i=1}^{N} y_i^E(t), \tag{5.15}$$

which enables us to compute the approximated field Y_{EI} as

$$\begin{aligned} Y_{EI}(t) &= \frac{1}{f_I N} \sum_{i \in \mathcal{I}} y_i^E(t) = \\ &= \frac{1}{f_I N} \left(\sum_{i=1}^{N} y_i^E(t) - \sum_{i \in \mathcal{E}} y_i^E(t) \right) = \\ &= \frac{1}{f_I N} \sum_{i=1}^{N} y_i^E(t) - \frac{1}{f_I N} \frac{(1-f_I)}{(1-f_I)} \sum_{i \in \mathcal{E}} y_i^E(t) = \\ &= \frac{1}{f_I N} \sum_{i=1}^{N} y_i^E(t) - \frac{(1-f_I)}{f_I} Y_{EE}(t) \approx \\ &\approx \left(\frac{1}{f_I} - \frac{(1-f_I)}{f_I} \right) \frac{1}{N} \sum_{i=1}^{N} y_i^E(t) = \\ &= \frac{1}{N} \sum_{i=1}^{N} y_i^E(t). \end{aligned} \tag{5.16}$$

Finally, we can estimate Y_E as:

$$\begin{aligned} Y_E(t) &= (1-f_I) Y_{EE}(t) - f_I Y_{EI}(t) = \\ &= (1-2f_I) \frac{1}{N} \sum_{i=1}^{N} y_i^E(t). \end{aligned} \tag{5.17}$$

Remark that the above expression for Y_E is obtained without grouping the neurons in excitatory and inhibitory classes, but provided f_I, the fraction of inhibitory neurons, is eventually known. As we lack information on the

corresponding field Y_I, we can run the reconstruction scheme in a simplified setting which is solely targeted to reconstructing the probability distributions $P(a)$ and $P_E(\tilde{k})$. In Fig. 5.1D, the results of the revisited inversion method are displayed, having set f_I to the correct value, i.e. assuming the relative proportion of excitatory and inhibitory neurons which has been effectively employed in generating the synthetic dataset. The reconstruction algorithm is still capable of returning a faithful representation of both $P(a)$ and $P_E(\tilde{k})$. Conversely, when f_I is set to zero, the reconstruction scheme compensates for the missing inhibitory component by predicting a reduced average connectivity of the excitatory population, as compared to the correct value assumed in the data generation scheme, see Fig. 5.1E. In the following, we will apply the reconstruction scheme in this latter version to the analysis of 2PLS microscope images of living zebrafish larva.

5.2.2 Experimental data

In this section, we apply our reconstruction framework to calcium fluorescence microscopy data of zebrafish larva brain. Indeed, each time a neuron fires an action potential, the strong depolarization occurring triggers a rapid and transient increase of intracellular calcium concentration [160]. Thus, following calcium-dependent fluorescence dynamics represents an indirect measurement of neuronal spiking activity [161]. A description of the experimental set up is provided in the Methods section.

Data processing

In order to apply the inverse scheme to real data, it is necessary to preprocess the wide-field calcium images with the purpose of first identifying the location of the neurons. From individual traces of each spotted neuron, we will single out the spiking events, record the times of occurrence and build up the corresponding raster plot. This will serve as input to the reconstruction algorithm.

To this aim, data are first downsampled to 2×2 pixels so that the new pixel size is comparable to the neurons' nuclear size (Fig. 5.2A). For every new pixel, the maximum value of the calcium fluorescence is calculated and only the pixels with maximum intensity projection (MIP) above a threshold are identified as neurons. The threshold is fixed to the average MIP value over all the image pixels. Furthermore, we operate a moving average to

remove low-frequency fluctuation (Fig. 5.2B) and select as presumed neurons the pixels that show large asymmetry in the recorded traces. To implement this step, we compute the *skewness* from individual time series of the calcium activity and classify as neurons the pixels that yield a sufficiently skewed signal[2]. Figure 5.2C outlines the different phases of the process for one of the layers of the collection. More specifically, in Fig. 5.2C.i the MIP of the down-sampled pixels are depicted, in greyscale. In Fig. 5.2C.ii a binary representation of the whole brain is displayed where only pixels with MIP above the fixed threshold are highlighted. Lastly, in Fig. 5.2C.iii only the pixels which exhibit a strong asymmetric signal, i.e. the neurons with skewness above the imposed threshold, are shown. At the end of the selection process, the number of identified neurons is around $(1 \div 3) \times 10^3$ for each layer, which correspond to a total of 49×10^3.

Once the neurons are identified, we proceed to construct the raster plot. To this aim, for each selected neuron we analyze the time series of the calcium fluorescence to remove the background noise and detect events, which we call spikes. More specifically, a spike is defined as the time of threshold crossing. The thresholds are set to the mean value of the recorded time series plus two times the associated standard deviation. In addition, in order to avoid double detections due to noise, we discarded all events that succeeded the previous event by less than a minimum inter-event interval of 5 data points (5 seconds)[3] [115]. The general overview of the spike trains emitted by neurons in a sample layer results in a raster plot (Fig. 5.2D). Time is on the horizontal axis, whereas the vertical axis displays the neuron indices. Each spike of neuron i is associated with a red dot in the row i, at the corresponding time of spiking.

Results

As described in the previous section, we process 3D calcium fluorescence data so as to identify pixels containing neurons. Figure 5.3 shows the results of this identification for eight different layers of the zebrafish brain. Colours

[2]The skewness threshold is here put to 0.4. In doing so we select a number of putative neurons which is comparable to the known size of a zebrafish larva brain [162]

[3]An additional analysis has been carried out using a minimum inter-event interval of 2 data points. From the corresponding raster plot, the global fields have been calculated and they appear indistinguishable from the ones obtained using a minimum inter-event interval of 5 data points.

reflect the average cross-correlation[4] at lag zero of each neuron with all other selected neurons of the brain. The higher the correlation, the more reddish the colour displayed. The patterns of correlations are rather symmetric, an observation which can be interpreted as an a posteriori validation of the implemented procedure for automatic neurons selection. A movie which allows to navigate across successive layers of the whole 3D stack can be found in the SM.

The processing of data explained above allows us to obtain an experimental raster plot describing the events, or spikes, associated to each neuron. Indeed, the raster plot contains information about the spike train function $S_i(t)$, for all neurons i, and can be readily employed to recover the global field Y_E to be supplied as an input to the reconstruction scheme. More explicitly, the experimentally determined $S_i(t)$ is used to integrate Eqs. (5.2) and (5.3), by breaking the coupling with Eq. (5.1) which sets the evolution of the membrane potential[5]. This is of great advantage since Eq. (5.1) contains the specific information about the network connections, i.e., the adjacency matrix elements, which are a priori unknown. In other words, the raster plot provides us with a way to compute the global field (input of the reconstruction process described in section 5.1.3) without knowing the underlying structure of the network.

Since the true fraction f_I of inhibitory neurons is unknown, the global field Y_E in the approximated form [Eq. (5.17)] is computed for different values of f_I. In particular, we first reconstruct the in-degree distribution $P_E(\tilde{k})$ for the excitatory neurons and the external current distribution $P(a)$ for different values of f_I and we store the results[6]. Secondly, we computed the reconstruction error $MSE = 1/T \sum_t^T (Y(t) - \tilde{Y}(t))^2$ for all the considered values of f_I, comparing the estimated field $\tilde{Y}_E$ with the one used as input in the reconstruction scheme. Figure 5.4A reports on this comparison in the case of $f_I = 0.05$. In Fig. 5.4B, the MSE is plotted against different values

[4]Cross-correlation measures the similarity between two series at different time shifts, or lags. In formulae, the cross-correlation between two vectors x_t and y_t at lag τ is defined as the expected value of the product of the shifted copy of x_t and the complex conjugate of y_t, i.e., $R_\tau(x, y) = \mathbf{E}(x_{t+\tau} y_t^*)$, where the asterisk denotes the complex conjugation.

[5]The reactions parameters are set to the nominal values as declared above [89]. The same parameters are assumed in the reconstruction, and, in this respect, the model equations acts as a filter to transform the supplied fluorescence data in the ideal input for the inverse procedure to run.

[6]The coupling strength g is set to the (experimentally justified) value of 30 [89; 151; 163] adopted in the forward simulations of the model.

of f_I. Small errors are found over a large (and biologically meaningful) interval of values for f_I, approximately $f_I \in (0, 0.4]$. For this reason, we focus on five different choices of f_I, i.e., $f_I = 0.05, 0.1, 0.2, 0.3, 0.4$, to explore a wide range of results for the reconstruction scheme, when sampling the region of parameters in which the interpolation of the experimental time series proves accurate. The reconstructed distributions $P(a)$ and $P_E(\tilde{k})$ are plotted in Figs. 5.4C,D. For every choice of f_I, over the spanned interval, the reconstructed distributions show common features. In particular, the external current distribution $P(a)$ is peaked in the vicinity of the critical value $a = 1$ (Fig. 5.4C). The neurons associated to $a > 1$ get self-excited and promote the activation of other neurons which would be instead quiescent in the uncoupled limit. The small bumps that are found for relatively large values of the intensities a can be traced back to the high-frequency component of the signal to be interpolated, and, as such, bear limited fundamental interests. The large-scale dynamics of the recorded time-series, including the heterogeneous modulation of the macroscopic field oscillations, is instead encoded in the distribution of intensities that define the bulk of $P(a)$, i.e. the limited excerpt of curve which is found in correspondence of the leftmost portion of the support in a.

The reconstructed in-degree distributions $P_E(\tilde{k})$ for the excitatory neurons, at different values of f_I, are depicted in Fig. 5.4E, in log-log scale. Although over a limited support in $\tilde{k}$, the obtained distributions seem to display a power-law decay, $P_E(\tilde{k}) \propto \tilde{k}^{-\alpha}$, the characteristic exponent α being only modestly influenced by the chosen value of f_I. Our findings suggest that excitatory neurons are organized in a network with few hubs and many more peripheral nodes.

As an additional test, we partition the full set of identified nodes in 10 different populations, reflecting distinct anatomical regions, as follows available atlases [157; 162]. The reconstruction algorithm is then applied to each of the selected region, treated as independent from the surrounding context, so as to access the local degree distribution. Results, displayed in Fig. 5.5, are in line with those reported in Fig. 5.4. Moreover, neurons characterized by a significant connectivity, the above-referenced hubs, seem unevenly distributed across different anatomical regions.

5.3 Discussion

Reconstructing structural and functional information from brain activity represents a topic of outstanding importance, which can in principle trigger applied and fundamental fallout. In Chapter 4 we presented, and successfully tested, an inverse scheme which aimed at inferring the distributions of both firing rates and networks connectivity, from global activity fields. The method builds on the Leaky-Integrate and Fire (LIF) model which we modified by the inclusion of quenched disorder, in the assigned individual currents. The imposed degree of heterogeneity in the currents yields non-trivial a-periodic patterns, which resemble those recorded in vivo. The dynamical model considered in the previous chapter solely included the population of excitatory neurons. Starting from this background, we here have generalized the reconstruction procedure of Chapter 4 so as to account for the simultaneous presence of both excitatory and inhibitory neurons, while still dealing with the effect of the current heterogeneity. The dynamics of the examined multi-species LIF model is recast in a simplified framework, by grouping together neurons that belong to the same class (inhibitory vs. excitatory), while sharing the similar currents and in-degree. The output of the reduced model, driven by the excitatory and inhibitory global fields, is self-consistently used to seed an iterative scheme which seeks at fitting the supplied fields, via suitably adjusting the unknown distributions. These latter are the distributions of the incoming degrees for, respectively, excitatory and inhibitory neurons, as well as the distribution of the imposed currents. The method is tested on synthetic data and yields satisfying performances. Having in mind applications to real data, we also dealt with a setting where it is not possible to separate the contribution that pertains to the excitatory component from that stemming from the inhibitory counterpart. In this case, we propose and test a procedure which enables to recover the distribution of incoming degrees for the network of excitatory neurons (assumed predominant), while gauging the role exerted by inhibitors.

The devised protocol is then applied to whole-brain functional data resulting from light-sheet calcium imaging of a zebrafish larva. The experimental input is processed with an automatic procedure which allows us to identify putative neurons , and to extract their fluorescence signal. Remarkably, the cross-correlation maps produced show a high grade of clusterization, which faithfully matches the anatomical boundaries of multiple brain regions identified using zebrafish brain atlases [156; 157]. From the

calcium signal displayed by each selected neuron we build up an experimental representation of the raster plot of the spiking activity of the zebrafish brain, which forms the input to the reconstruction scheme. A power law distribution of the in-coming connectivity of excitatory neurons is found, which is only modestly affected by the imposed fraction of inhibitors. Local degree distributions are also reconstructed by analysing the signal from specific regions, which correspond to distinct anatomical areas. Interestingly, the anatomical districts considered in the analysis can be divided into two different groups, according to the reconstructed probability distributions of both their excitatory incoming connections $P_E(\tilde{k})$ and excitability $P(a)$. The first group, including dorsal thalamus, medial tegmentum, superior raphe, hindbrain and spinal cord, is characterized by higher connections and lower excitability. Conversely, the second group, comprising telencephalon, habenulae, optic tectum and cerebellum, is described by lower connections and higher excitability. The reconstruction scheme reflects the specific functional connectivity of the larval brain during spontaneous activity precisely under these experimental conditions. Indeed, during measurements the zebrafish larva is embedded in agarose, and thus exposed to a diffused tactile stimulation, which could explain the higher incoming connections calculated for the dorsal thalamus, a sensory relay station [164; 165]. Furthermore, despite being mechanically and pharmacologically immobilized, larval attempts to escape the restrained condition could account for the higher incoming excitatory connections calculated for dorsal raphe (whose activity has been correlated with arousal state, vigilance and responsiveness [166]) and for the most caudal regions, namely hindbrain and spinal cord, responsible for the initiation of motor behaviours [167; 168]. Moreover, in this scenario, we observe a lower probability distribution of incoming excitatory connections for cerebellum. This result may be associated to the function of motor coordination and refinement [169; 170] of this region, typically related to the actual execution of a movement. Finally, since the measurement is performed in complete darkness, the larva is not exposed to any visual cue (the IR laser used for two-photon excitation is not perceived by the larval visual system) and this could explain the lower incoming connections calculated for the optic tectum, the main retinorecipient structure in the zebrafish brain [171; 172]. The large-scale oscillations in the recorded time series reflect back in the recovered distribution of currents: a significant fraction of neurons appear to operate in the quiescent state, while a minority self-excite to orchestrate

the dynamics of the ensemble.

5.4 Materials and Methods

5.4.1 Validity of the HMF approximation

We here challenge the predictive ability of the HMF approximation. To this end, we first calculate the average inter-spike interval (ISI) – the average distance in time between successive spikes – for the system in its original formulation, i.e. in the space of the nodes. The computed ISI is confronted to the homologous quantity obtained under the HMF scenario. The comparison is drawn in Fig. 5.6, for both excitatory and inhibitory neurons, and confirm the accuracy of the reduced HMF scheme.

5.4.2 Experimental setup

The experimental optical setup employed is a modified version of the setup described in detail in [173]. Briefly, 930 nm NIR light is generated by a pulsed titanium-sapphire oscillator (Chameleon Ultra II, Coherent) and conditioned by a pulse compressor (PreComp, Coherent). After being attenuated by a combination of a half-wave plate and a GlanâThompson polarizer, the beam passes through an electro-optical modulator that periodically switches its polarization plane orientation between two states: parallel or orthogonal to the optical table surface. Then a pair of retarders are used to pre-compensate for polarization distortions. After that, the beam is routed to the galvanometric mirror assembly and scanned by a resonant galvanometric mirror (CRS-8 kHz, Cambridge Technology) along larval rostro-caudal direction, to generate the digitally-scanned LS, and by a closed-loop galvanometric mirror (6215H, Cambridge Technology) along larval dorso-ventral direction. Finally, the beam is relayed to an objective (XLFLUOR4X/340/0,28,Olympus), placed at the lateral side of the larva, by a scan-lens (50 mm focal length), a tube-lens (75 mm focal length) and a pair of relay lenses (250 mm and 200 mm focal lengths).

Differently from the setup described in [173], a polarizing beam splitter (PBS) is present between the tube-lens and the first relay lens and the optical components downstream the PBS are duplicated on the opposite side of the larva. In this way, the excitation light is steered on one optical arm or on the other depending on its instantaneous polarization orientation by the PBS.

The detection arm of the microscope is identical to what described in [173]. A water-immersion objective (XLUMPLFLN20XW, Olympus) placed on the dorsal side of the larva collects the emitted green fluorescent light while being scanned along the axial dimension by an objective scanner (PI-FOC P-725.4CD, Physik Instrumente) synchronously with the closed-loop galvanometric mirror oscillations. The optical image is then spectrally filtered (FF01-510/84-25 nm BrightLineÂ®, Semrock) and projected on a camera (ORCA-Flash4.0 V3, Hamamatsu) sensor by a sequence of two tube lenses (300 mm and 200 mm focal lengths) and an objective (UPLFLN10X2, Olympus).

The larvae were imaged with volumetric acquisitions (frequency: 1 Hz) composed by 31 planes spaced by 5 μm and with a pixel size of about 2×2 μm^2.

We employed a transgenic strain of zebrafish larvae Tg(elavl3:H2B-GCaMP6s) [174; 175] in homozygous albino background that express the fluorescent calcium indicator GCaMP6s under a pan-neuronal promoter and with a nuclear localization. Sample mounting was performed as described in [176]. Briefly, before the acquisition each larva was immersed in a solution of the paralyzing agent d-tubocurarine (2 mM; 93750, Sigma-Aldrich), included in 1.5% (w/v) low gelling temperature agarose (A9414, Sigma-Aldrich) in fish water (150 mg/L Instant Ocean, 6.9 mg/L NaH2PO4, 12.5 mg/L Na2HPO4, pH 7.2) and mounted on a custom-made glass support immersed in thermostated fish water. The animals were maintained according to standard procedures [177] and observed at 4 days post-fertilization. Fish maintenance and handling were carried out in accordance with European and Italian law on animal experimentation (D.L. 4 March 2014, no. 26).

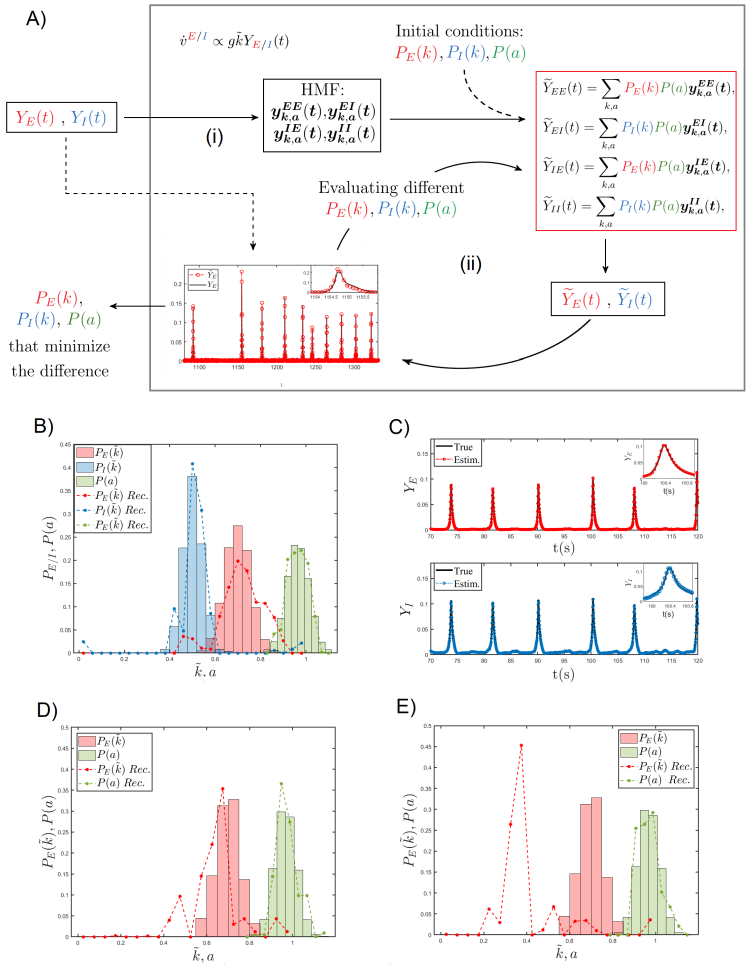

Figure 5.1: A) Schematic outline of the reconstruction procedure. The global fields $Y_E(t)$ and $Y_I(t)$ constitute the inputs of the model in the HMF approximation (i). Different choices for the probability distributions $P_E(k)$, $P_I(k)$, and $P(a)$ are iteratively tested in order to find the best match between the input fields and the reconstructed fields, as obtained by using the equations displayed in the red box (ii). B) Outcome of the reconstruction procedure: the true probability distributions of a synthetic network are compared with those obtained with the proposed reconstruction method. A random network with $N = 5000$ is considered here. The fraction of inhibitory neurons is set to $f_I = 0.05$. The number of classes defined in the HMF approximation for the in-degree and the external current is $L = 250$ and $M = 250$ respectively. C) Comparison between the true global fields and the ones obtained via the reconstructed distributions. The plot in the inset is a zoom-in of a peak.

Fig. 5.1 continued on next page

Fig. 5.1 continued
D-E) Outputs of the reconstruction are compared with the true external current probability distribution $P(a)$ and the true in-degree distribution $P_E(k)$ for the excitatory neurons of the same network; the network is made of $N = 1000$ neurons of which a fraction $f_I = 0.2$ are inhibitors. In the HMF approximation, one hundred classes have been defined for both the in-degree and external current, namely, $L = 100$ and $M = 100$. In D) the correct fraction of inhibitory neurons is taken into account, while in E) the inhibitory neuron effects are not considered.

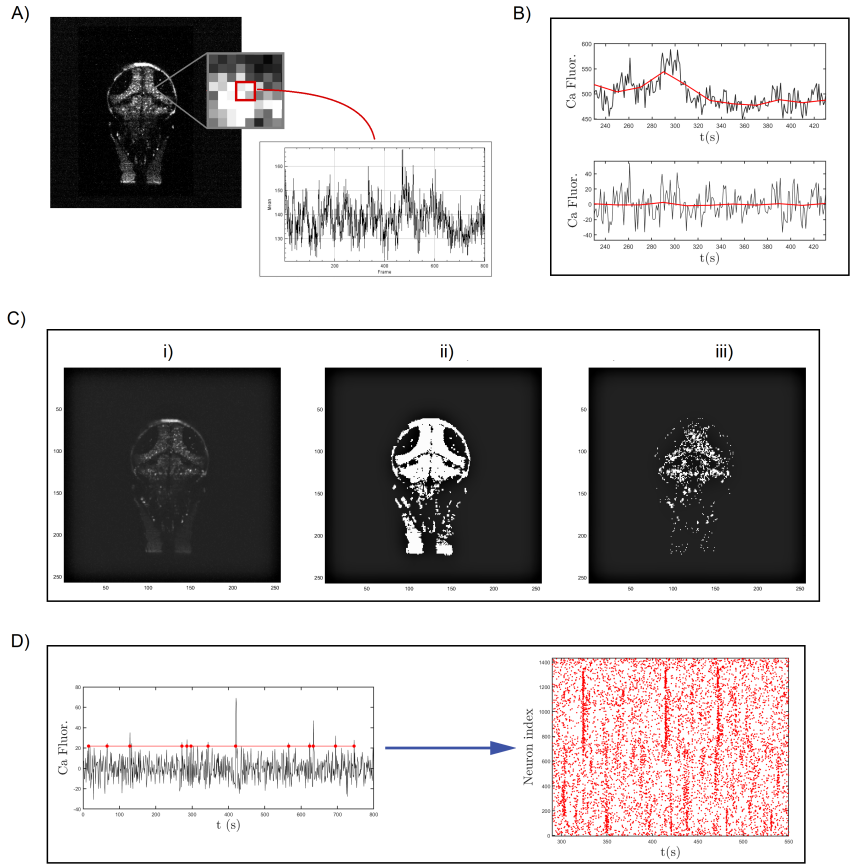

Figure 5.2: Main steps of experimental data elaboration. Every layer of the imaged 3D zebrafish brain is spatially downsampled, as shown in panel A) in order to obtain signals from pixel ensembles of size comparable to a neuron (2×2 pixels). B) Detrending for slow oscillations by subtraction of moving average. C) Results of neurons selection for one of the layers: (i) raw data, (ii) selection of pixels with maximum value above a fixed threshold, and (iii) only pixels with skewness larger than 0.4. At the end of the neurons selection procedure, the number of identified neurons in the whole brain is about $5 \cdot 10^4$. D) Procedure to obtain the experimental raster plot starting from calcium fluorescence time series of the selected neurons. A spike is identified by its upwards threshold crossing time.

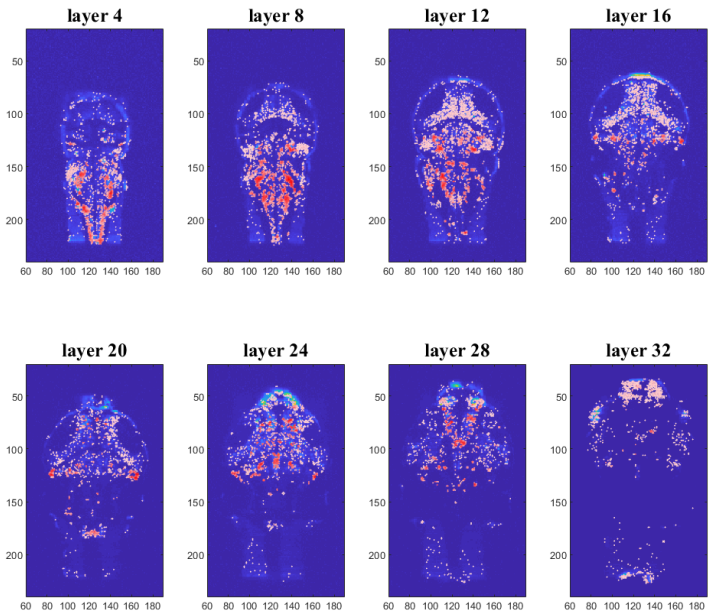

Figure 5.3: Detected neurons for eight different layers of the zebrafish brain. Colours represent the average cross-correlation of each neuron with all the others selected neurons of the brain.

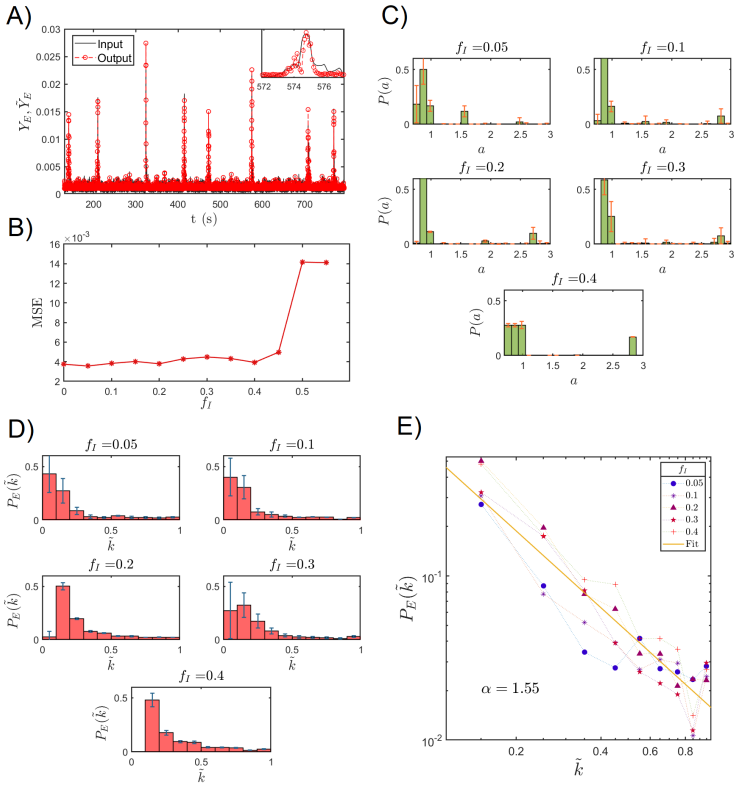

Figure 5.4: Reconstruction of the two distributions $P(a)$ and $P_E(\tilde{k})$ from calcium fluorescence microscopy data of zebrafish larva brain. A) Comparison between the global field obtained from the experimental raster plot and the one that follows the reconstructed distributions $P_E(\tilde{k})$ and $P(a)$, for a fraction $f_I = 0.05$ of inhibitory neuron. B) Mean square error $MSE = 1/T \sum_t^T (Y(t) - \tilde{Y}(t))^2$ for different choices of f_I. C-D) Reconstructed probability distributions $P(a)$ and $P(\tilde{k})$ for five different choices of f_I. For each setting, we ran $H = 50$ independent realizations of the iterative reconstruction scheme, starting from different initial conditions. The histograms represent the mean values and the error bars stands for the associated variance. E) In-degree probability distributions in logarithmic scale and their best linear fitting.

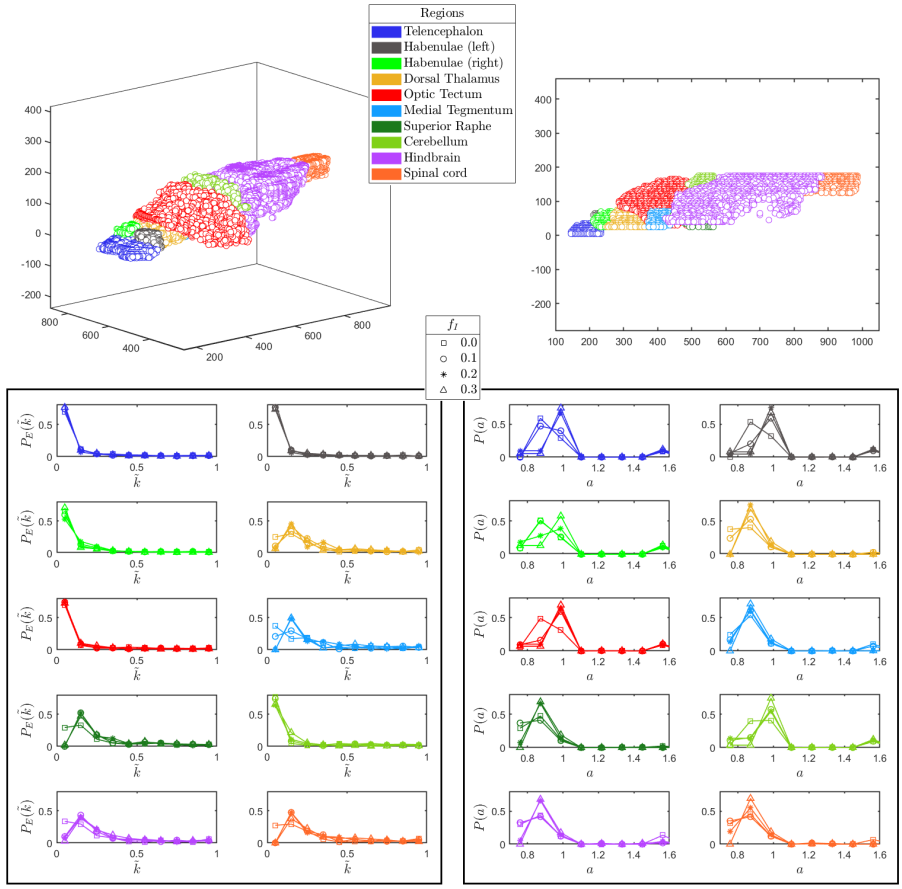

Figure 5.5: The reconstructed probability distributions $P_E(\tilde{k})$ (left) and $P(a)$ (right) are shown for ten different regions of the brain. The 3D images at the top display the relative spatial positions of the ten selected regions (as listed in the legend).

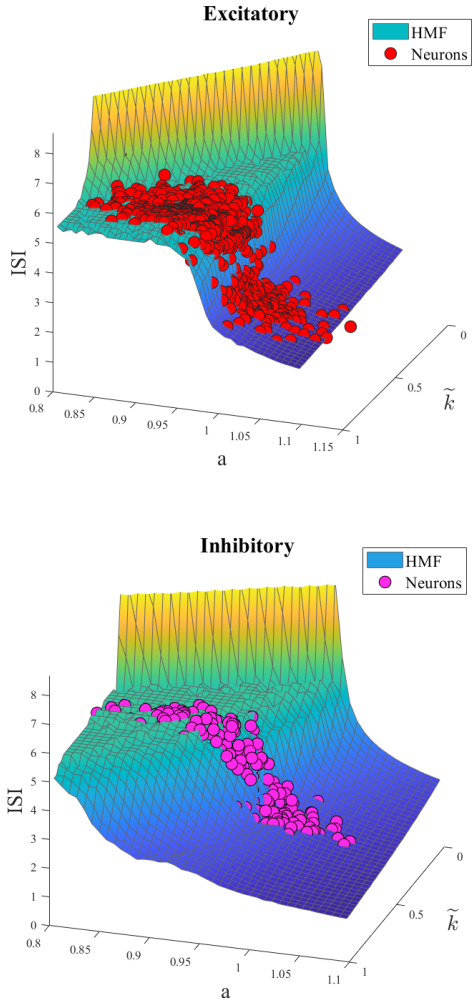

Figure 5.6: The ISI is computed for both excitatory (red symbols, top panel) and inhibitory (purple symbols, bottom panel) neurons. The prediction based on the HMF approximation yields the continuous curves. Here $N = 1000$ and $f_I = 0.2$.

Chapter 6

Prestrain induced contractions in Elastic Networks

The previous chapters have introduced and tested methods of inferring structural information from measurements of either local or global phenomenon together with the knowledge of the general governing dynamics of the processes that evolve on the unknown underlying network support. We have validated these methods on various synthetic scenarios following which we successfully applied them to real-world datasets to reveal fundamentally relevant insights about the structure of brains with in the context of stroke recovery. These chapters, in other words, have relied on the relationship between structure and function to formulate an inverse protocol that utilizes the collective, or mean, output of the systems to go back to structure.

When looking at macroscopic behaviours, small and local perturbations of the topological structure melt into mean/average features which, however, depends on local properties in a very complex way. In this last chapter, we study an interesting phenomenon where a desired function is induced, in this case, an overall contraction of the network, through zero-mean noise-like global prestrain applied across a peculiar class of networks. The analysis presented here attempts to describe the effect of this prestrain by leaning on the average effect it has on the network. This chapter also shows that here the structure plays a very limited role in the networks ability to perform this desired function.

Mass-spring networks or Elastic Network Models (ENMs) have been studied extensively due to their potential to model many interesting real-world

phenomenon. Earlier applications of such networks have been in the simulation of deforming bodies such as clothes and other fabric-like materials for computer graphics [178; 179; 180]. Recently, soft deforming bodies of a biological nature have been studied using ENMs with applications ranging from the study of facial tissue [181] to simulation of body organs in a surgical context [182]. Even smaller micro-scale biological phenomena, such as the membrane mechanics of cells, have benefited from the simplicity of ENMs [183; 184]. This is in part due to the efficiency and low computational complexity of ENMs compared to other competing simulation frameworks such as finite elements methods [185].

When it comes to the study of large molecular structures such as proteins, coarse-grained ENMs have been shown to be computationally more efficient than the more accurate atomic models which do not scale as well with the number of atoms or molecules to be simulated [186]. In such studies, the nodes of the ENM act as single amino acid residues, while the links model the inter-residue potentials. Despite the obvious simplifications introduced in their formulation, ENMs have been shown to capture not only the folding and unfolding of conformations, but also fluctuations around these shapes [187; 188; 189]. The normal modes of vibration ENMs can also describe even the large-amplitude motions related to ATP binding and hydrolysis in various molecular machines and motors [190; 191; 192].

Inspired by protein-machines, there is a growing trend to design mechanical networks that perform specific prescribed tasks [193]. Abstract networks are also at the basis of many coordination algorithms in robotics, such as consensus and formation control [194].

With potential interest ranging from material sciences to biophysical system and robotics, we propose a novel method that uses a random, zero-mean prestrain to induce contractions in 1D elastic networks. Prestrain is an important concept in many diverse fields, from tissue and bio-film engineering [181; 184] in the biological realm, to the design of elastomer-based artificial muscle actuators [195; 196; 197; 198] in the realm of robotics.

Starting from an intuitive explanation as to the nature of this contraction within the proposed framework, we develop an analytical theory to show how the strength of the noise affects the final contraction. We also explore how the topology of these contacting networks affect the final state by numerically testing Watts-Strogatz [56] networks and scale-free networks [199] of, respectively, varying rewiring probability and degree exponent. It

is found that the amount of contraction depends mainly on the magnitude of the noise, and the effect of the topology fades as the size of the network increases, i.e. in the thermodynamic limit.

6.1 Problem statement

We consider a network composed of point masses linked by linear springs with a spring constant $k = \frac{\gamma}{l_0}$, where l_0 is the rest length of the spring and γ can be regarded as the mechanical stiffness of the springs (proportional to the Young's modulus of the material composing the spring). The positions, x_i, of N number of masses are initialised at a regular spacing over a line segment of length $[-5N, 5N]$[1], so that they are equidistant. In the following, the connections among masses, corresponding to springs are generated according to the Watts-Strogatz method [56], unless otherwise stated. In this way, networks of increasing disorder or randomness can be created by starting from a regular lattice (of N nodes) with a specified number of links to each neighbour. Each link is then rewired randomly with set rewiring probability p.

Once the positions of the masses have been initialised and the links between them have been assigned, we set the rest length $l_{0_{ij}}$ of the spring connecting masses j and i, such that the system is at equilibrium. In formulae, this means $l_{0_{ij}} = |x_j - x_i|$.

A prestrain is then applied to the system by changing the rest length of the springs as $l_{0_{ij}} \mapsto \hat{l}_{0_{ij}} = l_{0_{ij}}(1 + \delta_{ij})$, where $l_{0_{ij}}$ refers to the original rest length of the spring connecting masses j and i, and $\hat{l}_{0_{ij}}$ refers to the new rest length after perturbation. For each spring, the prestrain term δ_{ij} is drawn from a random uniform distribution over the range $\delta \in [-\delta_{max}, \delta_{max}]$. The system is then allowed to relax to its new equilibrium.

The dynamics of the system can be modelled by the following set of ordinary differential equations:

$$\ddot{x_i} = \sum_j A_{ij}\gamma \left(\frac{1}{\hat{l}_{0_{ij}}} - \frac{1}{l_{ij}} \right) (x_j - x_i) - \eta \dot{x_i} - F_{r_{ij}} \tag{6.1}$$

where $l_{ij} = |x_j - x_i|$ and $\mathbf{A}$ is the adjacency matrix of the network, i.e. $A_{ij} = A_{ji} = 1$ if there exists a spring between masses i and j and

[1]The choice of 5 is arbitrary, however it is important for the length of the system to scale linearly with N for meaningful comparisons of networks of different.

$A_{ij} = A_{ji} = 0$ otherwise. Dissipation has been modelled by adding a viscous term with coefficient η. The term $F_{r_{ij}}$ models simple rigid sphere interaction, preventing the masses from switching their relative ordering along the segment as the system relaxes. For the simulation described below, this term is set to $F_{r_{ij}} = (x_j - x_i)^{-3}$. However, as the theoretical analysis shows, the exact form of this term does not matter, as long as masses do not switch order during relaxation.

Given that links share the same stiffness γ, i.e. have a spring constant k that depends on the rest length, the network has tendency to contract when subject to the prestrain described above. This is because the zero mean perturbation of rest length $l_{0_{ij}} \mapsto \hat{l}_{0_{ij}} = l_{0_{ij}}(1 + \delta_{ij})$ creates a perturbed distribution of spring constants

$$\hat{k}_{ij} = \frac{\gamma}{l_{0_{ij}}(1 + \delta_{ij})} \tag{6.2}$$

that is biased. In other words, the uniform distribution of prestrain $P(\delta)$ results in a distribution of k that is skewed more towards stronger and shorter springs. Hence, springs with negative prestrain ($\delta_{ij} < 0$) become stiffer than springs with positive prestrain.

6.2 Expected Shrinkage

The exact dynamics of Eq. (6.1) is difficult to obtain analytically due to the presence of the nonlinear term $F_{r_{ij}}$. Therefore, here only the expected value of the steady-state position x_i is studied. This allows the analysis of the mean outcome of the problem within given bounds.

To this end, let us note at first that the problem can be simplified by making use of the fact the nodes cannot swap positions during motion thanks to the term $F_{r_{ij}}$. Let us then define $\dot{x} = v_i$ and rewrite the model in Eq. (6.1) in matrix form as

$$\dot{\overrightarrow{V}} = \gamma(\mathbf{L}\overrightarrow{X} - \overrightarrow{B}) - \eta\overrightarrow{V} \tag{6.3}$$

where each element of the vector $\overrightarrow{B}$ is $B_i = \sum_j A_{ij}\ sign\{x_j - x_i\}$ and each element of the Laplacian operator matrix $\mathbf{L}$ is defined as

$$L_{ij} = A'_{ij} - k'\delta_{ij} \tag{6.4}$$

Here, the following quantities are defined to simplify the notation: $A'_{ij} = \frac{A_{ij}}{l_{0_{ij}}}$ and $k'_i = \sum_j A'_{ij}$.

Note that the vector $\overrightarrow{B}$ is a constant as long as the masses keep their relative ordering, i.e. do not swap positions. Furthermore, the repulsion term F_{ij} that models the rigid sphere collisions in Eq. (6.1) has been omitted in Eq. (6.3). This was done on the assumption that this repulsive force is active only on a very short range, so that it does not significantly alter the final state of the system. In summary, we assume that effect of the rigid sphere collisions can be captured by having a fixed vector $\overrightarrow{B}$ in the following analysis. This assumption will be validated *a posteriori* by comparing the predictions from the analytical theory with numerical tests.

It is important to note that the system is in equilibrium $\left(\overrightarrow{V}_0, \dot{\overrightarrow{V}}_0\right) = (0,0)$ before the prestrain is applied, therefore the initial positions $\overrightarrow{X_0}$ must satisfy

$$L_0 \overrightarrow{X_0} = \overrightarrow{B} \tag{6.5}$$

where L_0 is the initial, unperturbed Laplacian matrix from Eq. (6.4) formed from the initial rest lengths $l_{0_{ij}}$.

The expected final equilibrium position can be estimated by setting $\dot{\overrightarrow{V}} = \overrightarrow{V} = 0$, so that the Eq. (6.3) reads

$$L(\delta)\overrightarrow{X_f} = \overrightarrow{B} \tag{6.6}$$

where X_f denotes the final positions of the masses.

Upon perturbation, the only term that is directly affected by the prestrain δ is the Laplacian $\mathbf{L}$. Hence, by taking the expected value of both sides of Eq. (6.6), one obtains

$$\langle L(\delta)\rangle\langle\overrightarrow{X_f}\rangle = \overrightarrow{B} \tag{6.7}$$

By integrating each term over the noise distribution $\langle L_{ij}\rangle = \int_{-\delta_{max}}^{\delta_{max}} L_{ij}(\delta)P(\delta)d\delta$ with $P(\delta) = \frac{1}{2\delta_{max}}$ we can derive

$$\langle L_{ij}\rangle = \psi L_{0_{ij}} \tag{6.8}$$

where the shrinkage factor ψ is defined as

$$\psi = \frac{1}{2\delta_{max}} ln\left(\frac{1+\delta_{max}}{1-\delta_{max}}\right) \tag{6.9}$$

Combining Eq.(6.7) with Eq.(6.8) one obtains

$$L_0\psi\langle\overrightarrow{X_f}\rangle = \overrightarrow{B} \tag{6.10}$$

The expected relative shift of each mass can thus be found by comparing Eq. (6.10) and Eq. (6.5) as

$$\frac{1}{\psi} = \frac{\langle x_{f_i}\rangle}{x_{0_i}} \tag{6.11}$$

where x_{0_i} and x_{f_i} are the i-th elements of the initial position vector $\overrightarrow{X_0}$ and expected final position vector $\langle\overrightarrow{X_f}\rangle$, respectively.

Note that ψ is only a function of the maximum prestrain δ_{max}, and hence the expected shift of each mass, as described by Eq. (6.11), is only affected by δ_{max}. In fact, as it can be seen from the plot in Fig.6.1, numerical simulations of the process described in the previous section match remarkably well with the theoretical predictions of shrinkage even with relatively small networks of size $N = 2000$. This also confirms our assumption that the effect of the rigid sphere collisions is captured by considering the vector $\overrightarrow{B}$ as constant.

It should also be noted from Fig. 6.1 that $\frac{x_{f_i}}{x_{0_i}} < 1$ for the test points shown and therefore the networks are shrinking, as expected. The shrinkage of the final state of the system can be measured via the radius of gyration

$$R_g^2 = \frac{1}{N}\sum_{i=1}^{N}(x_i - x_m)^2 \tag{6.12}$$

where x_m refers to the centre of mass of the system. This can used to compute the relative shrinkage $\Delta R_g^2 = \frac{(R_{g_f}^2 - R_{g_0}^2)}{R_{g_0}^2}$, where $R_{g_0}^2$ and $R_{g_f}^2$ are, respectively, the initial and the final radii of gyration. Thanks to Eq. (6.11), the expected value for the final radius of gyration can be written in terms of the shrinkage factor ψ as

$$\langle R_{g_f}^2\rangle = \frac{1}{\psi^2}R_{g_0} \tag{6.13}$$

with the expected relative shrinkage then reading

$$\langle\Delta Rg^2\rangle = \frac{1}{\psi^2} - 1 \tag{6.14}$$

Note that, in the setting considered in this paper, the prestrained elastic networks always shrink on average. In fact, given a maximum prestrain

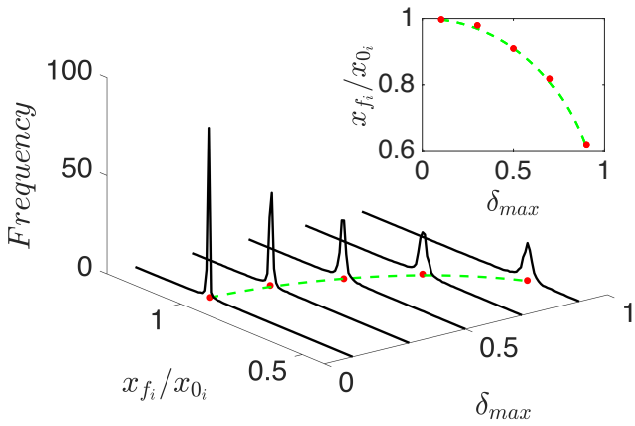

Figure 6.1: The solid black lines show histograms of x_{f_i}/x_{0_i} plotted for all nodes of the network. For each of the values of maximum noise δ_{max} shown, a new network was generated and tested according to the method outlined in the text. The tested networks have been created according to the Watts-Strogratz strategy [56] with rewiring probability $P = 0.7$ and are of size $N = 2000$ masses. The dotted green line plots the expected shift per node, $1/\psi$, against δ_{max}. The red dots mark the mean of each of the histograms. A top view of the plot is shown in the inset.

between 0% and 100% (i.e. $\delta_{max} \in (0, 1)$), $\psi > 1$ and hence, from Eq. (6.14), $\langle \Delta Rg^2 \rangle < 0$. It should also be remarked that a similar analysis can be performed using the distribution of prestrained spring constants $P(k)$ instead of the distribution of prestrain $P(\delta)$ to obtain the same results.

6.3 Numerical Tests

The analytical results described above were validated against numerical simulations of the exact dynamics Eq. (6.1). Such numerical simulations were carried out also to rigorously assess the effect that other factors, such as network size and the density of the links, might have on the relative shrinkage $\langle \Delta Rg^2 \rangle$.

The results of tests performed on random networks, generated with rewiring $p = 0.7$, of sizes $N = 500$ masses and $N = 4000$ are displayed in Fig. 6.2. For

each of these sizes, we tested varying average coordination numbers $\rho_{av} = \frac{L}{2N}$ where L is the total number of links in the network.

As can be seen in Fig. 6.2, neither the size of the network nor the link densities have a major effect on the observed $\langle \Delta R g^2 \rangle$. On the other hand, there is a minor finite size effect that can be appreciated in Fig. 6.2 for large values of δ_{max}. The percentage deviation of the observed shrinkage from the theoretical predictions is about 2% at $\delta_{max} = 0.9$ for $N = 4000$, while it is about 5% for networks of $N = 500$ masses.

Overall, these numerical results confirm the theoretical prediction that the expected shrinkage is only influenced by amount of prestrain δ_{max}.

6.3.1 Role of network topology

In order to investigate the effect of network topology on the expected network shrinkage, several numerical simulations were performed. Firstly, the effect of small worldliness on the overall network shrinkage was studied via a series of tests on Watts-Strogatz networks with varying rewiring probability p. For each value of p, 50 tests were performed and then the overall shrinkage averaged as shown in Fig. 6.3. Each network was generated starting from a ring lattice of N nodes with $\rho_{av} = 3$ (which translates to average node degree $\langle k \rangle = 6$), and the links then rewired randomly with a probability p while avoiding self-loops and multiple links. From results displayed in Fig. 6.3 it can be seen that the variance of the shrinkage decreases as the rewiring p increases. The mean values are slightly higher (7%) than the expected value given by the theory for low rewiring p while this difference drops to 2% for high p. This is compatible with the finite size effect that was observed in Fig.6.2.

Similar tests were carried out for scale-free networks to understand whether structural properties of scale-free networks, such as the degree exponent, have an effect on the observed shrinkage distribution. To create the test networks, a random degree sequence was generated for $N = 2000$ nodes with a given degree exponent γ. Vertices or node degree is then assigned to the nodes from this degree sequence essentially creating stubs or half connections. The configuration model with hidden parameters was then used to connect the stubs avoiding self-loops and multiple links in order to create a connected network from the degree sequence [200] Fig. 6.4 shows that there is a small tendency for the shrinkage to decrease as the degree exponent γ increases. This again could be attributable to the small size of the networks

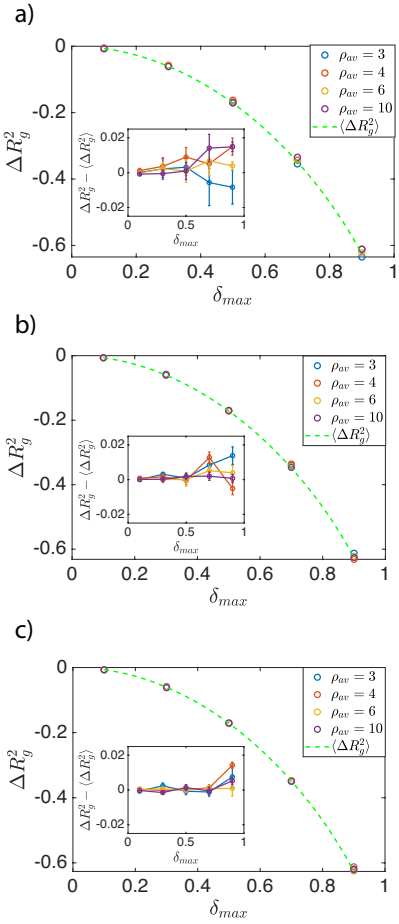

Figure 6.2: a) Variation of the relative shrinkage $\Delta Rg^2 < 0$ against the maximum prestrain δ_{max} for networks of $N = 500$ masses while b) and c) show similar results of tests done on $N = 2000$ and $N = 4000$ respectively. The dotted green line shows the expectation calculated using Eq. (6.12) and the solid lines refer to numerical simulations. Networks of different average coordination numbers, ρ_{av} are shown by colour. Each marker (dot) shows the mean of 6 trials with separate realisations of networks, generated according to the Watts-Strogatz (rewiring probability $p = 0.7$). The error bars represent the Standard Error. The inset shows the difference between the expected relative shrinkage and the shrinkage from the numerical simulations $\Delta Rg^2 - \langle \Delta Rg^2 \rangle$.

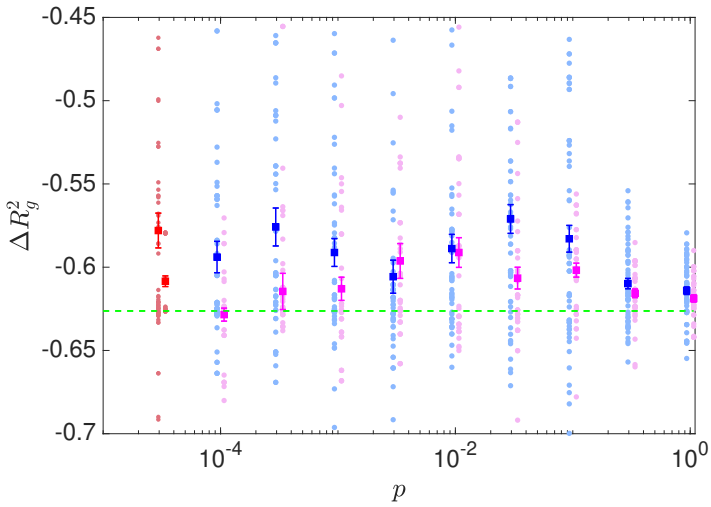

Figure 6.3: Distribution (mean and standard error) of relative shrinkage $\langle \Delta Rg^2 \rangle$ against the rewiring probability p of the generated Watts-Strogatz networks. 50 trials were tested for each rewiring probability by generating a new network of $N = 1000$ (shown in blue) and $N = 2000$ (shown in magenta). The prestrain level was set to the maximum $\delta_{max} = 0.9$ and the dotted green line is the expectation given by the theoretical analysis. The scatter of the data is shown underneath as dots of a paler colour, to show the overall distribution. The red points refer to tests done with rewiring $p = 0$ and have been added on to the same axis for comparison for both $N = 1000$ (red left-hand side marker) and $N = 2000$ (red right-hand side marker).

tested not being able to form large enough hubs to see the effect of the exponent or the degree 'cutoff' effect in such networks.

The last class of networks tested are 'End-Hub' networks. These are symmetric networks that have an equal number of hubs on either end of the 1D network, and are designed to maximise the link distances. For example, if a network of $N = 8$ nodes has two hubs with $H = 1$ hub on either end, then the links are such that each hub links to half the nodes of network. This is sketched in Fig. 6.5 a) for reference. Further tests were done to see the effect of rewiring these networks in a fashion similar to that done with the Watts-Strogatz networks. Once again, theoretical predictions match numerical results within 4%. The comparison between the results shown in Fig. 6.5 b) and those in Fig. 6.3 highlights that, while the Watts-Strogatz have a mean $\langle \Delta Rg^2 \rangle$ that starts above the theoretical predictions and gets closer

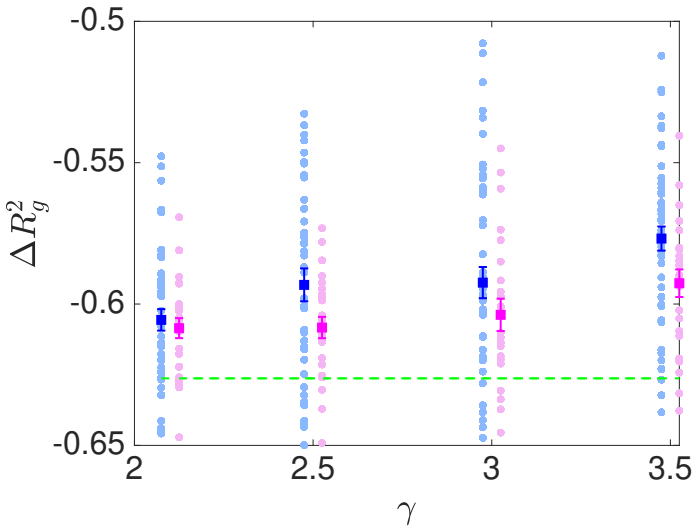

Figure 6.4: Distribution (mean and standard Error) of relative shrinkage $\langle \Delta R g^2 \rangle$ against the degree exponent γ of the generated scale-free networks. 50 trials were tested for each γ by generating a new realisation of a network of $N = 2000$ for each trail. The prestrain strength was set to the maximum $\delta_{max} = 0.9$ and dotted green line is the expectation given by the theory. $N = 2000$ is shown in magenta and the results of $N = 1000$ is shown in blue. The pale dots show the scatter of the data.

with increasing randomness, the opposite is true for End-Hub networks. The reason for this is believed to be due to the link lengths. The regular lattice starts from the shortest possible lengths for any given number of links while End-Hubs have the longest links. As the randomness increases with rewiring probability we see that both of these trends converge to roughly the same value for $p = 1$.

6.4 Discussion

We proposed and studied a framework for inducing contraction in 1D elastic networks using a random, zero-mean, prestrain. We have analysed the expected behaviour of such systems within the given bounds and shown that these networks will always contract with the applied prestrain and, furthermore, that for large networks the amount of contraction is only influenced

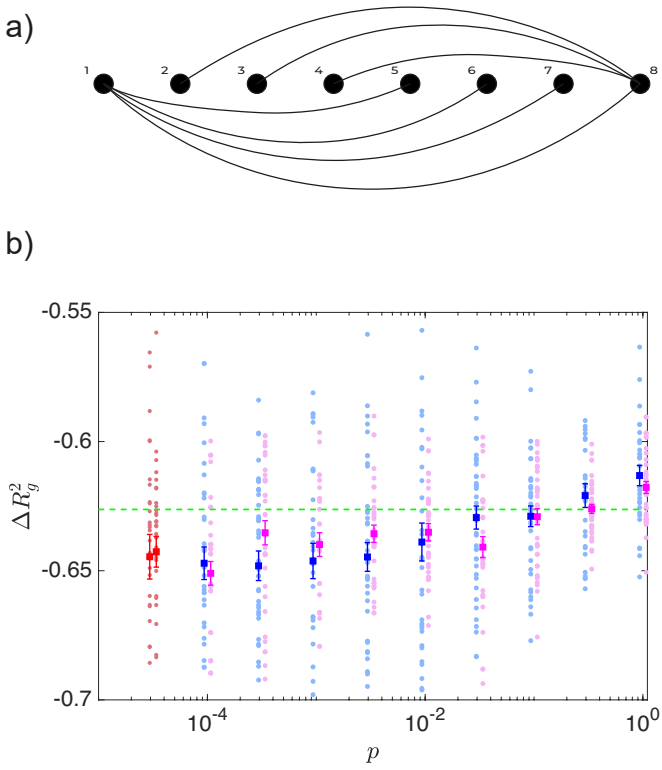

Figure 6.5: a) Sketch of an End-Hub network of size $N = 8$ with $H = 1$ hub on either side. b) Distribution (mean and standard Error) of relative shrinkage $\langle \Delta Rg^2 \rangle$ against the rewiring probability of the generated End-Hub networks with $H = 3$ hubs per side of the network. 35 trials were tested for each rewiring probability by generating a new network of $N = 1000$ nodes (shown in blue) and 16 trials have been tested for $N = 2000$ (shown in magenta). The prestrain strength was set close to the maximum $\delta_{max} = 0.9$ and dotted green line is the expectation given by the theory. Pale colour dots show the scatter of the data.

by the magnitude of the perturbations. Through numerical testing, we have found the theoretical predictions of the analysis to be robust with networks as small as $N = 500$ nodes. However, minor fluctuations were observed around the expected value at high prestrain strengths. This can be attributed to finite size effects, as those fluctuations vanish for larger networks of $N = 2000$

or higher. In the small N region where fluctuations were significant, we investigated the role played by the topology of the connecting network by numerically testing Watts-Strogatz, scale-free and End-Hub networks. It was found that having order and regularity in the links, as in the case of Watts-Strogatz an End-Hubs with low rewiring probability p, can influence the direction of the observed fluctuations. This can be attributed to the average link length, being shorter (Watts-Strogatz) or longer (End-Hubs) than if the network were completely random. At high p both types of topology converge to similar values of shrinkage.

Conclusions

The world around is filled with fascinating complexity that arises as a result of numerous elements interacting via an intricate web of connections. The standard assumptions that guide many conceptual and quantitative frameworks do not often hold for many complex biological, physical, and social systems. Ranging in size, shape and function, processes from the protein-protein interactions inside cells to the spreading of diseases or opinions shaping presidential elections can all be studied under the broad umbrella of complex networks. This versatility of network science in being able to quantitatively describe a wide plethora of complex phenomena across diverse fields has led to a rapid development and interest despite how relatively new it as a discipline in itself. The study of complex networks, not only from an abstract theoretical lens but also as a powerful modelling tool that describes complex macroscopic behaviour from the interactions of microscopic elements, remains an active and intriguing field of exploration.

The aim of this thesis was to inform our understanding of the interplay between the embedding structure of complex dynamical systems and their collective behaviour by focusing the inverse problem. Large and complicated systems in particular are difficult to probe to the fullest extent, i.e., with perfect information on all the actors of the system. They can often only be studied through limited measurements; be it the observation of a limited subset of nodes (microscopic) or the observation of the collective output (macroscopic) but with limited resolution on individual entities. While network science as a whole is a testament to the importance of being able to characterize and distinguish one topology from the other, in many cases of interest one has to infer this information from limited measurements. A framework for inversion has been proposed that unveils structural information about the architecture of the underlying network support of the scrutinized system, namely the distribution of degrees of the nodes of the system. The

degree distribution reveals meaningful information in characterizing various network topologies as the characteristic signatures of the commonly encountered, and widely studied, types of networks are therein displayed. This framework is successfully validated for a simple reactive-walker model hosted on a symmetric network support in a purely synthetic context. Following this, the inversion protocol has been generalized and extended to reveal more than just the degree distribution using spiking neuronal model on a directed network. This extended framework upon successful validation *in sillico* has been applied to *in vivo* cortical activity data from two different species of animals to reveal physiologically and biologically relevant insights. Microscopic fluctuations are often absorbed into average effects at the macroscopic level. The last chapter analysed a different class of network models, namely Elastic Network Models, where an interesting shrinking effect was studied by theoretical predictions of its average behaviour. Markedly, the inspected effect proved to be unresponsive to topological changes.

Let us summarize the main findings and highlight future areas of investigation. In Chapter 2 a procedure that builds on the celebrated Heterogeneous Mean Field (HMF) approximations to recover structural information is developed and tested on synthetic simulations of reactive-walkers. The method samples the dynamics of the microscopic agents that hop from node to node exploring the network, while also being subject to local non-linear reactions terms at the nodes. This non-linearity, whose relative importance can be tuned at will, enables the recovery of the distribution of connectivities of the entire network through a sequence of measurements performed on just one arbitrary observation node. This goal was achieved by exploiting the organisation in classes of the ensuing dynamical equilibrium and making explicit use of the HMF approximation to recast the dynamics into a form that is defined through classes of nodes differentiated by their connectivities. Due to the reliance of the method on the ability to sample multiple dynamical equilibria, a variant of the scheme that achieves this by injecting material into the network (at modulable rates through a subset of nodes) was also successfully tested. When the network is scrutinized by modulating the strength of injection of the sources, the size of the network could be estimated alongside the degree distribution of the undirected network support.

The next two Chapters, 3 and 4, introduced and presented two different analyses of the same neurological data set. The wide-field calcium imag-

ing data of cortical activity from transgenic mice with genetically encoded calcium indicators is introduced in Chapter 3. The brain activity of the animals are recorded before, during and after a stroke and while undergoing rehabilitation. In Chapter 3 an overview of a spatial-temporal analysis that capture the progression stroke recovery through three new biomarkers that identify the features of movement-evoked global activation patterns: duration, smoothness and angle of propagation of events. It was found that the stroke condition slows down the propagation patterns and makes them patterns more irregular.

While in Chapter 4, a similar signature of the effects of the stroke, and in turn the recovery of the animals were found through the application of a generalized version of the inversion protocol from Chapter 2 to this data. Reconstructing structural and functional information from brain activity represents a topic of outstanding importance, which can in principle trigger applied and fundamental fallout. A more complicated Leaky-Integrate and Fire (LIF) spiking neuronal model with short term plasticity was used here. Unlike the reactive-walkers which were evolving on an undirected network, LIF neurons were coupled via a directed support. The method builds on the Leaky-Integrate and Fire (LIF) model which we modified by the inclusion of quenched disorder, in the assigned individual currents. The imposed degree of heterogeneity in the currents yields non-trivial aperiodic patterns with variations in intensity, which resemble that recorded *in vivo*.

The inverse protocol was extended to recover both structural and functional information from measurements of the global field, namely the in-degree distribution of the embedding network and the distribution of currents that dictate the neuron's inherent dynamics. This was achieved making use of the HMF approximations to redefine a reduced version of the LIF model based on classes decorated with joint values of connectivities and currents. A known global field was used as the driver of the reduced model in self-consistent minimization scheme which acts through the tuning of the two unknown distributions, i.e., essentially fitting the reduced HMF model to the data. The inversion scheme was used successfully to recover both distributions simultaneously in synthetic tests that were matched, by design, to the temporal fidelity of the mice data set. Following this successful *in silico* validation the scheme was applied to the wide-field cortical imaging data made possible through spike detection and a novel filtering of the detected spike through a reduced version of the model that bypasses the network.

This filtering resulted in the ideal input for the reconstruction scheme, the global field. The analysis found that although there was not any noteworthy changes in the brain's dense connectivity distribution, a significant change was was observed in the recovered distributions of currents as the stroke and eventual recovery progressed. The initially peaked distribution flattened and formed a heavy right tail (alluding to more excitable neurons) after stroke in line with the post stroke hyperexcitability in the penumbra region. This effect was quantified through the skewness and could have the potential to be developed into a non-invasive monitoring framework for recovery from brain injuries like stroke in a future perspective.

The model above only accounts for excitatory neurons and hence taking this as a starting point, the next logical extension was developed in Chapter 5. The reconstruction scheme was further generalized so as to account for the simultaneous presence of both excitatory and inhibitory neurons, while still dealing with the effect of the current heterogeneity. The dynamics of the examined multi-species LIF model is recast in a simplified framework, by grouping together neurons that belong to the same class (inhibitory vs. excitatory), while sharing the similar currents and in-degree. The *a priori* unknown distributions of the incoming degrees for, respectively, excitatory and inhibitory neurons, as well as the distribution of the imposed currents are recovered in a comparable iterative minimization scheme to that proposed in Chapter 4. Upon synthetic validation, the method was then applied to whole-brain functional data resulting from light-sheet calcium imaging of a zebrafish larva. Remarkably, the cross-correlation maps produced, show a high grade of clusterization, which aligns with the anatomical boundaries of multiple brain regions identified using zebrafish brain atlases [156; 157]. A power law distribution of the in-coming connectivity of excitatory neurons is found, which is only modestly affected by the imposed fraction of inhibitors, that was introduced to account for the inseparability of two species dependant global fields. Through local degree distributions that correspond to the brain regions, two groups were identified, one characterized by higher connections and lower excitability and the other with lower connections and higher excitability. The reconstruction scheme reflects the specific functional connectivity of the larval brain during spontaneous activity under the restrained experimental setting and the recovered distributions are compatible with the various possible actions or experiences of the setting. This opens up the possibility to study the animal's reactions to many different setting and stimuli.

An interesting future extension would be to study how the functional connectivity of the animal changes when subjected to various sensory inputs, for instance, the presence of a predator in the visual field.

All the variants and refinements of the reconstruction scheme discussed in this thesis rely on the HMF reformulations of the dynamics. However, the existence of possible correlations between individual connectivities (in Chapter 2) and associated neurons' currents (in Chapters 4 and 5) cannot be resolved within the proposed approach and defines an interesting target for future investigations. Moreover, it would be also interesting to elaborate on possible generalization of the method so as to account for corrections beyond the simplified HMF.

Lastly, another interesting phenomenon on a different class of networks (Elastic Network Models or ENMs) is studied similarly by looking at the mean effects. A framework was proposed and studied for inducing contractions in 1D elastic networks using a zero-mean, noise-like prestrain. Interestingly, numerical simulation revealed that once prestrained all networks invariably shrunk within the bounds of the testing. It was found the magnitude of the shrinkage, although invariant to topological changes, was tunable by modulating the strength (or variance) of the prestrain. Networks that can execute a desired function (shrinkage) in mechanistic fashion are also useful in modelling the dynamics of active networks such as the protein machinery in cells. Furthermore, this framework opens up the possibility for a new perspective in consensus reaching methods where the goal is to generate agreement amongst the microscopic participants on certain parameters of interest which is relevant for instance in group decision making, smart power grids, swarming control and robotics. It should also be remarked that although the role of topology is limited in the 1D case analysed here, it could have a more prominent role in the behaviour of networks in higher dimensions. Furthermore, the effect of fixing springs constants rather than the stiffness would be very different to the contracting networks studied here, and could form the basis of a different type of noise-driven machinery. These will be interesting avenues of inquiry that have been left for future work.

To sum up, the thesis achieves its aim of contributing towards our understanding of the interlinked relationship between structure and function, through the successful development of many novel ideas that have the main theme of solving the inverse problem; recovering structure from function.

Appendix A: Supplementary information for Chapters 3 and 4

A.1 Materials and methods

A.1.1 Experimental design

The experiments were carried out by collaborators at the LENS - European Laboratory for Non-Linear Spectroscopy. Please refer to the referred manuscript in Publications for more details. The experimental details are presented here to compliment the analysis presented in the main body.

Mice

All experimental procedures were performed in accordance with directive 2010/63/EU on the protection of animals used for scientific purposes and approved by the Italian Minister of Health, authorization n.183/2016-PR. Mice were housed in clear plastic cages under a 12 h light/dark cycle and were given ad libitum access to water and food. We used a transgenic mouse line (C57BL/6J-Tg(Thy1GCaMP6f)GP5.17Dkim/J, referred to as GCaMP6f mice) expressing a genetically-encoded fluorescent calcium indicator under the control of the Thy-1 promoter. Mice were identified by earmarks and numbered accordingly. Animals were randomly assigned to 3 experimental groups: control, robot and rehab (rehab mice are a subgroup of those used in [109]). Each group contained comparable numbers of male and female mice (weighing approximately 25g). The age of mice was consistent

between the groups (ranging from 3 to 4 month).

Photothrombotic Stroke Induction & Optical Window

All surgical procedures were performed under Isoflurane anesthesia (3% induction, 1.5% maintenence, in 1.5L/min oxygen). The animals (apart from the control mice) were placed into a stereotaxic apparatus (Stoelting, Wheat Lane, Wood Dale, IL 60191) and, after removing the skin over the skull and the periosteum, the primary motor cortex (M1) was identified (stereotaxic coordinates 1,75 lateral, 0.5 anterior to bregma). Five minutes after intraperitoneal injection of Rose Bengal (0.2 ml, 10 mg/ml solution in Phosphate Buffer Saline (PBS); Sigma Aldrich, St. Louis, Missouri, USA), white light from an LED lamp (CL 6000 LED, Carl Zeiss Microscopy, Oberkochen, Germany) was focused with a 20X objective (EC Plan Neofluar NA 0.5, Carl Zeiss Microscopy, Oberkochen, Germany) and used to illuminate the M1 for 15 min to induce unilateral stroke in the right hemisphere. We choose a photothrombotic stroke model as a non invasive technique to induce a targeted ischemic stroke highly reproducible. Previous results confirmed that lesion volume were comparable between groups[123]. In this previous set of experiment the behavioural evaluation highlighted that while all groups showed a deficit of motor performances 2 days after photothrombosis, only the combined rehabilitative treatment induced the recovery of forelimb functionality. Botulinum Neurotoxin E (BoNT/E) injections in rehab mice were performed during the same surgical session of the photothrombotic lesions. A dental drill was used to create a small craniotomy over M1 of the healthy hemisphere (ML: -1.75; RC:+0.5). Then 500 nL of BoNT/E were delivered in two separate injections. A cover glass and an aluminum headpost were attached to the intact skull using transparent dental cement (Super Bond, C&S). Afterwards, the animals were placed in their cages until full recovery. In a previous study Spalletti and colleagues [123] characterized the effects of BoNT/E in naive mice. They first evaluated the diffusion of the toxin activity in the cortex by performing immunostaining 2 days after the injection. This analysis revealed an evident cleavage of SNAP-25 protein along all cortical layers. Then to characterize the duration of BoNT/E expression they collected tissue samples at different time points after surgery. Western-blot analysis showed a persistence of cleaved snap-25 for at least 10 days after injection. Indeed the evaluation of mice motor performances via gridwalk and Schallert test revealed a transient deficit in contralateral forelimb perfor-

mance, significant 2 days post injection. Performance returned to baseline on day 9. Spalletti and collaborators further investigated the effect of contralesional BoNT/E injection in a photothrombotic stroke model. Behavioural investigation revealed a slight improvement in general forelimb motor test, but this effect was not stable throughout the observation period.

Motor Training Protocol on the M-Platform

Before the first imaging session each mouse was allowed to become accustomed to the apparatus. The animals were trained by means of the M-Platform, which is a robotic system that encourages mice to perform a retraction movement of their left forelimb [109; 124]. The task consisted of up to 15 cycles of passive extension of the affected forelimb followed by its active retraction triggered by an acoustic cue. The time course of one individual training cycle is detailed in Table 1. All groups performed at least four weeks (20 sessions) of daily sessions; in addition, 5 out of 8 robot mice were also recorded for one week before stroke (5 sessions). The M-Platform was designed to allow mice in all conditions (before stroke, right after stroke, and during the weeks under all treatments) to easily perform the motor task from the very first session by applying similar forces. For the same reason, this robotic device is not suitable to evaluate post-stroke functional impairment.

0	linear actuator positions forelimb at 10 mm from resting position (passive maximum extension)
1	forelimb remains in extended position (0.50s)
2	acoustic tone (1.00V, 0.50s) signals beginning of task
3	mouse is allowed to perform task of pulling handle back to resting position
4	different acoustic tone (3.00V, 1.00s) marks end of task
5	waiting time before reward supply (0.50s)
6	supply of liquid reward for successful execution of task (0.30s)
7	waiting time (2.00s) to allow mouse to drink reward before next task

Table 1: Time course of training cylce. Each line corresponds to a different value of the status variable.

Wide-Field Fluorescence Microscopy

The custom-made wide-field imaging setup [201; 202] was equipped with a 505 nm LED (M505L3 Thorlabs, New Jersey, United States) light was deflected by a dichroic filter (DC FF 495-DI02 Semrock, Rochester, New York USA) on the objective (2.5x EC Plan Neofluar, NA 0.085, Carl Zeiss Microscopy, Oberkochen, Germany). Then a 20x objective (LD Plan Neofluar, 20x/0.4 M27, Carl Zeiss Microscopy, Oberkochen, Germany) was used to demagnify the image onto a high-speed complementary metal-oxide semiconductor (CMOS) sensor (OrcaFLASH 4.0, Hamamatsu Photonics, NJ, USA). The fluorescence signal was selected by a band pass filter (525/50 Semrock, Rochester, New York USA) and images (100 x 100 pixels, pixel size 60 μm) were acquired at 25 Hz. Accordingly, signals from every pixel reflect the activity of hundreds if not thousands of neurons.

A.2 Statistical Tests

Each propagation indicator, event type and condition (healthy, Fig. 3.3, acute phase, Fig. 3.4, and rehabilitation, Fig. 3.5) were all tested with different models. The unit observations considered were the indicator averages of all events (of a specific type) in a single session/day. Therefore, having 4 weeks of training, each animal had at most 20 measurements per indicator and event type. Intra-subject correlation were considered through the implementation of mixed-effect models. Circular distributions were assumed for tests on the propagation angle. The analyses in Fig. 3.3 were carried out considering healthy mice only during all 4 weeks of training (pre-stroke week of robots is not included). The acute phase analyses in Fig. 3.4 focused on the first week of training for the healthy mice (including the pre-stroke week of robots) and the first post-stroke week of robot group. Finally, the rehabilitation comparisons in Fig. 3.5 looked at all groups from the second to the fourth week of training.
Mixed-effect models, for duration and smoothness indicators, are implemented in the *R* software with the *lme4* library [203]. All models were initialised with all possible fixed covariates and interactions and with all random parameters (subject intercept variance, daily slope variance and intercept-slope covariance). Subsequently, a backward selection with likelihood-ratio tests was carried out in order to select a parsimonious feasible model without removing relevant effects that could decrease the *type I error* rate and

increase the statistical power [204]. Once the model parameters had been selected, differences between the estimates of interest were assessed with the *lmerTest* library [205] and Holm-Bonferroni correction was used to correct the multiple testing bias. Moreover, normality of residuals assumption was assessed with the Kolmogorov-Smirnov test, while homogeneity of variance for fixed effects without related random slopes was evaluated with the Breusch-Pagan test. If normality assumption did not hold, a Box-Cox transform of the dependent variable [206] was carried out. If the Breusch-Pagan test revealed departure from homogeneity of variance, we analyzed which comparisons had a significant difference in variance, again correcting the p-values with the Holm-Bonferroni method.
Differences in circular variance for the propagation angle were instead tested with multiple Bartlett tests [*circular* library in *R*, 207]. Again, the Holm-Bonferroni correction was adopted to correct the multiple comparison bias. Assumption of Von-Mises distribution for both groups under comparison was assessed with the Watson test [208].

A.2.1 Signal processing and data analysis

Preprocessing

Data acquired during each recording session (one mouse, one day, see Fig. 3.1b) was processed offline using custom routines implemented in Python (Python Software Foundation) and Matlab (MathWorks). Each such dataset consisted of up to 15 cycles of active retraction movements on a slide triggered by passively actuated contralesional forelimb extensions. To ensure the consistency of the field of view across sessions and across mice, each frame of the fluorescence data was offline registered by aligning each frame to two reference points (corresponding to bregma and lambda) that were previously marked on the glass window during the surgery procedure. For the 2D fluorescence data, masking the region of interest and spatial downsampling by a factor 3 for both rows and columns resulted in calcium activity matrices of 12 x 21 pixels. Spatial average over all pixels yielded the mean calcium activity. In parallel, the force applied to the slide by the mouse and the discrete status of the slide were recorded. Using samplings with a time step of 40 ms and acquisition times of up to 400 seconds this yielded recordings with at most 10000 data points. The calcium traces were detrended via subtraction of a moving average of order 75 (three seconds) and, in order to

yield a better time resolution, upsampled by a factor 20.

Event detection

Next, within all of these traces we identified the times of the most relevant discrete events. For the status (Fig. 3.2a) we marked the transition from level 3 to level 4 which corresponds to the completion of the forelimb retraction by the active movement of the mouse upon which the animal received its reward (reward pulling event). For the force (Fig. 3.2b), the mean calcium (Fig. 3.2c) and the individual calcium traces of all the pixels the events are the high-amplitude peaks that can easily be recognised. As event times we used the upwards crossings of a threshold T which in each of these cases was defined in a data-adaptive manner according to $T = mean(x) + t * std(x)$. The free parameter t was set to 1.5 for the force and 1.7 for all the calcium traces. In the slower calcium traces, in order to avoid double detections due to noise, we discarded all events that succeeded the previous event by less than a minimum inter-event interval of 25 data points (one second).

SPIKE-order

The events (from now on called spikes) of all the pixels can be represented best in a rasterplot like the one shown in Fig. 3.2d. The next important step was to identify the global events that correspond to the events of the mean calcium trace. To this aim, we used the cSPIKE-implementation [209] of the SPIKE-order approach recently proposed in [122] (for detailed definitions of all the underlying quantities please refer to the Appendix A.3). The original proposal was designed for rather clean data with well-defined global events. These conditions hold for most of our datasets as well, however, we added a few tailor-made denoising steps that addressed the rare instances of increased noisiness that we observed in some of the datasets.

The procedure consisted of six steps: in an initial denoising step, we filtered out all spikes of individual pixels that were not within 1 second of a mean calcium event and thus were certainly not part of global events. Secondly, we applied the coincidence detection first introduced for the bivariate measure *event synchronization* [127]. This criterion paired spikes in such a way that every spike was matched with at most one spike in each of the other pixels. Here we combined the original adaptive approach with a maximum allowed distance between spikes of 2.5 seconds. Next, we used the symmet-

ric and multivariate measure SPIKE-Synchronization C [128] to quantify for each spike the fraction of other pixels for whom a matching spike could be found. By setting a threshold value $C_{thr} = 0.75$ we only took into account spikes which were coincident with spikes in at least three quarters of the other pixels, all other spikes were filtered out as background noise.

In a fourth step, we applied the SPIKE-order D [122] which evaluates the temporal order of the spikes by quantifying for each spike the net-fraction of spikes of other pixels this spike is leading (positive value) or following (negative value). Based on the time profile we identified start and end spikes of global events by tracking the jumps from a negative local minimum (last spike of previous event) to a positive local maximum (first spike of current event). In one further denoising step we discarded split events and eliminated outlier spikes by using a maximum distance between consecutive spikes of 0.15 seconds and thereby kept only continuous global events. The final step used in the visualisation of the spike trains in Fig. 3.2d involved the Synfire Indicator [122], a scalar measure which quantifies to what degree the spatiotemporal propagation patterns of the global events are consistent with each other. Optimisation of this indicator was used to sort the spike trains / pixels from overall leader to overall follower. Here, overall means that we take into account all global events at the same time. The result is that the first spike trains contain mostly leading spikes, whereas the last spike trains consist largely of trailing spikes.

Categorisation of events

Next, we divided the global events into several types using the following three-level categorisation scheme (the corresponding branching structure is shown in Section Methods): First, we separated all the global events that are not associated with a force event (non-Force, **nF**). For this we demanded that there is no force event in the interval [1 second before, 0.75 seconds after] the matching calcium event. The window was slightly asymmetric to account for the fact that typically Force were observed a bit earlier than mean calcium events. The remaining Force events (**F**) were further subdivided into events that occur during the passive extension of the arm by the slide (Passive, **Pass**) and events that occur outside that window (Active, **Act**). In the passive events the mouse applied force to resist the forelimb extension movement of the robot, whereas the active events were the ones where the force was applied during an active retraction movement (when the status variable was set

to 3, i.e. between the Go cue and the completion of the task). Finally, among the active events we distinguished between events which were not completed and thus not rewarded (non-Reward Pulling, **nRP**) and events which lead to a completion of the forelimb retraction and therefore were rewarded with milk (Reward Pulling, **RP**). The categorisation criterion was the occurrence of a transition from status 3 to status 4 within [0.75 seconds before, 0.75 seconds after] a calcium event. This window was symmetric, since the observed temporal distribution of status events was symmetric with respect to the mean calcium events.

Three propagation indicators: Duration, Angle, Smoothness

For all global events, the event time was defined as the average time of all the spikes within the event and our first propagation indicator, the event duration, was defined as time from the first to the last spike of the event. To calculate the other two propagation indicators, angle and smoothness, we first generated the propagation matrix by mapping the color-coded relative order of the spikes onto the pixels of the 2D-recording plane (compare Fig. 3.2f). Next, we applied singular value decomposition (SVD, [129]) which searches for spatial patterns by decomposing the propagation matrix P into three simple transformations: a rotation U, a scaling Σ along the rotated coordinate axes and a second rotation V^T.

The rotations U and V^T are orthonormal matrices and Σ is a diagonal matrix containing in its diagonal the singular values σ_i of P. By backprojecting the sorted singular values one at a time

$$\Sigma_1 = \begin{bmatrix} \sigma_1 & & \\ & 0 & \\ & & \ddots \end{bmatrix} \qquad \Sigma_2 = \begin{bmatrix} 0 & & \\ & \sigma_2 & \\ & & \ddots \end{bmatrix}$$

we could obtain various projections of the original propagation matrix

$$P_1 = U\Sigma_1 V^T \qquad P_2 = U\Sigma_2 V^T.$$

The mean gradients with respect to column (c) and row (r) increments of the first two projections were calculated as

$$\begin{cases} g_1^c = \mathbb{E}(-\frac{\partial P_1}{\partial c}) \\ g_1^r = \mathbb{E}(-\frac{\partial P_1}{\partial r}) \end{cases} \qquad \begin{cases} g_2^c = \mathbb{E}(-\frac{\partial P_2}{\partial c}) \\ g_2^r = \mathbb{E}(-\frac{\partial P_2}{\partial r}) \end{cases}$$

with $\mathbb{E}$ denoting the average across pixels while the sign (-) is defined by the directionality in the matrix P going from leader (+1) to follower (-1). The main propagation directions, along the column and row directions,

$$\begin{cases} v^c = \sigma_1 g_1^c + \sigma_2 g_2^c \\ v^r = \sigma_1 g_1^r + \sigma_2 g_2^r \end{cases}$$

were calculated from the weighted average of the mean gradients of the first two projections, with the singular values as weights. Our second propagation indicator, the angle

$$\alpha = \arctan\left(\frac{v^c}{v^r}\right)$$

was defined relative to the horizontal axis.

Finally, our third propagation indicator, the smoothness S, quantified how well the second order approximation, the weighted sum of the projections of only the first two singular values, captures the full spatiotemporal pattern obtained by considering all singular values σ_i. Smoothness is defined as the relative weight of the first two approximations

$$S = \frac{\sigma_1^2 + \sigma_2^2}{\sum_i \sigma_i^2}. \tag{15}$$

A.3 SPIKE-order method

Here we present the more detailed definitions of the SPIKE-order approach, the central method of our study that we use to identify global events and to track the propagation patterns within these events by sorting the spikes from leader to follower.

A.3.1 Adaptive Coincidence Detection

Analysing leader-follower relationships in a spike train set requires a criterion that determines which spikes should be compared against each other. Here we use the adaptive coincidence criterion first proposed in [127]. This coincidence detection is scale- and parameter-free since the maximum time lag $\tau_{ij}^{(m,n)}$ up to which two spikes $t_i^{(m)}$ and $t_j^{(n)}$ of spike trains $m, n = 1, ..., N$ (with N denoting the number of spike trains) are considered to be syn-

chronous is adapted to the local firing rates according to

$$\tau_{ij}^{(m,n)} = \min\{t_{i+1}^{(m)} - t_i^{(m)}, t_i^{(m)} - t_{i-1}^{(m)}, \\ t_{j+1}^{(n)} - t_j^{(n)}, t_j^{(n)} - t_{j-1}^{(n)}\}/2. \tag{16}$$

A.3.2 SPIKE-Synchronization

Following [128], we apply the adaptive coincidence criterion in a multivariate context by defining for each spike i of any spike train n and for each other spike train m a coincidence indicator

$$C_i^{(n,m)} = \begin{cases} 1 & \text{if } \min_j(|t_i^{(n)} - t_j^{(m)}|) < \tau_{ij}^{(n,m)} \\ 0 & \text{otherwise.} \end{cases} \tag{17}$$

which is either one or zero depending on whether this spike is part of a coincidence with a spike of spike train m or not. This results in an unambiguous spike matching since any spike can at most be coincident with one spike (the nearest one) in the other spike train.

Subsequently, for each spike of every spike train a normalised coincidence counter

$$C_i^{(n)} = \frac{1}{N-1} \sum_{m \neq n} C_i^{(n,m)} \tag{18}$$

is obtained by averaging over all $N-1$ bivariate coincidence indicators involving the spike train n.

In order to obtain a single multivariate SPIKE-Synchronization profile we pool the coincidence counters of all the spikes of every spike train:

$$\{C(t_k)\} = \bigcup_n \{C_{i(k)}^{(n(k))}\}, \tag{19}$$

where we map the spike train indices n and the spike indices i into a global spike index k denoted by the mapping $i(k)$ and $n(k)$.

With M denoting the total number of spikes in the pooled spike train, the average of this profile

$$S_C = \begin{cases} \frac{1}{M} \sum_{k=1}^{M} C(t_k) & \text{if } M > 0 \\ 1 & \text{otherwise} \end{cases} \tag{20}$$

yields SPIKE-Synchronization, the overall fraction of coincidences. It reaches one if and only if each spike in every spike train has one matching spike in all the other spike trains (or if there are no spikes at all), and it attains the value zero if and only if the spike trains do not contain any coincidences.

A.3.3 SPIKE-Order

While SPIKE-Synchronization is invariant to which of the two spikes within a coincidence is leading and which is following, the temporal order of the spikes is taken into account by the two indicators SPIKE-Order and Spike Train Order.

The bivariate anti-symmetric SPIKE-Order indicators

$$\begin{aligned} D_i^{(n,m)} &= C_i^{(n,m)} \cdot (t_{j'}^{(m)} - t_i^{(n)}) \\ D_{j'}^{(m,n)} &= C_{j'}^{(m,n)} \cdot (t_i^{(n)} - t_{j'}^{(m)}) = -D_i^{(n,m)}, \end{aligned} \tag{21}$$

where the index j' is defined from the minimum in Eq. 17 as $j' = \arg\min_j(|t_i^{(1)} - t_j^{(2)}|)$, assign to each spike either a 1 or a -1 depending on whether the respective spike is leading or following a coincident spike in the other spike train.

SPIKE-Order distinguishes leading and following spikes, and is thus used for color-coding the individual spikes on the leader to follower scale. But it can also be employed to sort the *spike trains* based on a pairwise analysis. For this we use the cumulative SPIKE-Order matrix

$$D^{(n,m)} = \sum_i D_i^{(n,m)}. \tag{22}$$

This anti-symmetric matrix sums up the orders of coincidences from the respective pair of spike trains only and quantifies how much spike train n is leading spike train m. Hence if $D^{(n,m)} > 0$ spike train n is leading m, while $D^{(n,m)} < 0$ means m is leading n. If the current spike train order is consistent with the synfire property (i.e., it displays consistent repetitions of the same global propagation pattern), we thus expect that $D^{(n,m)} > 0$ for $n < m$ and $D^{(n,m)} < 0$ for $n > m$. Therefore, we construct the overall SPIKE-Order as

$$D_< = \sum_{n<m} D^{(n,m)}, \tag{23}$$

i.e. the sum over the upper right tridiagonal part of the matrix $D^{(n,m)}$.

A.3.4 Synfire Indicator

After normalizing by the overall number of possible coincidences, we arrive at the definition of the Synfire Indicator:

$$F = \frac{2D_<}{(N-1)M}. \tag{24}$$

This measure quantifies to what degree coinciding spike pairs with correct order prevail over coinciding spike pairs with incorrect order, or in other words, to what extent the spike trains in their current order resemble a synfire pattern. Conversely, the maximization of the Synfire Indicator as a function of the spike train order within a set of spike trains can be used to sort spike trains from leader to follower such that the set comes as close as possible to a synfire pattern. Denoting the Synfire Indicator for any given spike train index permutation $\varphi(n)$ as F_φ, the optimal (**s**orted) order φ_s is the one resulting in the maximal overall Synfire Indicator $F_s = F_{\varphi_s}$:

$$\varphi_s : F_{\varphi_s} = \max_{\varphi}\{F_\varphi\} = F_s. \tag{25}$$

Whereas the Synfire Indicator F_φ for any spike train order φ is normalized between -1 and 1, the optimized Synfire Indicator F_s can only attain values between 0 and 1. A perfect synfire pattern results in $F_s = 1$, while sufficiently long Poisson spike trains without any synfire structure yield $F_s \approx 0$. For details on the optimisation procedure, please refer to [122].

A.3.5 Source Codes

SPIKE-Synchronization, SPIKE-Order and Spike Train Order are implemented in three publicly available software packages. Results in this study were obtained using cSPIKE [2] (Matlab command line with MEX-files). The Matlab-based graphical user interface SPIKY [3] [128], or the Python library PySpike [4] [210] are available as well.

[2] http://www.fi.isc.cnr.it/users/thomas.kreuz/Source-Code/cSPIKE.html
[3] http://www.fi.isc.cnr.it/users/thomas.kreuz/Source-Code/SPIKY.html
[4] http://www.pyspike.de

Publications

The research work presented in this thesis has lead to several publications in international journals which are summarized below. [5]

International Journals

I. Adam, D. Fanelli, T. Carletti, G. Innocenti, Reactive Explorers to Unravel Topology, THE EUROPEAN PHYSICAL JOURNAL. B, CONDENSED MATTER PHYSICS, 92, 2019, FloRe id: 2158/1164151

I. Adam, G. Cecchini, D. Fanelli, T. Kreuz, R. Livi, M. di Volo, A. Letizia, E Conti, A. Scaglione, L. Silvestri, F. Pavone, Inferring network structure and local dynamics from neuronal patterns with quenched disorder, CHAOS, SOLITONS FRACTALS, 140, 2020, FloRe id: 2158/1209935

Accepted Manuscripts

L. Chicchi, G. Cecchini, **I. Adam**, G. de Vito, R. Livi, F. Pavone, L. Silvestri, L. Turrini, F. Vanzi, D. Fanelli, Reconstruction Scheme for Excitatory and Inhibitory Dynamics with Quenched Disorder: Application to Zebrafish imaging, *accepted for publication in Journal of Computational Neuroscience*

Submitted Manuscripts

G. Cecchini, A. Scaglione, A. Letizia, C. Checcucci, E Conti, **I. Adam**, D. Fanelli, R. Livi, F. Pavone, T. Kreuz, Cortical Propagation as a Biomarker for Recovery After Stroke, *Manuscript submitted to PLOS Computational Biology*

[5] The author's bibliometric indices are the following: H-index = 1, total number of citations = 2 (source: Google Scholar on February 19, 2021).

I. Adam, F. Bagnoli, D. Fanelli, L. Mahadevan, P, Paoletti, Prestrain-induced contraction in 1D random elastic networks, *Manuscript being submitted to Physical Review Letters E*

Bibliography

[1] B. I. Henry, *Critical phenomena in natural sciences: Chaos, fractals, self-organization and disorder: Concepts and tools*, vol. 38 of *Springer Series in Synergetics*. Springer Berlin Heidelberg, 2001.

[2] I. Couzin, "Collective minds," *Nature*, vol. 445, no. 7129, p. 715, 2007.

[3] J. Buhl, D. J. Sumpter, I. D. Couzin, J. J. Hale, E. Despland, E. R. Miller, and S. J. Simpson, "From disorder to order in marching locusts," *Science*, vol. 312, no. 5778, pp. 1402–1406, 2006.

[4] D. T. Sumpter, *Collective animal behavior*. Princeton University Press, 2010.

[5] J. E. Herbert-Read, "Understanding how animal groups achieve coordinated movement," *Journal of Experimental Biology*, vol. 219, no. 19, pp. 2971–2983, 2016.

[6] M. Ballerini, N. Cabibbo, R. Candelier, A. Cavagna, E. Cisbani, I. Giardina, V. Lecomte, A. Orlandi, G. Parisi, A. Procaccini, M. Viale, and V. Zdravkovic, "Interaction ruling animal collective behavior depends on topological rather than metric distance: Evidence from a field study," *Proceedings of the National Academy of Sciences of the United States of America*, vol. 105, no. 4, pp. 1232–1237, 2008.

[7] H. Hamann, *Swarm Robotics: A Formal Approach*. Springer International Publishing, 2018.

[8] D. L. Stein and C. M. Newman, *Spin glasses and complexity*. 2013.

[9] Y. Holovatch, R. Kenna, and S. Thurner, "Complex systems: physics beyond physics," *European Journal of Physics*, vol. 38, no. 2, pp. 1–22, 2017.

[10] S. Battiston, J. D. Farmer, A. Flache, D. Garlaschelli, A. G. Haldane, H. Heesterbeek, C. Hommes, C. Jaeger, R. May, and M. Scheffer, "Complexity theory and financial regulation: Economic policy needs interdisciplinary

network analysis and behavioral modeling," *Science*, vol. 351, no. 6275, pp. 818–819, 2016.

[11] Steven L, "Regulating Complexity in Financial Markets," *Duke Public Law & Legal Theory Research Paper Series*, vol. 87, no. 3, pp. 1–70, 2009.

[12] M. Gell-Mann and D. Park, *The Quark and the Jaguar: Adventures in the Simple and the Complex*, vol. 65. Macmillan, 1997.

[13] D. W. McShea and R. N. Brandon, *Biology's first law: the tendency for diversity and complexity to increase in evolutionary systems*, vol. 48. University of Chicago Press, 2011.

[14] E. V. Koonin, "A non-adaptationist perspective on evolution of genomic complexity or the continued dethroning of man," *Cell Cycle*, vol. 3, no. 3, pp. 278–283, 2004.

[15] N. A. Heim, J. L. Payne, S. Finnegan, M. L. Knope, M. Kowalewski, S. K. Lyons, D. W. McShea, P. M. Novack-Gottshall, F. A. Smith, and S. C. Wang, "Hierarchical complexity and the size limits of life," *Proceedings of the Royal Society B: Biological Sciences*, vol. 284, no. 1857, p. 20171039, 2017.

[16] R. E. Goldstein, "Evolution of biological complexity," *Progress in Mathematical Physics*, vol. 60, no. 9, pp. 123–139, 2010.

[17] M. Newman, *Networks: An Introduction*. OUP Oxford, 2010.

[18] S. Boccaletti, V. Latora, Y. Moreno, M. Chavez, and D. U. Hwang, "Complex networks: Structure and dynamics," *Physics Reports*, vol. 424, no. 4-5, pp. 175–308, 2006.

[19] R. Albert and A. L. Barabási, "Statistical mechanics of complex networks," *Reviews of Modern Physics*, vol. 74, pp. 47–97, 1 2002.

[20] A. Barrat, M. Barthélemy, and A. Vespignani, *Dynamical processes on complex networks*. Cambridge: CUP, 2008.

[21] G. Caldarelli, *Scale-Free Networks: Complex Webs in Nature and Technology*, vol. 9780199211. 2010.

[22] J. D. Noh and H. Rieger, "Random Walks on Complex Networks," *Physical Review Letters*, vol. 92, p. 118701, 3 2004.

[23] R. Sinatra, J. Gómez-Gardeñes, R. Lambiotte, V. Nicosia, and V. Latora, "Maximal-entropy random walks in complex networks with limited information," *Physical Review E - Statistical, Nonlinear, and Soft Matter Physics*, vol. 83, p. 30103, 3 2011.

[24] V. Nicosia, F. Bagnoli, and V. Latora, "Impact of network structure on a model of diffusion and competitive interaction," *Epl*, vol. 94, p. 68009, 6 2011.

[25] N. Masuda, M. A. Porter, and R. Lambiotte, "Random walks and diffusion on networks," *Physics Reports*, vol. 716-717, pp. 1–58, 2017.

[26] S. Manfredi, E. Di Tucci, and V. Latora, "Mobility and Congestion in Dynamical Multilayer Networks with Finite Storage Capacity," *Physical Review Letters*, vol. 120, p. 68301, 2 2018.

[27] V. Latora, V. Nicosia, and G. Russo, *Complex Networks: Principles, Methods and Applications*. Complex Networks: Principles, Methods and Applications, Cambridge University Press, 2017.

[28] J. F. Fan, J. Meng, X. S. Chen, Y. Ashkenazy, and S. Havlin, "Network approaches to climate science," *Science China: Physics, Mechanics and Astronomy*, vol. 60, no. 1, p. 10531, 2017.

[29] M. Becker, M. Karpytchev, M. Marcos, S. Jevrejeva, and S. Lennartz-Sassinek, "Do climate models reproduce complexity of observed sea level changes?," *Geophysical Research Letters*, vol. 43, no. 10, pp. 5176–5184, 2016.

[30] K. T. Eames and J. M. Read, "Networks in epidemiology," *Lecture Notes in Computer Science (including subseries Lecture Notes in Artificial Intelligence and Lecture Notes in Bioinformatics)*, vol. 5151 LNCS, pp. 79–90, 2008.

[31] M. Woodward, *Epidemiology: Study design and data analysis, third edition*. Chapman & Hall/CRC Texts in Statistical Science, Taylor & Francis, 2013.

[32] KaranPatel, "Incremental Journey for World Wide Web: Introduced with Web 1.0 to Recent Web 5.0 â A Survey Paper," in *International Journal of Advanced Research in Computer Science and Software Engineering*, vol. 3, pp. 410–417, 2013.

[33] G. Ghoshal, G. Mangioni, R. Menezes, and J. Poncela-Casanovas, "Social system as complex networks," *Social Network Analysis and Mining*, vol. 4, no. 1, pp. 1–2, 2014.

[34] S. V. Albrecht and P. Stone, "Autonomous agents modelling other agents: A comprehensive survey and open problems," *Artificial Intelligence*, vol. 258, pp. 66–95, 2018.

[35] N. Dhanda, S. S. Datta, and M. Dhanda, *Machine Learning Algorithms*. Packt Publishing, 2019.

[36] A. M. Andrew, *Information Theory, Inference, and Learning Algorithms*, vol. 33. Cambridge University Press, 2004.

[37] G. Caldarelli and A. Vespignani, *Large Scale Structure and Dynamics of Complex Networks*. Complex systems and interdisciplinary science, World Scientific, 2007.

[38] Y. Bar-Yam, *Dynamics of complex systems: Introduction*. CRC Press, 2003.

[39] V. G. Ivancevic and T. T. Ivancevic, *Geometrical dynamics of complex systems: a unified modelling approach to ...* Intelligent Systems, Control and Automation: Science and Engineering, Springer Netherlands, 2006.

[40] A. M. Turing, "The chemical basis of morphogenesis," *Bulletin of Mathematical Biology*, vol. 52, no. 1-2, pp. 153–197, 1990.

[41] J. Miyazaki, "Belousov-Zhabotinsky Reaction," in *Pattern Formations and Oscillatory Phenomena* (S. Kinoshita, ed.), pp. 61–83, Boston: Elsevier, 2013.

[42] G. Cencetti, F. Battiston, D. Fanelli, and V. Latora, "Reactive random walkers on complex networks," *Physical Review E*, vol. 98, p. 52302, 11 2018.

[43] D. Fanelli and A. J. McKane, "Diffusion in a crowded environment," *Physical Review E - Statistical, Nonlinear, and Soft Matter Physics*, vol. 82, p. 21113, 8 2010.

[44] M. Galanti, D. Fanelli, S. D. Traytak, and F. Piazza, "Theory of diffusion-influenced reactions in complex geometries," *Physical Chemistry Chemical Physics*, vol. 18, no. 23, pp. 15950–15954, 2016.

[45] R. Muolo, M. Asllani, T. Carletti, and D. Fanelli, "Turing pattern formation on non-normal networks," *dim*, vol. 10, pp. 1–75.

[46] J. Halatek and E. Frey, "Rethinking pattern formation in reaction-diffusion systems," *Nature Physics*, vol. 14, no. 5, pp. 507–514, 2018.

[47] B. A. Grzybowski, *Chemistry in Motion: Reaction-Diffusion Systems for Micro- and Nanotechnology*. Wiley, 2009.

[48] H. L. Smith, *Book Review: Spatial ecology via reaction-diffusion equations*, vol. 41 of *Wiley Series in Mathematical & Computational Biology*. Wiley, 2004.

[49] R. Cherniha and V. Davydovych, *Nonlinear Reaction-Diffusion Systems: Conditional Symmetry, Exact Solutions and their Applications in Biology*. Lecture Notes in Mathematics, Springer International Publishing, 2017.

[50] S.-H. Yook, H. Jeong, and A.-L. Barabási, "Modeling the Internet's large-scale topology," *Proceedings of the National Academy of Sciences*, vol. 99, no. 21, pp. 13382–13386, 2002.

[51] M. C. González, C. A. Hidalgo, and A. L. Barabási, "Understanding individual human mobility patterns (Nature (2008) 453, (779-782))," *Nature*, vol. 458, no. 7235, p. 238, 2009.

[52] A. L. Barabási, *Network Science*. Cambridge University Press, 2016.

[53] A. L. Barabási and R. Albert, "Emergence of scaling in random networks," *The Structure and Dynamics of Networks*, vol. 9781400841, no. 5439, pp. 349–352, 1999.

[54] R. Milo, S. Shen-Orr, S. Itzkovitz, N. Kashtan, D. Chklovskii, and U. Alon, "Network motifs: Simple building blocks of complex networks," *Science*, vol. 298, pp. 824–827, 10 2002.

[55] Z. Yang, R. Algesheimer, and C. J. Tessone, "A comparative analysis of community detection algorithms on artificial networks," *Scientific Reports*, vol. 6, no. 1, p. 30750, 2016.

[56] D. J. Watts and S. H. Strogatz, "Collective dynamics of 'small-world' networks," *Nature*, vol. 393, no. 6684, pp. 440–442, 1998.

[57] P. ErdÓ§s and A. Rėnyi, "On random graphs I.," *Publicationes Mathematicae*, vol. 6, pp. 290–297, 1959.

[58] G. Cencetti, F. Bagnoli, G. Battistelli, L. Chisci, and D. Fanelli, "Spectral control for ecological stability," *European Physical Journal B*, vol. 91, no. 10, p. 264, 2018.

[59] G. Cencetti, F. Bagnoli, G. Battistelli, L. Chisci, and D. Fanelli, "Control of multidimensional systems on complex network," *PLoS ONE*, vol. 12, no. 9, pp. 1–12, 2017.

[60] J. FRATKIN, *Fundamental Neuroscience*, vol. 56 of *ClinicalKey 2012*. Elsevier Science, 1997.

[61] M. Tsodyks, K. Pawelzik, and H. Markram, "Neural Networks with Dynamic Synapses," *Neural Computation*, vol. 10, pp. 821–835, 5 1998.

[62] X. Zhang and J. Feng, "Computational Modeling of Neuronal Networks," *Encyclopedia of Biophysics*, pp. 344–353, 2013.

[63] M. Newman, *Networks*. Oxford university press, 2018.

[64] C. Sutherland, A. K. Fuller, and J. A. Royle, "Modelling non-Euclidean movement and landscape connectivity in highly structured ecological networks," *Methods in Ecology and Evolution*, vol. 6, no. 2, pp. 169–177, 2015.

[65] H. González-Díaz, L. G. Pérez-Montoto, A. Duardo-Sanchez, E. Paniagua, S. Vázquez-Prieto, R. Vilas, M. A. Dea-Ayuela, F. Bolas-Fernández, C. R. Munteanu, J. Dorado, J. Costas, and F. M. Ubeira, "Generalized lattice graphs for 2D-visualization of biological information," *Journal of Theoretical Biology*, vol. 261, no. 1, pp. 136–147, 2009.

[66] K. Himoto, M. Matsumoto, and H. Tanaka, "Lattice- and network-structure in plastic ice," *Phys. Chem. Chem. Phys.*, vol. 13, no. 44, pp. 19876–19881, 2011.

[67] A. Pei, J. Wang, and W. Fang, "Predicting agent-based financial time series model on lattice fractal with random Legendre neural network," *Soft Computing*, vol. 21, no. 7, pp. 1693–1708, 2017.

[68] Z. Li, S. Bianco, Z. Zhang, and C. Tang, "Generic Properties of Random Gene Regulatory Networks," *Quantitative biology (Beijing, China)*, vol. 1, pp. 253–260, 12 2013.

[69] R. Deulofeu, J. Suárez, and A. Pérez-Cervera, "Explaining the behaviour of random ecological networks: the stability of the microbiome as a case of integrative pluralism," *Synthese*, 2019.

[70] M. J. L. Riascos, A P, "Emergence of encounter networks due to human mobility," *PLOS ONE*, vol. 12, no. 10, pp. 1–22, 2017.

[71] S. Milgram, "The small-world problem," *Psychology Today*, vol. 1, no. 61-67, 1967.

[72] E. Ranta, M. S. Fowler, and V. Kaitala, "Population synchrony in small-world networks," *Proceedings of the Royal Society B: Biological Sciences*, vol. 275, no. 1633, pp. 435–442, 2008.

[73] N. R. Taylor, "Small world network strategies for studying protein structures and binding," *Computational and Structural Biotechnology Journal*, vol. 5, p. e201302006, 3 2013.

[74] D. S. Bassett and E. T. Bullmore, "Small-World Brain Networks Revisited," *Neuroscientist*, vol. 23, pp. 499–516, 10 2017.

[75] M. Liu, D. Li, P. Qin, C. Liu, H. Wang, and F. Wang, "Epidemics in interconnected small-world networks," *PLoS ONE*, vol. 10, no. 3, pp. 1–9, 2015.

[76] Y. Gandica, M. Del Castillo-Mussot, G. J. Vzquez, and S. Rojas, "Continuous opinion model in small-world directed networks," *Physica A: Statistical Mechanics and its Applications*, vol. 389, no. 24, pp. 5864–5870, 2010.

[77] C. J. Kim and O. B. Obah, "Vulnerability assessment of power grid using graph topological indices," *International Journal of Emerging Electric Power Systems*, vol. 8, no. 6, 2007.

[78] P. K. Pandey and V. Badarla, "Small-World Regular Networks for Communication," *IEEE Transactions on Circuits and Systems II: Express Briefs*, vol. 67, no. 8, pp. 1409–1413, 2020.

[79] S. Chattopadhyay and C. A. Murthy, "Generation of power-law networks by employing various attachment schemes: Structural properties emulating real world networks," *Information Sciences*, vol. 397-398, pp. 219–242, 2017.

[80] A. D. Broido and A. Clauset, "Scale-free networks are rare," *Nature Communications*, vol. 10, no. 1, p. 1017, 2019.

[81] T. Verma, N. A. Araújo, and H. J. Herrmann, "Revealing the structure of the world airline network," *Scientific Reports*, vol. 4, no. 1, p. 5638, 2014.

[82] R. Albert, "Scale-free networks in cell biology," *Journal of Cell Science*, vol. 118, no. 21, pp. 4947–4957, 2005.

[83] C. León and R. J. Berndsen, "Rethinking financial stability: Challenges arising from financial networks' modular scale-free architecture," *Journal of Financial Stability*, vol. 15, pp. 241–256, 2014.

[84] L. Biggiero and P. P. Angelini, "Hunting scale-free properties in R&D collaboration networks: Self-organization, power-law and policy issues in the European aerospace research area," *Technological Forecasting and Social Change*, vol. 94, pp. 21–43, 2015.

[85] E. Schneidman, M. J. Berry, R. Segev, and W. Bialek, "Weak pairwise correlations imply strongly correlated network states in a neural population," *Nature*, vol. 440, pp. 1007–1012, 4 2006.

[86] S. Cocco, S. Leibler, and R. Monasson, "Neuronal couplings between retinal ganglion cells inferred by efficient inverse statistical physics methods," *Proceedings of the National Academy of Sciences of the United States of America*, vol. 106, no. 33, pp. 14058–14062, 2009.

[87] R. Burioni, M. Casartelli, M. Di Volo, R. Livi, and A. Vezzani, "Average synaptic activity and neural networks topology: A global inverse problem," *Scientific Reports*, vol. 4, pp. 1–7, 2014.

[88] M. Di Volo, R. Burioni, M. Casartelli, R. Livi, and A. Vezzani, "Heterogeneous mean field for neural networks with short-term plasticity," *Physical Review E - Statistical, Nonlinear, and Soft Matter Physics*, vol. 90, p. 22811, 8 2014.

[89] M. Di Volo, R. Burioni, M. Casartelli, R. Livi, and A. Vezzani, "Neural networks with excitatory and inhibitory components: Direct and inverse problems by a mean-field approach," *Physical Review E*, vol. 93, p. 12305, 1 2016.

[90] L. Michiels Van Kessenich, L. De Arcangelis, and H. J. Herrmann, "Synaptic plasticity and neuronal refractory time cause scaling behaviour of neuronal avalanches," *Scientific Reports*, vol. 6, no. May, pp. 1–7, 2016.

[91] R. Russo, H. J. Herrmann, and L. De Arcangelis, "Brain modularity controls the critical behavior of spontaneous activity," *Scientific Reports*, vol. 4, no. March, p. 4312, 2014.

[92] S. G. Shandilya and M. Timme, "Inferring network topology from complex dynamics," *New Journal of Physics*, vol. 13, p. 13004, 1 2011.

[93] I. Malvestio, T. Kreuz, and R. G. Andrzejak, "Robustness and versatility of a nonlinear interdependence method for directional coupling detection from spike trains," *Physical Review E*, vol. 96, p. 22203, 8 2017.

[94] M. Asllani, T. Carletti, F. Di Patti, D. Fanelli, and F. Piazza, "Hopping in the Crowd to Unveil Network Topology," *Physical Review Letters*, vol. 120, p. 158301, 4 2018.

[95] T. M. Liggett, *Stochastic Interacting Systems: Contact, Voter and Exclusion Processes*, vol. 324. Springer-Verlag, Berlin, 1999.

[96] E. Almaas, R. V. Kulkarni, and D. Stroud, "Scaling properties of random walks on small-world networks," *Physical Review E - Statistical Physics, Plasmas, Fluids, and Related Interdisciplinary Topics*, vol. 68, p. 56105, 11 2003.

[97] S. Kwon and Y. Kim, "Effects of excluded volume interaction on diffusion-reaction processes in crowded environments," *Physical Review E - Statistical, Nonlinear, and Soft Matter Physics*, vol. 84, p. 41103, 10 2011.

[98] M. Galanti, D. Fanelli, and F. Piazza, "Macroscopic Transport Equations in Many-Body Systems from Microscopic Exclusion Processes in Disordered Media: A Review," *Frontiers in Physics*, vol. 4, no. August, pp. 12–16, 2016.

[99] A. E. Fernando, K. A. Landman, and M. J. Simpson, "Nonlinear diffusion and exclusion processes with contact interactions," *Physical Review E - Statistical, Nonlinear, and Soft Matter Physics*, vol. 81, p. 11903, 1 2010.

[100] K. A. Landman and A. E. Fernando, "Myopic random walkers and exclusion processes: Single and multispecies," *Physica A: Statistical Mechanics and its Applications*, vol. 390, pp. 3742–3753, 10 2011.

[101] M. Galanti, D. Fanelli, A. Maritan, and F. Piazza, "Diffusion of tagged particles in a crowded medium," *Epl*, vol. 107, p. 20006, 7 2014.

[102] S. N. Dorogovtsev, A. V. Goltsev, and J. F. Mendes, "Critical phenomena in complex networks," *Reviews of Modern Physics*, vol. 80, pp. 1275–1335, 10 2008.

[103] F. Pittorino, M. Ibáñez-Berganza, M. Di Volo, A. Vezzani, and R. Burioni, "Chaos and Correlated Avalanches in Excitatory Neural Networks with Synaptic Plasticity," *Physical Review Letters*, vol. 118, p. 98102, 3 2017.

[104] C. M. Stinear, C. E. Lang, S. Zeiler, and W. D. Byblow, "Advances and challenges in stroke rehabilitation," *Lancet Neurol.*, vol. 19, pp. 348–360, 4 2020.

[105] E. Burke Quinlan, L. Dodakian, J. See, A. McKenzie, V. Le, M. Wojnowicz, B. Shahbaba, and S. C. Cramer, "Neural function, injury, and stroke subtype predict treatment gains after stroke," *Annals of neurology*, vol. 77, no. 1, pp. 132–145, 2015.

[106] S. Prabhakaran, E. Zarahn, C. Riley, A. Speizer, J. Y. Chong, R. M. Lazar, R. S. Marshall, and J. W. Krakauer, "Inter-individual variability in the capacity for motor recovery after ischemic stroke," *Neurorehabilitation and neural repair*, vol. 22, no. 1, pp. 64–71, 2008.

[107] A. R. Carter, K. R. Patel, S. V. Astafiev, A. Z. Snyder, J. Rengachary, M. J. Strube, A. Pope, J. S. Shimony, C. E. Lang, G. L. Shulman, and M. Corbetta, "Upstream dysfunction of somatomotor functional connectivity after corticospinal damage in stroke," *Neurorehabil. Neural Repair*, vol. 26, pp. 7–19, 1 2012.

[108] M. P. A. van Meer, W. M. Otte, K. van der Marel, C. H. Nijboer, A. Kavelaars, J. W. B. van der Sprenkel, M. A. Viergever, and R. M. Dijkhuizen, "Extent of bilateral neuronal network reorganization and functional recovery in relation to stroke severity," *J. Neurosci.*, vol. 32, pp. 4495–4507, 3 2012.

[109] A. L. Allegra Mascaro, E. Conti, S. Lai, A. P. Di Giovanna, C. Spalletti, C. Alia, A. Panarese, A. Scaglione, L. Sacconi, S. Micera, M. Caleo, and F. S. Pavone, "Combined Rehabilitation Promotes the Recovery of Structural and Functional Features of Healthy Neuronal Networks after Stroke," *Cell Reports*, vol. 28, no. 13, pp. 3474–3485, 2019.

[110] C.-C. Chen, S.-H. Lee, W.-J. Wang, Y.-C. Lin, and M.-C. Su, "EEG-based motor network biomarkers for identifying target patients with stroke for upper limb rehabilitation and its construct validity," *PLOS ONE*, vol. 12, no. 6, pp. 1–20, 2017.

[111] J. M. Cassidy, A. Wodeyar, J. Wu, K. Kaur, A. K. Masuda, R. Srinivasan, and S. C. Cramer, "{Low-Frequency} Oscillations Are a Biomarker of Injury and Recovery After Stroke," *Stroke*, p. STROKEAHA120028932, 4 2020.

[112] A. R. Carter, S. V. Astafiev, C. E. Lang, L. T. Connor, J. Rengachary, M. J. Strube, D. L. W. Pope, G. L. Shulman, and M. Corbetta, "Resting interhemispheric functional magnetic resonance imaging connectivity predicts performance after stroke," *Ann. Neurol.*, vol. 67, pp. 365–375, 3 2010.

[113] M. P. A. van Meer, K. van der Marel, K. Wang, W. M. Otte, S. El Bouazati, T. A. P. Roeling, M. A. Viergever, J. W. van der Sprenkel, and R. M. Dijkhuizen, "Recovery of sensorimotor function after experimental stroke correlates with restoration of resting-state interhemispheric functional connectivity," *J. Neurosci.*, vol. 30, pp. 3964–3972, 3 2010.

[114] A. K. Rehme, L. J. Volz, D.-L. Feis, I. Bomilcar-Focke, T. Liebig, S. B. Eickhoff, G. R. Fink, and C. Grefkes, "Identifying Neuroimaging Markers of Motor Disability in Acute Stroke by Machine Learning Techniques," *Cereb. Cortex*, vol. 25, pp. 3046–3056, 9 2015.

[115] T. W. Chen, T. J. Wardill, Y. Sun, S. R. Pulver, S. L. Renninger, A. Baohan, E. R. Schreiter, R. A. Kerr, M. B. Orger, V. Jayaraman, L. L. Looger, K. Svoboda, and D. S. Kim, "Ultrasensitive fluorescent proteins for imaging neuronal activity," *Nature*, vol. 499, no. 7458, pp. 295–300, 2013.

[116] T. C. Harrison, G. Silasi, J. D. Boyd, and T. H. Murphy, "Displacement of sensory maps and disorganization of motor cortex after targeted stroke in mice," *Stroke*, vol. 44, no. 8, pp. 2300–2306, 2013.

[117] M. P. Vanni and T. H. Murphy, "Mesoscale transcranial spontaneous activity mapping in {GCaMP3} transgenic mice reveals extensive reciprocal connections between areas of somatomotor cortex," *J. Neurosci.*, vol. 34, pp. 15931–15946, 11 2014.

[118] M. Carandini, D. Shimaoka, L. F. Rossi, T. K. Sato, A. Benucci, and T. Knöpfel, "Imaging the awake visual cortex with a genetically encoded voltage indicator," *J. Neurosci.*, vol. 35, pp. 53–63, 1 2015.

[119] W. E. Allen, I. V. Kauvar, M. Z. Chen, E. B. Richman, S. J. Yang, K. Chan, V. Gradinaru, B. E. Deverman, L. Luo, and K. Deisseroth, "Global Representations of {Goal-Directed} Behavior in Distinct Cell Types of Mouse Neocortex," *Neuron*, vol. 94, pp. 891–907.e6, 5 2017.

[120] H. Makino, C. Ren, H. Liu, A. N. Kim, N. Kondapaneni, X. Liu, D. Kuzum, and T. Komiyama, "Transformation of Cortex-wide Emergent Properties during Motor Learning," *Neuron*, vol. 94, pp. 880–890.e8, 5 2017.

[121] M. Balbi, M. P. Vanni, M. J. Vega, G. Silasi, Y. Sekino, J. D. Boyd, J. M. LeDue, and T. H. Murphy, "Longitudinal monitoring of mesoscopic cortical activity in a mouse model of microinfarcts reveals dissociations with behavioral and motor function," *J. Cereb. Blood Flow Metab.*, p. 0271678X18763428, 3 2018.

[122] T. Kreuz, E. Satuvuori, M. Pofahl, and M. Mulansky, "Leaders and followers: Quantifying consistency in spatio-temporal propagation patterns," *New Journal of Physics*, vol. 19, p. 43028, 2017.

[123] C. Spalletti, C. Alia, S. Lai, A. Panarese, S. Conti, S. Micera, and M. Caleo, "Combining robotic training and inactivation of the healthy hemisphere restores pre-stroke motor patterns in mice," *eLife*, vol. 6, 2017.

[124] C. Spalletti, S. Lai, M. Mainardi, A. Panarese, A. Ghionzoli, C. Alia, L. Gianfranceschi, C. Chisari, S. Micera, and M. Caleo, "A robotic system for quantitative assessment and poststroke training of forelimb retraction in mice," *Neurorehabilitation and Neural Repair*, vol. 28, pp. 188–196, 2 2014.

[125] M. Pasquini, S. Lai, C. Spalletti, M. Cracchiolo, S. Conti, A. Panarese, M. Caleo, and S. Micera, "A robotic system for adaptive training and function assessment of forelimb retraction in mice," *IEEE Transactions on Neural Systems and Rehabilitation Engineering*, vol. 26, no. 9, pp. 1803–1812, 2018.

[126] E. S. Lein, M. J. Hawrylycz, N. Ao, M. Ayres, A. Bensinger, A. Bernard, A. F. Boe, M. S. Boguski, K. S. Brockway, E. J. Byrnes, L. Chen, L. Chen, T.-M. Chen, M. C. Chin, J. Chong, B. E. Crook, A. Czaplinska, C. N. Dang, S. Datta, N. R. Dee, A. L. Desaki, T. Desta, E. Diep, T. A. Dolbeare, M. J. Donelan, H.-W. Dong, J. G. Dougherty, B. J. Duncan, A. J. Ebbert, G. Eichele, L. K. Estin, C. Faber, B. A. Facer, R. Fields, S. R. Fischer, T. P. Fliss, C. Frensley, S. N. Gates, K. J. Glattfelder, K. R. Halverson,

M. R. Hart, J. G. Hohmann, M. P. Howell, D. P. Jeung, R. A. Johnson, P. T. Karr, R. Kawal, J. M. Kidney, R. H. Knapik, C. L. Kuan, J. H. Lake, A. R. Laramee, K. D. Larsen, C. Lau, T. A. Lemon, A. J. Liang, Y. Liu, L. T. Luong, J. Michaels, J. J. Morgan, R. J. Morgan, M. T. Mortrud, N. F. Mosqueda, L. L. Ng, R. Ng, G. J. Orta, C. C. Overly, T. H. Pak, S. E. Parry, S. D. Pathak, O. C. Pearson, R. B. Puchalski, Z. L. Riley, H. R. Rockett, S. A. Rowland, J. J. Royall, M. J. Ruiz, N. R. Sarno, K. Schaffnit, N. V. Shapovalova, T. Sivisay, C. R. Slaughterbeck, S. C. Smith, K. A. Smith, B. I. Smith, A. J. Sodt, N. N. Stewart, K.-R. Stumpf, S. M. Sunkin, M. Sutram, A. Tam, C. D. Teemer, C. Thaller, C. L. Thompson, L. R. Varnam, A. Visel, R. M. Whitlock, P. E. Wohnoutka, C. K. Wolkey, V. Y. Wong, M. Wood, M. B. Yaylaoglu, R. C. Young, B. L. Youngstrom, X. F. Yuan, B. Zhang, T. A. Zwingman, and A. R. Jones, "Genome-wide atlas of gene expression in the adult mouse brain," *Nature*, vol. 445, pp. 168–176, 1 2007.

[127] R. Quian Quiroga, T. Kreuz, and P. Grassberger, "Event Synchronization: simple and fast method to measure synchronicity and time delay patterns," *Phys. Rev. E*, vol. 66, p. 41904, 2002.

[128] T. Kreuz, M. Mulansky, and N. Bozanic, "SPIKY: A graphical user interface for monitoring spike train synchrony," *Journal of Neurophysiology*, vol. 113, no. 9, pp. 3432–3445, 2015.

[129] H. Yanai, K. Takeuchi, and Y. Takane, *Projection Matrices, Generalized Inverse Matrices, and Singular Value Decomposition*. Springer, 2011.

[130] F. Gerhard, G. Pipa, B. Lima, S. Neuenschwander, and W. Gerstner, "Extraction of network topology from multi-electrode recordings: Is there a small-world effect?," *Frontiers in Computational Neuroscience*, vol. 5, no. February, pp. 1–13, 2011.

[131] K. J. Friston, "Functional and Effective Connectivity: A Review," *Brain Connectivity*, vol. 1, no. 1, pp. 13–36, 2011.

[132] Y. V. Zaytsev, A. Morrison, and M. Deger, "Reconstruction of recurrent synaptic connectivity of thousands of neurons from simulated spiking activity," *Journal of Computational Neuroscience*, vol. 39, no. 1, pp. 77–103, 2015.

[133] O. Stetter, D. Battaglia, J. Soriano, and T. Geisel, "Model-Free Reconstruction of Excitatory Neuronal Connectivity from Calcium Imaging Signals," *PLoS Computational Biology*, vol. 8, no. 8, 2012.

[134] V. Pernice and S. Rotter, "Reconstruction of sparse connectivity in neural networks from spike train covariances," *Journal of Statistical Mechanics: Theory and Experiment*, vol. 2013, p. P03008, 3 2013.

[135] G. Deco, A. Ponce-Alvarez, D. Mantini, G. L. Romani, P. Hagmann, and M. Corbetta, "Resting-state functional connectivity emerges from structurally and dynamically shaped slow linear fluctuations," *Journal of Neuroscience*, vol. 33, no. 27, pp. 11239–11252, 2013.

[136] S. J. Tripathy, K. Padmanabhan, R. C. Gerkin, and N. N. Urban, "Intermediate intrinsic diversity enhances neural population coding," *Proceedings of the National Academy of Sciences of the United States of America*, vol. 110, no. 20, pp. 8248–8253, 2013.

[137] N. Dehghani, A. Peyrache, B. Telenczuk, M. Le Van Quyen, E. Halgren, S. S. Cash, N. G. Hatsopoulos, and A. Destexhe, "Dynamic balance of excitation and inhibition in human and monkey neocortex," *Scientific Reports*, vol. 6, pp. 1–12, 2016.

[138] A. Marty, *Neuromodulation: The Biochemical Control of Neuronal Excitability*, vol. 11. Oxford University Press, 1988.

[139] O. Harish and D. Hansel, "Asynchronous Rate Chaos in Spiking Neuronal Circuits," *PLoS Computational Biology*, vol. 11, no. 7, pp. 1–38, 2015.

[140] C. Van Vreeswijk and H. Sompolinsky, "Chaos in neuronal networks with balanced excitatory and inhibitory activity," *Science*, vol. 274, pp. 1724–1726, 12 1996.

[141] R. W. Olsen and M. Avoli, "Progress in epilepsy research: GABA and epileptogenesis," *Epilepsia*, vol. 38, pp. 399–407, 4 1997.

[142] X. Fan, N. Gaspard, B. Legros, F. Lucchetti, R. Ercek, and A. Nonclercq, "Automated epileptic seizure detection based on break of excitation/inhibition balance," *Computers in Biology and Medicine*, vol. 107, pp. 30–38, 2019.

[143] G. Deco, A. Ponce-Alvarez, P. Hagmann, G. L. Romani, D. Mantini, and M. Corbetta, "How local excitation-inhibition ratio impacts the whole brain dynamics," *Journal of Neuroscience*, vol. 34, no. 23, pp. 7886–7898, 2014.

[144] R. Pastor-Satorras and A. Vespignani, "Epidemic spreading in scale-free networks," *Physical Review Letters*, vol. 86, pp. 3200–3203, 4 2001.

[145] A. Vespignani, "Modelling dynamical processes in complex socio-technical systems," *Nature Physics*, vol. 8, no. 1, pp. 32–39, 2012.

[146] I. Adam, D. Fanelli, T. Carletti, and G. Innocenti, *Reactive explorers to unravel network topology*, vol. 92. 11 2019.

[147] K. Schiene, C. Bruehl, K. Zilles, M. Qü, G. Hagemann, M. Kraemer, and O. W. Witte, "Neuronal hyperexcitability and reduction of GABA(A)-receptor expression in the surround of cerebral photothrombosis," *Journal of Cerebral Blood Flow and Metabolism*, vol. 16, no. 5, pp. 906–914, 1996.

[148] T. Neumann-Haefelin, G. Hagemann, and O. W. Witte, "Cellular correlates of neuronal hyperexcitability in the vicinity of photochemically induced cortical infarcts in rats in vitro," *Neuroscience Letters*, vol. 193, no. 2, pp. 101–104, 1995.

[149] D. Berger, E. Varriale, L. M. van Kessenich, H. J. Herrmann, and L. de Arcangelis, "Three cooperative mechanisms required for recovery after brain damage," *Scientific Reports*, vol. 9, p. 15858, 11 2019.

[150] M. V. Tsodyks and H. Markram, "The neural code between neocortical pyramidal neurons depends on neurotransmitter release probability," *Proceedings of the National Academy of Sciences of the United States of America*, vol. 94, no. 2, pp. 719–723, 1997.

[151] M. Tsodyks, A. Uziel, and H. Markram, "Synchrony generation in recurrent networks with frequency-dependent synapses.," *The Journal of neuroscience : the official journal of the Society for Neuroscience*, vol. 20, p. RC50, 1 2000.

[152] M. Di Volo, R. Livi, S. Luccioli, A. Politi, and A. Torcini, "Synchronous dynamics in the presence of short-term plasticity," *Physical Review E - Statistical, Nonlinear, and Soft Matter Physics*, vol. 87, p. 32801, 3 2013.

[153] S. Wolf, W. Supatto, G. Debrégeas, P. Mahou, S. G. Kruglik, J.-M. Sintes, E. Beaurepaire, and R. Candelier, "Whole-brain functional imaging with two-photon light-sheet microscopy," *Nature Methods*, vol. 12, no. 5, pp. 379–380, 2015.

[154] G. de Vito, C. Fornetto, P. Ricci, C. Müllenbroich, G. Sancataldo, L. Turrini, G. Mazzamuto, N. Tiso, L. Sacconi, D. Fanelli, L. Silvestri, F. Vanzi, and F. S. Pavone, "Two-photon high-speed light-sheet volumetric imaging of brain activity during sleep in zebrafish larvae," in *Neural Imaging and Sensing 2020*, vol. 11226, p. 3, International Society for Optics and Photonics, 2020.

[155] G. de Vito, L. Turrini, C. Fornetto, P. Ricci, C. Müllenbroich, G. Sancataldo, E. Trabalzini, G. Mazzamuto, N. Tiso, L. Sacconi, D. Fanelli, L. Silvestri, F. Vanzi, and F. S. Pavone, "Two-photon light-sheet microscopy for high-speed whole-brain functional imaging of zebrafish neuronal physiology and pathology," in *Neurophotonics*, vol. 11360, p. 3, International Society for Optics and Photonics, 2020.

[156] O. Randlett, C. L. Wee, E. A. Naumann, O. Nnaemeka, D. Schoppik, J. E. Fitzgerald, R. Portugues, A. M. Lacoste, C. Riegler, F. Engert, and A. F. Schier, "Whole-brain activity mapping onto a zebrafish brain atlas," *Nature Methods*, vol. 12, no. 11, pp. 1039–1046, 2015.

[157] M. Kunst, E. Laurell, N. Mokayes, A. Kramer, F. Kubo, A. M. Fernandes, D. Förster, M. Dal Maschio, and H. Baier, "A Cellular-Resolution Atlas of the Larval Zebrafish Brain," *Neuron*, vol. 103, no. 1, pp. 21–38, 2019.

[158] M. Tsodyks, K. Pawelzik, and H. Markram, "Neural Networks with Dynamic Synapses," *Neural Computation*, vol. 10, pp. 821–835, 5 1998.

[159] I. Adam, G. Cecchini, D. Fanelli, T. Kreuz, R. Livi, M. d. Volo, A. L. Allegra Mascaro, E. Conti, A. Scaglione, L. Silvestri, and F. S. Pavone, "Inferring network structure and local dynamics from neuronal patterns with quenched disorder," *Chaos, Solitons and Fractals*, vol. 140, 2020.

[160] P. F. Baker, A. L. Hodgkin, and E. B. Ridgway, "Depolarization and calcium entry in squid giant axons," *The Journal of Physiology*, vol. 218, no. 3, pp. 709–755, 1971.

[161] C. Grienberger and A. Konnerth, "Imaging Calcium in Neurons," *Neuron*, vol. 73, no. 5, pp. 862–885, 2012.

[162] E. A. Naumann, A. R. Kampff, D. A. Prober, A. F. Schier, and F. Engert, "Monitoring neural activity with bioluminescence during natural behavior," *Nature Neuroscience*, vol. 13, no. 4, pp. 513–520, 2010.

[163] V. Volman, I. Baruchi, E. Persi, and E. Ben-Jacob, "Generative modelling of regulated dynamical behavior in cultured neuronal networks," *Physica A: Statistical Mechanics and its Applications*, vol. 335, no. 1-2, pp. 249–278, 2004.

[164] R. G. Northcutt, "Forebrain evolution in bony fishes," *Brain Research Bulletin*, vol. 75, no. 2-4, pp. 191–205, 2008.

[165] T. Mueller, "What is the thalamus in zebrafish?," *Frontiers in Neuroscience*, vol. 6, no. MAY, p. 64, 2012.

[166] T. Yokogawa, M. C. Hannan, and H. A. Burgess, "The dorsal raphe modulates sensory responsiveness during arousal in zebrafish," *Journal of Neuroscience*, vol. 32, no. 43, pp. 15205–15215, 2012.

[167] L. Garcia-Campmany, F. J. Stam, and M. Goulding, "From circuits to behaviour: motor networks in vertebrates," *Current Opinion in Neurobiology*, vol. 20, no. 1, pp. 116–125, 2010.

[168] A. Kinkhabwalaa, M. Riley, M. Koyama, J. Monen, C. Satou, Y. Kimura, S. I. Higashijima, and J. Fetcho, "A structural and functional ground plan for neurons in the hindbrain of zebrafish," *Proceedings of the National Academy of Sciences of the United States of America*, vol. 108, no. 3, pp. 1164–1169, 2011.

[169] L. Heap, C. C. Goh, K. S. Kassahn, and E. K. Scott, "Cerebellar output in zebrafish: An analysis of spatial patterns and topography in eurydendroid cell projections," *Frontiers in Neural Circuits*, vol. 7, no. MAR, p. 53, 2013.

[170] J. Kaslin and M. Brand, "The zebrafish cerebellum," in *Essentials of Cerebellum and Cerebellar Disorders: A Primer for Graduate Students*, pp. 411–421, Springer, 2016.

[171] P. Sajovic and C. Levinthal, "Visual cells of zebrafish optic tectum: Mapping with small spots," *Neuroscience*, vol. 7, no. 10, pp. 2407–2426, 1982.

[172] C. Gebhardt, T. O. Auer, P. M. Henriques, G. Rajan, K. Duroure, I. H. Bianco, and F. Del Bene, "An interhemispheric neural circuit allowing binocular integration in the optic tectum," *Nature Communications*, vol. 10, no. 1, pp. 1–12, 2019.

[173] G. de Vito, P. Ricci, L. Turrini, V. Gavryusev, C. Müllenbroich, N. Tiso, F. Vanzi, L. Silvestri, and F. S. Pavone, "Effects of excitation light polarization on fluorescence emission in two-photon light-sheet microscopy," *Biomedical Optics Express*, vol. 11, no. 8, p. 4651, 2020.

[174] N. Vladimirov, Y. Mu, T. Kawashima, D. V. Bennett, C. T. Yang, L. L. Looger, P. J. Keller, J. Freeman, and M. B. Ahrens, "Light-sheet functional imaging in fictively behaving zebrafish," *Nature Methods*, vol. 11, no. 9, pp. 883–884, 2014.

[175] M. C. Müllenbroich, L. Turrini, L. Silvestri, T. Alterini, A. Gheisari, N. Tiso, F. Vanzi, L. Sacconi, and F. S. Pavone, "Corrigendum: Bessel beam illumination reduces random and systematic errors in quantitative functional studies using light-sheet microscopy (frontiers in cellular neuroscience, (2018),

12, 10.3389/fncel.2018.00315)," *Frontiers in Cellular Neuroscience*, vol. 13, pp. 1–1, 2019.

[176] L. Turrini, C. Fornetto, G. Marchetto, M. C. Müllenbroich, N. Tiso, A. Vettori, F. Resta, A. Masi, G. Mannaioni, F. S. Pavone, and F. Vanzi, "Optical mapping of neuronal activity during seizures in zebrafish," *Scientific Reports*, vol. 7, no. 1, pp. 1–12, 2017.

[177] M. Westerfield, "The Zebrafish Book. A Guide for the Laboratory Use of Zebrafish (Danio rerio), 5th Edition," *University of Oregon Press, Eugene (Book)*, 2007.

[178] D. Hutchinson, M. Preston, and T. Hewitt, "Adaptive Refinement for Mass/Spring Simulations," pp. 31–45, 1996.

[179] P. Howlett and W. Hewitt, "Mass-Spring Simulation using Adaptive Non-Active Points," *Computer Graphics Forum*, vol. 17, no. 3, pp. 345–353, 1998.

[180] S. Bayraktar, U. Gudukbay, and B. Ozguc, "Practical and Realistic Animation of Cloth," in *2007 3DTV Conference*, pp. 1–4, 2007.

[181] A. Duysak, J. J. Zhang, and V. Ilankovan, "Efficient modelling and simulation of soft tissue deformation using mass-spring systems," *International Congress Series*, vol. 1256, no. C, pp. 337–342, 2003.

[182] D. Zerbato, S. Galvan, and P. Fiorini, "Calibration of mass spring models for organ simulations," in *2007 IEEE/RSJ International Conference on Intelligent Robots and Systems*, pp. 370–375, 2007.

[183] M. Chen and F. J. Boyle, "Investigation of membrane mechanics using spring networks: Application to red-blood-cell modelling," *Materials Science and Engineering C*, vol. 43, pp. 506–516, 2014.

[184] M. K. Rausch and E. Kuhl, "On the effect of prestrain and residual stress in thin biological membranes," *Journal of the Mechanics and Physics of Solids*, vol. 61, no. 9, pp. 1955–1969, 2013.

[185] F. Delhomme, M. Mommessin, J. P. Mougin, and P. Perrotin, "Simulation of a block impacting a reinforced concrete slab with a finite element model and a mass-spring system," *Engineering Structures*, vol. 29, no. 11, pp. 2844–2852, 2007.

[186] A. R. Atilgan, S. R. Durell, R. L. Jernigan, M. C. Demirel, O. Keskin, and I. Bahar, "Anisotropy of fluctuation dynamics of proteins with an elastic network model," *Biophysical Journal*, vol. 80, no. 1, pp. 505–515, 2001.

[187] L. Yang, G. Song, and R. L. Jernigan, "Protein elastic network models and the ranges of cooperativity," *Proceedings of the National Academy of Sciences of the United States of America*, vol. 106, no. 30, pp. 12347–12352, 2009.

[188] J. Echave, "Evolutionary divergence of protein structure: The linearly forced elastic network model," *Chemical Physics Letters*, vol. 457, no. 4-6, pp. 413–416, 2008.

[189] H. Dietz and M. Rief, "Elastic Bond Network Model for Protein Unfolding Mechanics," *Phys. Rev. Lett.*, vol. 100, p. 98101, 3 2008.

[190] Y. Togashi and A. S. Mikhailov, "Nonlinear relaxation dynamics in elastic networks and design principles of molecular machines," *Proceedings of the National Academy of Sciences of the United States of America*, vol. 104, no. 21, pp. 8697–8702, 2007.

[191] S. A. Wieninger, E. H. Serpersu, and G. M. Ullmann, "ATP binding enables broad antibiotic selectivity of aminoglycoside phosphotransferase(3â^2) – $IIIa$: $An elastic network kanalysis,'' Journal of Molecular Biology, vol.$ 409, $no.$ 3, $pp.$ 450− −465, 2011.

[192] W. Zheng and S. Doniach, "A comparative study of motor-protein motions by using a simple elastic-network model," *Proceedings of the National Academy of Sciences of the United States of America*, vol. 100, no. 23, pp. 13253–13258, 2003.

[193] H. Flechsig and Y. Togashi, "Designed elastic networks: Models of complex protein machinery," *International Journal of Molecular Sciences*, vol. 19, no. 10, 2018.

[194] J. CORTÉS and M. EGERSTEDT, "Coordinated Control of Multi-Robot Systems: A Survey," *SICE Journal of Control, Measurement, and System Integration*, vol. 10, no. 6, pp. 495–503, 2017.

[195] P. Brochu, H. Stoyanov, X. Niu, and Q. Pei, "All-silicone prestrain-locked interpenetrating polymer network elastomers: Free-standing silicone artificial muscles with improved performance and robustness," *Smart Materials and Structures*, vol. 22, no. 5, 2013.

[196] S. M. Ha, W. Yuan, Q. Pei, R. Pelrine, and S. Stanford, "Interpenetrating networks of elastomers exhibiting 300% electrically-induced area strain," *Smart Materials and Structures*, vol. 16, no. 2, 2007.

[197] A. Kim, J. Ahn, H. Hwang, E. Lee, and J. Moon, "A pre-strain strategy for developing a highly stretchable and foldable one-dimensional conductive cord based on a Ag nanowire network," *Nanoscale*, vol. 9, no. 18, pp. 5773–5778, 2017.

[198] S. M. Ha, W. Yuan, Q. Pei, R. Pelrine, and S. Stanford, "Interpenetrating polymer networks for high-performance electroelastomer artificial muscles," *Advanced Materials*, vol. 18, no. 7, pp. 887–891, 2006.

[199] G. Caldarelli, *Scale-Free Networks - Complex Webs in Nature and Technology*. 2007.

[200] G. Caldarelli, A. Capocci, P. De Los Rios, and M. A. Muñoz, "Scale-Free Networks from Varying Vertex Intrinsic Fitness," *Phys. Rev. Lett.*, vol. 89, p. 258702, 12 2002.

[201] C. Crocini, C. Ferrantini, R. Coppini, M. Scardigli, P. Yan, L. M. Loew, G. Smith, E. Cerbai, C. Poggesi, F. S. Pavone, and others, "Optogenetics design of mechanistically-based stimulation patterns for cardiac defibrillation," *Scientific reports*, vol. 6, p. 35628, 2016.

[202] E. Conti, A. Mascaro, A. Letizia, and F. S. Pavone, "Large Scale Double-Path Illumination System with Split Field of View for the All-Optical Study of Inter-and Intra-Hemispheric Functional Connectivity on Mice," *Methods and protocols*, vol. 2, no. 1, p. 11, 2019.

[203] D. Bates, M. Mächler, B. Bolker, and S. Walker, "Fitting Linear Mixed-Effects Models Using {lme4}," *Journal of Statistical Software*, vol. 67, no. 1, pp. 1–48, 2015.

[204] H. Matuschek, R. Kliegl, S. Vasishth, H. Baayen, and D. Bates, "Balancing Type I error and power in linear mixed models," *Journal of Memory and Language*, vol. 94, pp. 305–315, 2017.

[205] A. Kuznetsova, P. B. Brockhoff, and R. H. B. Christensen, "{lmerTest} Package: Tests in Linear Mixed Effects Models," *Journal of Statistical Software*, vol. 82, no. 13, pp. 1–26, 2017.

[206] M. J. Gurka, L. J. Edwards, K. E. Muller, and L. L. Kupper, "Extending the Box–Cox transformation to the linear mixed model," *Journal of the Royal Statistical Society: Series A (Statistics in Society)*, vol. 169, no. 2, pp. 273–288, 2006.

[207] C. Agostinelli and U. Lund, "{R} package \texttt{circular}: Circular Statistics (version 0.4-93)," 2017.

[208] S. R. Jammalamadaka and A. Sengupta, *Topics in circular statistics*, vol. 5. world scientific, 2001.

[209] E. Satuvuori, M. Mulansky, N. Bozanic, I. Malvestio, F. Zeldenrust, K. Lenk, and T. Kreuz, "Measures of spike train synchrony for data with multiple time scales," *J Neurosci Methods*, vol. 287, pp. 25–38, 2017.

[210] M. Mulansky and T. Kreuz, "PySpike {-} \textsc{A} Python library for analyzing spike train synchrony," *Software X*, vol. 5, p. 183, 2016.

Acknowledgments

The time I have spent studying complex systems has given me a fresh perspective and wider appreciation for how things and events, in particular, relate to one another. This thesis and my work would not exist in the form it does if it were not for the nurturing support, help and guidance of many individuals. To put it differently, I would like to sincerely thank and honour everyone whose help in countless ways has produced this thesis (even if I have failed to personally mention them here).

Prof. Duccio Fanelli, my PhD supervisor, whose work ethic and dedication has always motivated me. My work has been steered through his brilliant knowledge and insight into a vast array of topics. I want to also thank my supervisor Prof. Giacomo Innocenti, for his support and all the help in getting me to where I am.

A sincere thanks to Dr. Paolo Paoletti, for inspiring my love for research way before the start of my PhD. Thank you so much for welcoming me and hosting my research visit to the University of Liverpool and for the measureless support and guidance.

I want to thank all the members of CSDC and colleagues that I had the good fortune of sharing the office with me. Thank you for welcoming and accepting me as one of your own and making the effort to converse with me in English whenever I was around. Lorenzo, Leo, Francesca and Sara, you have been the most wonderful office mates and I will cherish these years for a lifetime. Thank you, Gloria, Lorenzo, Prof.Franco Bagnoli, Giovanna and Vale for all the great lunches we have and much-needed coffee breaks we have shared. A special thanks to Sara for helping me navigate the bureaucratic nuances, Gloria for her guidance and support and Prof. Bagnoli for his important input and insights that helped during the journey.

Last but most definitely not the least, my family who has supported me through thick and thin. My wife, for lovingly accepting me at my lowest and holding my hand through the ups and downs of the delightful walk that is the PhD. My mom and dad for always being there, and whose well wishes and love has made it possible for me to go out chase my dreams.

Thank you for making this work possible.